TOWARDS AIRBORNE MEASUREMENTS OF GROUND DISPLACEMENT

by

Thomas D. Rapstine

© Copyright by Thomas D. Rapstine, 2020

All Rights Reserved

A thesis submitted to the Faculty and the Board of Trustees of the Colorado School of Mines in partial fulfillment of the requirements for the degree of PhD (Geophysics).

Golden, Colorado

Date _____

Signed: _____
Thomas D. Rapstine

Signed: _____
Dr. Paul Sava Advisor
Thesis Advisor

Golden, Colorado

Date _____

Signed: _____
Dr. Paul Sava
Professor and Head
Department of Geophysics

ABSTRACT

Valuable resources and risk assessments are realized by mapping variations of the physical composition and structure at the surface and in the subsurface of the Earth. A key measurement for realizing these benefits is measuring ground displacement as a function of time, which enable geophysicists to conduct seismic studies for inferring subsurface structure and composition, and enable geomorphologists to study and monitor landslides. It is difficult to measure ground displacement due to seismic waves or landslide failure since such phenomena evolve rapidly and exhibit large dynamic ranges. In addition, logistic, environmental, and safety concerns limit when and where seismic or landslide measurements can occur. These issues motivate the need for rapid, accurate, remote, and possibly airborne measurements of displacement time series. Simultaneously addressing all of these issues is challenging since conventional sensors capable of accurately measuring ground displacement, such as a geophones, require physical coupling to the ground and only measure displacement at one location. However, advancements in the field of computer vision, together with rapid development of drone and camera hardware, provide a foundation for rapid and accurate airborne displacement measurements, thus aiding geophysicists and geomorphologists in their respective studies. In this thesis, I describe multiple theoretical advances that enable remote video-based measurements of subtle rapidly varying ground displacement for applications in geophysics and geomorphology. Based on the methods and applications discovered in this thesis, I draw four main conclusions. (1) Earthquake signals can theoretically be measured using drone-borne stereo cameras, provided that the camera position is known with sufficient accuracy. (2) Video cameras can be used to remotely and accurately measure ground surface displacement and velocity during a rapidly evolving landslide. (3) When static markers are present, the position and velocity of a debris-flow front can be measured with accuracy comparable to that of lidar, but with much denser spatial distribution. (4) Using

measurements acquired from an airborne platform, ground displacement can be recovered accurately under reasonable assumptions about the platform motion. These conclusions demonstrate that airborne video measurements are on the brink of becoming a viable solution for obtaining ground displacement. Airborne measurements are faster and safer than the state of art, cover a wider area, and dramatically reduce environmental impact of seismic acquisition surveys while maintaining the accuracy needed for a multitude of geophysical applications.

TABLE OF CONTENTS

ABSTRACT iii

LIST OF FIGURES AND TABLES viii

LIST OF ABBREVIATIONS xv

ACKNOWLEDGMENTS xvi

DEDICATION xviii

CHAPTER 1 INTRODUCTION 1

CHAPTER 2 AIRBORNE SEISMIC DATA ACQUISITION USING STEREO VISION 4

2.1 Abstract 4

2.2 Introduction 4

2.3 Theory 6

2.4 Numerical examples 12

2.5 Conclusions 17

2.6 Acknowledgments 18

CHAPTER 3 RECONSTRUCTING THE EVOLUTION OF A RAPID LANDSLIDE USING MULTIVIEW VIDEO 19

3.1 Abstract 19

3.2 Introduction 20

3.3 Methods 23

3.3.1 Experimental setup 23

3.3.2 Reconstructing a dynamic 3-D surface from images 26

3.3.3 Reconstructing a transect of the deforming ground surface using lidar . 34

3.3.4 Computing dilation rate from surface displacements and velocities . . . 34

3.4 Results . . . 37

3.5 Discussion . . . 43

3.5.1 Error Analysis . . . 43

3.5.2 Mechanical Interpretation of Deformation during Slope Failure . . . 47

3.5.3 Future Directions . . . 49

3.6 Conclusion . . . 50

3.7 Acknowledgments . . . 51

CHAPTER 4 A TECHNIQUE FOR MEASURING THE VELOCITY FIELD OF A DEBRIS FLOW USING A SINGLE VIDEO . . . 52

4.1 Abstract . . . 52

4.2 Introduction . . . 53

4.3 Methods . . . 54

4.3.1 Experimental Setup . . . 54

4.3.2 Constructing a flow gather . . . 55

4.3.3 Quantifying surface velocity using a flow gather . . . 57

4.4 Results and Discussion . . . 58

4.4.1 Flow gathers on May 23rd and May 25th, 2017 experiments . . . 58

4.4.2 Debris-flow flow front position and velocity . . . 61

4.4.3 Debris-flow surface velocity . . . 68

4.5 Conclusion . . . 69

4.6 Acknowledgements . . . 69

CHAPTER 5 SEPARATING SENSOR MOTION FROM SEISMIC MOTION 73
5.1 Introduction 74
5.2 Methods 76
5.2.1 Airborne sensor motion model 76
5.2.2 Defining a seismic signal model 78
5.2.3 Topography as a randomly generated smooth surface 79
5.2.4 Simulating a moving surface as viewed from a noisy airborne sensor . . 81
5.2.5 Separating platform motion from seismic signals 82
5.3 Results and Discussion 85
5.3.1 Seismic signal separation in noiseless observations 86
5.3.2 Seismic signal separation in noisy observations 86
5.3.3 Separation dependency on sensor rotation 88
5.3.4 Separation dependency on sensor noise level and max peak signal . . . 90
5.3.5 Separation dependency on sample spacing 91
5.4 Conclusion 95
5.5 Acknowledgements 95
CHAPTER 6 CONCLUSION 96
REFERENCES CITED 99
APPENDIX 108
A.1 Estimating a rigid body transformation between point clouds 108
A.2 Permissions from journal 109
A.3 Permissions from coauthors 109

LIST OF FIGURES AND TABLES

Figure 2.1 A schematic of stereo cameras viewing the ground from above. The dashed paths show where a point on the ground projects on the left and right cameras, each with focal length f. The cameras optical axis are aligned and separated by b. 7

Figure 2.2 Left, right, and disparity image examples for the earthquake simulation (shown left to right, respectively). Note the left and right images are shifted versions of one another. The shift is quantified in the disparity image on the far right; smaller (darker) disparity values are farther away from the camera and indicate cracks in the ground. 13

Figure 2.3 Earthquake (top three plots) and UAV motion (bottom three plots) used in hovering UAV simulation. The red, blue, and green curves show x, y, and z positions. Earthquake data is recorded ground motions for the 2016 (M5.0) earthquake near Cushing, Oklahoma at USGS station OK034. We note that the UAV motion is three orders of magnitude larger than the earthquake signal we wish to recover. 14

Figure 2.4 Recovered ground position PDF (top) without and (bottom) with UAV motion. White curve shows the mean value of ground position, which resemble the vertical ground motion from the simulated earthquake. . . . 15

Figure 2.5 Recovered ground displacement signal compared with true displacement (top) without and (bottom) with UAV motion. Red curves show the absolute difference between recovered and true ground motion. Drone motion influences the recovery of the input signal. 16

Figure 3.1 Schematic of the sediment prism and sensor layout during the experiment. 25

Figure 3.2 Views of the sediment prism from one video camera near failure time ($t_f = 0$). Failure occurs rapidly over a few seconds which calls for rapid measurements of surface deformation. 26

Figure 3.3 (a) Appearance-based and (b) audio-based timing alignment results. The timing of events in (red) video 1 were aligned to match (blue) video 2 to obtain (black) shifted versions of signals in video 1. The horizontal-axis denotes video time corresponding to each signal as labelled in the legend. In (a) the vertical-axis denotes normalized color intensity whereas in (b) the vertical-axis denotes the normalized audio signal. Appearance-based and audio-based signal alignment results agree with each other, and are imperative for successfully applying 4D reconstruction using video images. 28

Figure 3.4 A subset of georeferenced vertical displacement maps of the sediment prism surface from its original state over an approximate 10 second interval of the video. Blue colors show downward displacement, white indicates zero displacement, and brown indicates upward displacement. During failure, height change varies over several orders of magnitude, so each panel has a different colorbar; each colorbar is shown in the rightmost column as a function of column index within the plot. The area of upward motion gradually propagated downslope as failure progressed. The effects of uncalibrated lens parameters are apparent in the upper left panel at 0.03 seconds as slanted stripes. The hatched areas in the bottom row denote areas where block-like processing artefacts occur due to image blur. 32

Figure 3.5 Video-based observations of (a) Δz, (b) v_z, and (c) v_x variations near the upslope, midslope, and downslope pore pressure sensors. During failure ($t_f = 0$), the upslope and midslope portion of the sediment prism moved downwards and the downslope portion moved up as sediment flowed downslope. 33

Figure 3.6 Deforming ground surface observations during natural-release failure measured along the lidar transect. The point color brightness increases with time in t_f (yellow points occur at greater times t_f). (a) Lidar and (b) video-based results show similar results. (c) Lidar and video-based results at a subset of times t_f. Lidar and video-based results are more similar before failure than after. The absence of dense lidar points in the upper portions of the sediment prism ($x > 1.5$) is caused by moving sediment blocking the lidar laser. 39

Figure 3.7 Observations of surface elevation z along the lidar transect derived from (a) lidar and (b) video as a function of time and space. The (c) difference between lidar and video is small. 40

Figure 3.8 Empirical probability density function (PDF) of the difference ϵ_z between lidar and video results along the lidar transect (a) before, and (b) after failure at $t_f = 0$. Note that horizontal and vertical axis in (a) and (b) are at different scales. The difference is characteristically smaller before failure than after. After failure, image blur and the sediment blocking the lidar laser cause larger differences between results. . 41

Figure 3.9 Pore pressure and velocity variation near failure for the (a) upslope, (b) midslope, and (c) downslope sensor locations. Two pore pressure sensors were placed at each location upslope, midslope, and downslope; the depths d of each sensor are noted in the legend. Pore pressure suddenly decreased in the upslope portion of the sediment prism before failure initiated. After failure, sediment rapidly moves downslope indicated by the velocity curves. 42

Figure 3.10 Soil dilation rate computed using (a) equation 3.1 and $k_{min} = 1 \times 10^{-11}$ m^2, (b) using equation 3.10, and (c) using equation 3.1 and $k_{max} = 1 \times 10^{-7}$ m^2. Results from equation 3.1 (a & c) should only be trusted for $t_f < 2$ s since the pore pressure sensors were being pulled by cables beyond this time. These curves confirm our hypothesis that (b) video-based estimates of dilation rate are within reasonable ranges of (a & c) estimates that depend on in situ measurements of pore pressure. . 43

Figure 3.11 Soil dilation rate along the x-axis of the sediment prism as computed using video observations and equation 3.10. Red colors indicate positions and times which exhibit dilation and blue colors indicate contraction. The location of pore pressure sensors are noted by the dashed lines. When the sediment fails ($t_f = 0$) a narrow band of contraction initiates upslope then propagates downslope. The sediment dilated and contracted during and after failure; the sediment did not strictly behave as an incompressible fluid. 44

Figure 4.1 First frame of May 23rd video with hand-picked locations along the flume axis marked in red. Each location has a corresponding distance down-flume in p_i pixels and d_i in meters for $i \in \{1, ..., n\}$. These locations are used to form the warping function f for converting between distance in pixels to distance in meters. 60

Figure 4.2 (a) Warping function to convert distance in pixels to distance in meters down-flume for the May 25th video and (b) the uncertainty in the warping function. Warping uncertainty is larger up-flume since pixels represent a larger area at those locations in the video (see Figure 4.1) . . 61

Figure 4.3 (a) Illustration of the pixel color from all frames as a function of down-flume distance. At each frame index (row) in (a), the down-flume distance in pixels is converted to down-flume distance in meters using the warping function f in order to construct a (b) flow gather. Results are shown for the May 23rd debris-flow. Detailed images of the flow gathers on May 23rd and May 25th are shown in Figures 4.4 and 4.5 . . 62

Figure 4.4 Flow gather from the May 23rd experiment with overlaying flow-depth sensor data. Flow-depth data are plotted at their respective locations as red curves and are scaled for displayed purposes with increasing flow-depth to the right. The flow-depth appears to increase when roll waves (dark linear streaks in the flow gather) move past each flow-depth sensor. The dashed black outline shows the zoomed area displaying structure tensors in Figure 4.9. 63

Figure 4.5 Flow gather from May 25rd experiment with overlaying flow-depth sensor data plotted in the same fashion as Figure 4.4. We see that flow-depth appears to change with the appearance in the flow gather. Roll waves are visible as dark dipping features in the flow gather. The velocity of each roll wave can be quantified by the inverse slope of each dark dipping feature. 64

Figure 4.6 Flow gathers during May 25th experiment using (a) video and (b) lidar. The location of the front picked from video is plotted over each flowgather. We see that the features in (a) and (b) are similar for most times and distances down-flume. The largest difference in the arrival of the debris-front occurs around 10 seconds and distance of 70-80 m down-flume. 65

Figure 4.7 Vertical thickness as a function of time at flow-depth laser sensor locations (a) $d = 31.7$ m, (b) $d = 65.4$ m, and (c) $d = 80.0$ m for both lidar and flow-depth laser sensors. Lidar and flow-depth curves disagree since they sample a different location across the flume axis – especially at large distances down flume. The video-based flow front pick in red matches lidar-based flow front pick in green within fractions of a second, which can also be explained by the two sensors measuring the front location at different locations across the flume axis. 66

Figure 4.8 Flow front (a) position and (b) velocity for the May 25th debris-flow experiment according to video and lidar. The front position derived from video matches that derived from lidar with a mean front arrival time difference of -0.36 s. Front velocity from lidar and video appear as shifted versions of one another due to each sensor sampling slightly different positions along the flume axis. 67

Figure 4.9 Zoomed in view of structure tensors computed on the May 23rd flow gather. Zoomed in region is outlined by the dashed line in Figure 4.4. Structure tensors are plotted as magenta ellipses with the minimum eigenvector direction aligning with the major axis of each ellipse. Structure tensors with higher coherency are plotted with more intense color; low coherency structure tensors are plotted with more opacity. We see that in areas where structure is ambiguous, the coherency is low. In areas with strongly dipping structure the coherency is high. . . . 70

Figure 4.10 (a-c) Surface velocity estimates and (d-f) coherency values derived from flow gathers on (a & d) May 23rd and (b & e) May 25th experiments. (c & f) Surface velocity and coherency derived from lidar measurements on May 25th. Surface velocities derived from structure tensors with coherency below 0.2, below 1 m/s, or above 30 m/s are not displayed. . . 71

Figure 4.11 Empirical PDFs for (a) surface velocity and (b) coherency from lidar and video on May 25th experiment as shown in Figure 4.10. The distributions do not match exactly, but more low surface velocities are recovered by both sensors. Lidar tends to measure higher velocities, likely because it is a higher resolution instrument than video and measures geometric changes rather than appearance changes. Additionally, lidar-based structure tensors, in general, exhibit less low-coherency than video-based structure tensors as shown in (b). 72

Figure 5.1 (a & b) Examples of randomly generated 3D seismic signals. The signals shown have compact support in the interval [0.2, 0.8] s. We estimate the sensors motion model using measurements taken outside the seismic signals support, then infer it inside the seismic signal support using an assumed sensor motion model. 80

Figure 5.2 Map-view of simulated topography with varying smoothness; (a) no smoothing, (b) smoothing with σ_t=1, and (c) σ_t=2. Topography is translated by a seismic signal during our simulations and has the benefit of being randomly generated. 81

Figure 5.3 (a) Noiseless observation, (b) true seismic signal, and (c) estimated seismic signal. 87

Figure 5.4 (a) True seismic signal and simulated noisy observations for (a) $\sigma = 0.5$ mm and (b) $\sigma = 1.0$ mm. Solid colors in (c-f) & (g-i) show each component of the mean recovered 3D seismic signal; shaded regions show the standard deviation of the estimated signal. (c-f) Recovery with a noise level $\sigma = 0.5$ mm shows lower uncertainty than that recovered using (g-i) a higher noise level $\sigma = 1.0$ mm. 89

Figure 5.5 Derived SNR as a function of observational noise σ. We observe that SNR for $x-$ and $y-$ components are consistently lower than the $z-$ component SNR for noise levels below $\sigma = 1$ mm due to topography being mostly planar. We also observe that $SNR > 0$ for $\sigma < 15$ mm for all components. 90

Figure 5.6 Derived SNR as a function of platform rotation θ. We observe smaller SNR for x- and $y-$ components compared to the z-component due to topography being mostly planar; rotation affects the x- and y-components of the points on the ground more than the z- components. . 91

Figure 5.7 Signal-to-noise ratios for (a) x-, (b) y-, and (c) z-components of estimated seismic signal as a function of observation noise and peak signal amplitude. When the peak signal amplitude is close to the noise level we are able to recover the signal. Blue areas of each subplot denote $SNR < 0$ and indicate failure; red areas denote $SNR > 0$ and indicate success. We denote the failure boundary for each component using a solid black line in each subplot to indicate $SNR = 0$. Below the failure boundary our method succeeds to recover seismic signals. . . . 92

Figure 5.8 SNR maps for the x-, y-, and z- component of the estimated seismic signal as a function of σ and max signal peak for various $\Delta x = \Delta y =$ (a-c) 20 cm, (d-f) 10 cm, (h-j) 5 cm, and (k-m) 2.5 cm. We observe a general linear trend in the failure boundary at $SNR = 0$ marked as a black line on each subplot. These results imply that denser sample spacing results in higher SNR. We observe exception of for SNR values below $\sigma = 5.0$ cm where we see a nonlinear trend develop indicating no improvement in SNR with a decrease in σ. 93

Figure 5.9 Failure boundaries defining $SNR = 0$ for (a) x-, (b) y-, and (c) z-components for varying sample spacings ($\Delta x = \Delta y$). Note that the failure boundaries here are plotted on a linear scale to highlight the differences in the slope of the failure boundary. The slope of each line is noted in Table 5.1. We find that smaller sample spacings give steeper failure boundaries. This indicates that for a given noise level on the failure boundary we can observe signals will smaller max signal peaks if we make measurements with denser sample spacings. The failure boundary slope roughly doubles if we half the sample spacing. . . 94

Figure A.1 Permission statement for the Journal of Unmanned Aerial Vehicles paper published under Canadian Science Publishing hightlighted in blue. 110

Figure A.2 Permission statement for Journal of Geophysical Research - Earth Surfaces hightlighted in yellow. 111

Figure A.3 Permission statement from coauthor Elias Arias. 112

Figure A.4 Permission statement from coauthor Dr. Paul Sava. 112

Figure A.5 Permission statement from coauthor Dr. Francis Rengers. 112

Figure A.6 Permission statement from coauthor Dr. Kate Allstadt. 113

Figure A.7 Permission statement from coauthor Dr. Richard Iverson. 113

Figure A.8 Permission statement from coauthor Dr. Michael Olsen. 114

Figure A.9 Permission statement from coauthor Joel Smith. 114

Figure A.10 Permission statement from coauthor Maciej Obryk. 115

Figure A.11 Permission statement from coauthor Dr. Matthew Logan. 115

Table 5.1 Failure boundary slope for each component of the estimated seismic signal for various sample spacings ($\Delta x = \Delta y$). The slope of the failure boundary quantifies the relationship between s_{max} and σ along the failure boundary. Higher slopes indicate that a higher sensor noise level σ can still achieve a given s_{max}. 94

LIST OF ABBREVIATIONS

Distributed Acoustic System . . . . . DAS

Laser Doppler Vibrometer . . . . . LDV

Probability Density Function . . . . . PDF

Structure from Motion . . . . . SFM

ACKNOWLEDGMENTS

A warm thank you to the Geophysics (GP) department and the Center for Wave Phenomena (CWP) during the chaotic times these last few years. Thank you Pam, Dawn, Debra, and Michelle for your critical administrative support, you keep the GP department stable in the face of chaos on a daily basis. I thank the sponsor companies of CWP whose support made this research possible. I am grateful for the opportunity CWP presented me in pursuing this non-traditional thesis topic. To the GP faculty and students, thank you for your camaraderie, critiques, and coffee conversations.

I thank the U.S. Geological Survey collaborators and coauthors Francis, Kate, Dick, Joel, Maciej, Joel, Michael, and Matt. You all endured my novice questions related to landslides and I thank you for your patience and support. I thank you all for your help in the writing process within USGS and for the opportunity to work with such interesting videos of landslides.

I thank my committee members Andrei, Bill, Mike, and Whitney. I realize my thesis was an evolving work that changed many times and your approval and flexibility was critical in completing the thesis. Perhaps the most flexible of all was my advisor, Paul. I thank Paul for the opportunity, and the patience in pursuing airborne seismic. I especially thank Paul for the thought he put into reviewing the thesis components and for the regular thought provoking discussions on how to realize airborne seismic.

A warm thank you to my family, the sense of gratitude I feel for you all is unmatched. To Angie, David, Theresa, and Rich - your local support and family dinners brought me feelings of home. To my Dad whose comic encouragement and solid work ethic example propelled me forward. To my Mom whose love and understanding comforted and levelled me when low. To my brother, Jacob whose endurance in the face uncertainty put my struggles into perspective. To my sister, Becca who inspired me to follow through when it wasn't easy.

To my nonrelated brothers, Alex, Austin, Travis, Gabriel, and Elias you guys are invaluable and I consider you all family. To my wife, Natalya who inspired and supported me with love and unparalleled tenacity during these past four years of graduate school. To my son Leo, whose genuine curiosity and laugh bring light into my life everyday.

For my family

CHAPTER 1

INTRODUCTION

Earth's subsurface contains valuable resources for addressing energy and everyday material needs. An effective subsurface exploration strategy involves estimating subsurface composition and structure, a specialty of geophysicists. Geophysicists rely on physical measurements, such as measuring electromagnetic, gravity, or elastic fields, for inferring subsurface structures and compositions. For practical reasons, many geophysical measurements are made at the Earth's surface; although subsurface measurements can be made, for example, in mines or boreholes. Additional limitations on geophysical data acquisition may be caused by extreme topography, exploration in remote areas, or presence in an environmentally sensitive area. These data acquisition limitations can prevent subsurface exploration in places that would otherwise be desirable areas of study. In a similar way, geomorphologists who study landslides and debris flows are limited due to the remote, sudden, and dangerous character of such surface processes. Both geophysicists and geomorphologists utilize ground displacement and velocity time signals to conduct their respective studies. This thesis focuses on enabling rapid, remote, and subtle displacement and velocity measurements at the Earth's surface using remote video cameras, including cameras deployed using airborne platforms.

Modern camera sensors are able to quantify the intensity of light at unprecedented resolution in space and time. Cameras on smart phones are routinely used to measure the geometry of an object, for example by exploiting facial features to unlock phones. Advances in the field of computer vision enable this common luxury, but have also been applied in the earth sciences to study variations of the Earth topography. A popular technology called structure from motion (SFM) is commonly used to quantify the geometry of a particular scene using cameras [1, 2], and is increasingly being used to measure changes in topography [3–8]. In addition to achieving measurements with high spatial resolution, researchers are

pushing the limits in temporal resolution. One exciting development is a technique known as motion magnification, which exploits subtle variations in color to recover audio signals, heart beats, or even subtle infrastructure vibrations [9–13]. Beyond motion magnification, light itself is being imaged with clever techniques that tote a trillion frames per second in controlled laboratory settings [14]. Our ability to rapidly measure subtle variations in light intensity has never been better and our competency in rapidly processing such measurements is accelerating. In this high tech camera climate, an opportunity for measuring rapid and subtle ground displacement signals lives, and forms the foundation of this thesis.

I develop and apply ways to rapidly measure subtle displacement signals using high speed multi-view video. In contrast to previous work, I focus on enabling application in geophysics and geomorphology that involve ground displacement and velocity signals. My developments enable research in new places and in new ways using data of unprecedented spatial and temporal resolution. The thesis is composed of four papers unified by the goal of developing and demonstrating how rapid subtle ground displacement and velocity signals can be measured using remote multi-view video. Within each paper, I demonstrate how such measurements can be used to gain geophysical or geomorphological insight on the physics of earthquakes, landslides, or debris-flow processes at previously unobtainable temporal and spatial resolution.

Chapter 2 develops and demonstrates how drone-borne stereo cameras may be used to measure earthquake signals. I conclude that current camera technology is sufficient to measure large-motion earthquake signals of $\approx$ 1 mm in amplitude, but require that the drone position and orientation be known with sufficient accuracy. My conclusions pave the way for further development into drone-borne seismic data acquisition. However, in practice the drone position and orientation can not by known exactly; I remove the need for this assumption using the techniques in Chapter 5. The effect of airborne platform is a first order limitation for realizing rapid, subtle, airborne seismic acquisition. Before presenting the material in Chapter 5, I build increased confidence in measuring rapid, subtle

displacement signals by capturing remotely the motion of rapid landslides and debris flows, as reported in Chapters 3 and 4.

Chapter 3 focuses on measuring rapid subtle deformation of landslide failure using two video cameras. In contrast to Chapter 2, the material in Chapter 3 involves real videos that are not recorded in stereographic mode. The measurements of ground displacement obtained in Chapter 3 are at sufficient resolution necessary to compute spatial and temporal derivatives present in equations that describe landslide motion, for example in the depth-averaged debris-flow landslide motion model [15, 16]. Thus, the video-based measurements obtained in Chapter 3 are useful for estimating soil characteristics, such as soil dilation/contraction rates, that would otherwise require costly and potentially hazardous in situ pore pressure sensors [15, 16].

Chapter 4 develops a new technique for analyzing the position and velocity of a debris-flow front as well as its surface velocity, using a single video camera. The technique I develop requires prior knowledge of the scene geometry in order to deduce the geometry and speed of the debris-flow. The result of this technique is an image that resembles a seismic shot gather, so I call the image a flow gather. The flow gather image is described as a function of position and time and thus can be used to interpret the location and speed of various flow characteristics based on their surface appearance.

The method developed in Chapter 5 removes the problematic assumption of a known airborne platform position and orientation required in Chapter 2, and also the need to measure displacement with video cameras. I propose a novel method for removing the effect of platform motion from airborne measurements of ground displacement using reasonable assumptions about the mathematical model underlying the position and orientation of the airborne platform.

The thesis concludes with a common discussion of insight accumulated in each chapter and with speculation on future research directions in airborne seismic data acquisition.

CHAPTER 2

AIRBORNE SEISMIC DATA ACQUISITION USING STEREO VISION

A paper published in *Journal of Unmanned Vehicle Systems*

Thomas D. Rapstine[1,2], Paul Sava[2], and Elias Arias[3]

2.1 Abstract

Environmental impact and the high cost of acquiring land seismic data are major factors to consider when designing a seismic survey. We explore means to quickly record seismic data without disturbing, or contacting, the ground surface, while reducing environmental impact and cost. Recent developments in computer vision techniques and unmanned aerial vehicle (UAV) technology lead us to propose passively observing ground displacement with a UAV-borne stereo video camera system. The recovered displacement is represented as a time varying probability distribution function (PDF) of ground displacement. Using this PDF, we can estimate the uncertainty of the displacement measurements. We conclude that currently available camera and UAVs may be used to measure sub-millimeter ground displacements, with associated uncertainties.

2.2 Introduction

Geophysical survey design requires one to consider the environment, access, and acquisition cost. When operating in environmentally sensitive areas, it may not be possible to conduct a ground-based survey without disturbing an ecosystem. In addition, in remote locations a survey may not be feasible due to access or other logistical concerns. Financial limitations also influence data acquisition feasibility. Cost may be reduced by optimizing

[1]Primary researcher and author.
[2]Department of Geophysics, Colorado School of Mines, Golden, Colorado, United States of America.
[3]Spectraseis Inc.

survey design parameters such as seismic source geometry, source signal length and frequency content, and receiver spacing. Technological advancements can also reduce costs and potentially lead to new opportunities for exploration; an excellent example is distributed acoustic systems (DAS) [17–22]. We advocate in this paper, that recent developments in computer vision and robotics also have impact potential for seismic data acquisition, leading towards fast, low cost, and environmentally friendly airborne seismic surveying.

Monitoring motion without contacting a surface can be performed using passive or active systems. Laser Doppler vibrometers (LDV) are examples of active systems, which use known source signals and the phase of the return signals to deduce the distance the signal travelled to a target. LDV's have been used in the past to investigate the feasibility of remotely detecting ground motion from seismic waves [23, 24]. Other active systems uses microwaves, and interferometry, to deduce vibrations and resonant frequencies in a structural engineering context such as in [25]. In contrast to active systems, passive systems do not require a source for deducing motion and leverage high speed video cameras and ambient lighting. Here we focus on passive methods for deducing motion.

We advocate measuring ground displacement as a function of time using stereo vision theory. As our left and right eyes allow for depth perception, two images taken from laterally offset cameras allow for a distance estimate. Stereo vision has been used in the past to passively deduce distance using two images taken from laterally offset cameras [26]. We measure the lateral shift, or disparity, between points observed in the two images. As we show later, this disparity is inversely proportional to the distance from the camera to the points observed in the images. Therefore, the process of finding ground displacement from stereo images requires us to accurately compute perceived shifts between two images. The stereo vision process is discussed in more detail in the Theory section.

In this paper, we demonstrate and detail a method for sampling a seismic wavefield, represented by ground displacements, that has potential to reduce costs while providing new opportunities for geophysical exploration or earthquake monitoring. First, we clarify the

stereo vision theory used to determine ground displacement variations with time. Using the collection of ground displacement values, we construct a probability density function (PDF) of ground displacement, from which we deduce the uncertainty of our measurement. Lastly, we conduct a realistic computer graphics simulation of a real-life earthquake signal, demonstrating the feasibility of using stereo videos to recover sub-millimeter displacement signals, with associated uncertainties, from a moving airborne platform.

2.3 Theory

We aim to passively measure ground displacement, without touching the ground, and obtain an uncertainty estimate of our measurement. In this section, we provide a brief summary of how stereo vision is used to acquire a ground displacement measurement with associate uncertainty. The stereo vision theory we summarize is common in standard computer vision literature [27]. Stereo videos are represented as a sequence of frames taken from two offset cameras (left and right), as shown in Figure 2.1. This geometry allows one to acquire the distance to points viewed by the stereo cameras using geometric relations based on similar triangles and triangulation.

We begin by defining the origin of three coordinate frames representing the origins of the world, left camera, and right camera. It is our goal to consistently represent a PDF of ground position in the world coordinate frame using images from stereo cameras. In the world coordinate frame, we denote the world and left camera origin as ${}^{w}\mathbf{o}_{w} = [0,0,0]^{T}$ and ${}^{w}\mathbf{o}_{l} = [0,0,-h]^{T}$, respectively. We adopt the notation where preceding superscripts denote the coordinate frame of a point and subscripts denote the label of a specific point as w, l, and r for the world, left camera, and right camera coordinates, respectively. The z-axis of the world coordinate frame points down, a left camera is placed at a height h above the world origin. The right camera origin is placed a distance b away from the left camera in the x-direction and is noted by ${}^{l}\mathbf{o}_{r} = [b,0,0]^{T}$. We represent transformations between an arbitrary coordinate system a to another coordinate system b using a 4×4 matrix ${}^{b}_{a}\mathbf{H}$. This matrix may be obtained by augmenting the rotation matrix from coordinate system a to b,

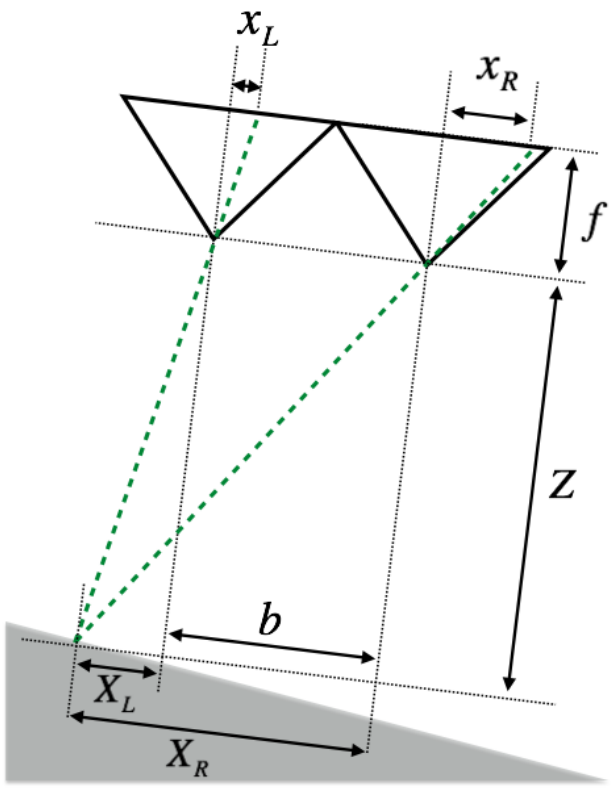

Figure 2.1: A schematic of stereo cameras viewing the ground from above. The dashed paths show where a point on the ground projects on the left and right cameras, each with focal length f. The cameras optical axis are aligned and separated by b.

denoted ${}^b_a\mathbf{R}$, with the origin of a in b, denoted ${}^b\mathbf{t}_{a,org}$

$$ {}^b_a\mathbf{H} = \begin{bmatrix} {}^b_a\mathbf{R} & {}^b\mathbf{t}_{a,org} \\ \mathbf{0} & 1 \end{bmatrix}. \tag{2.1} $$

We use a homogeneous point representation in order to apply rotation and translation of a point using a single matrix-vector multiplication. A point $\mathbf{x}$ in 3D space may be represented in homogeneous coordinates as a four-element point $\tilde{\mathbf{x}}$ by appending a fourth arbitrary element to $\mathbf{x}$. We represent a point $\mathbf{x}$ in homogeneous coordinates using the notation $\tilde{\mathbf{x}}$, and note that homogeneous coordinates that are scalar versions of one another are considered equivalent points in 3D space. We may obtain the original coordinate from the homogeneous coordinate by dividing by the fourth element:

$$ \tilde{\mathbf{x}} = \begin{bmatrix} x_1 \\ x_2 \\ x_3 \\ x_4 \end{bmatrix} \rightarrow \mathbf{x} = \begin{bmatrix} \frac{x_1}{x_4} \\ \frac{x_2}{x_4} \\ \frac{x_3}{x_4} \end{bmatrix}. \tag{2.2} $$

With homogeneous coordinates, we can transform the right camera origin from the left camera frame to the world frame by

$$ {}^w\tilde{\mathbf{o}}_r = {}^w_l\mathbf{H}\,{}^l\tilde{\mathbf{o}}_r. \tag{2.3} $$

In general, a point in the right camera frame is transformed into the world coordinate frame using

$$ {}^w\tilde{\mathbf{x}} = {}^w_r\mathbf{H}\,{}^r\tilde{\mathbf{x}}. \tag{2.4} $$

Stereo vision allows us to determine the 3D location of a point $\mathbf{p}$ observed using the left and right cameras. We can represent the point in the left or right coordinate frames as ${}^l\mathbf{p} = [X_l, Y_l, Z_l]^T$ or ${}^r\mathbf{p} = [X_r, Y_r, Z_r]^T$, respectively. We note that $Z_l = Z_r = Z$ since the camera origins are only separated in the x-direction of the right camera frame. Using stereo vision, we find ${}^r\tilde{\mathbf{p}}$ then transform the point to the world coordinate frame using ${}^w\tilde{\mathbf{p}} = {}^w_r\mathbf{H}\,{}^r\tilde{\mathbf{p}}$. The 3D location of the point ${}^r\mathbf{p}$ is found using the pixel coordinates where the point is observed in the left and right cameras denoted (x_l, y_l) and (x_r, y_r), respectively. Projecting a 3D point, such as ${}^r\mathbf{p}$, onto a 2D image can be described using a pinhole camera

model, which assumes that all 3D points project onto the image plane of a camera through a single point, or pinhole. The model is appropriate to use when a camera has been calibrated to remove lens distortion, which is commonly performed on images (we assume all images are calibrated). Figure 2.1 shows a point projecting onto the left and right image planes using the pinhole camera model. We use similar triangle geometry to express the left and right x-pixel coordinates of the point as a function of the camera focal length f, in pixels, and the distance to the point Z

$$\begin{aligned} \frac{x_l}{f} = \frac{X_l}{Z} \rightarrow x_l = \frac{fX_l}{Z} \\ \frac{x_r}{f} = \frac{X_r}{Z} \rightarrow x_r = \frac{fX_r}{Z}. \end{aligned} \tag{2.5}$$

The shift of the 3D point, as observed by left and right cameras, known as disparity, is then

$$d = x_r - x_l = \frac{fX_r - f(X_r - b)}{Z} = \frac{fb}{Z}. \tag{2.6}$$

We note that the shift is an integer since the pixel coordinates are integers. The distance, in the z-direction extending from the cameras, can be used to deduce the x and y-coordinates of ${}^{r}\tilde{\mathbf{p}}$

$$\begin{aligned} X_r = \frac{Zx_r}{f} \\ Y_r = \frac{Zy_r}{f}. \end{aligned} \tag{2.7}$$

Finally, the 3D point in the right camera coordinate system can be transformed into the world coordinate frame by converting to homogeneous coordinates and applying a coordinate transformation ${}^{w}_{r}\mathbf{H}$

$${}^{r}\mathbf{p} = \begin{bmatrix} X_r \\ Y_r \\ Z \end{bmatrix} \rightarrow {}^{w}\tilde{\mathbf{p}} = {}^{w}_{r}\mathbf{H}\,{}^{r}\tilde{\mathbf{p}}. \tag{2.8}$$

Determining the 3D world coordinates of a point ${}^{w}\mathbf{p}$ therefore requires us to know the camera separation b, the focal length of the camera f, the disparity d of points, and the

coordinate transformation ${}^{w}_{r}\mathbf{H}$. It is common for the camera separation and focal length of a stereo system to be known. However, it is more difficult to know the disparity and coordinate transformation than b and f.

The disparity may be found using a variety of methods. In general, there are two main categories of disparity algorithms that use sparse or dense point correspondence. Sparse methods track a limited number of features in an image and have been in development since the 1970's [27], whereas dense methods compute disparities for every pixel within an image [28]. The theory we adopt here is applicable regardless of the disparity method chosen. We choose to determine the disparity using a dynamic programming solution for finding shifts in images known as Smooth Dynamic Image Warping (SDW) [29]. SDW extends Dynamic Image Warping (DIW) [30] by recovering sub-sample shifts. We choose the SDW algorithm because it provides dense and sub-pixel disparity values for each pixel in an image. As a dynamic programming approach to finding shifts between two images, SDW works by minimizing a constrained nonlinear optimization problem. In summary, SDW determines shift values between two images that may be used to 'warp' one image to the other. In our context, we determine shifts between the left and right stereo images. Given that the cameras are only separated in the x-direction, the shift between images will only be in the x-direction. Therefore, we estimate 1D shifts between corresponding rows in left and right images. We note that estimating 2D shifts provides more constraints to the optimization problem and may be beneficial; however, we use 1D shifts in this paper for simplicity and computational efficiency. We can denote the image rows as vectors $\mathbf{l}$ and $\mathbf{r}$ where each element of $\mathbf{l}$, denoted l_i, is approximately an element in $\mathbf{r}$, r_{i+d_i}

$$l_i \approx r_{i+d_i} \; for \; i = 1, ..., W, \tag{2.9}$$

where W is the width of the image in pixels and d_i denotes the disparity used in equation 2.6 to determine the 3D point which projects onto pixel i. We estimate the disparity for all pixels in a row, and therefore recover a dense set of 3D point coordinates using SDW. In practice, we minimize the error between $\mathbf{l}$ and a shifted version of $\mathbf{r}$; SDW minimizes

absolute error, which results in shifts that express how each element of $\mathbf{r}$ may be shifted to in order for a match $\mathbf{l}$. The details of how the SDW minimization problem is implemented are beyond the scope of this paper but can be found in [30] and [29]. After finding the disparity using SDW, we obtain the 3D location of a point represented in the right camera coordinate frame from equations 2.6 and 2.7.

The cameras may be translating and rotating relative to the world coordinate frame while the stereo video is being recorded, for example, if the cameras are mounted on a hovering UAV. It is necessary to examine the 3D points in a consistent coordinate frame, therefore we require the coordinate transformation ${}^{w}_{r}\mathbf{H}$ for each frame of the video. This coordinate transformation may be provided from an onboard IMU, which uses accelerometers and gyroscopes to monitor position and orientation. In addition, other sensors, such as GPS may be used to monitor the camera motion during flight.

Many points on the ground are simultaneously viewed by the stereo cameras, and therefore we may statistically represent the position of the ground viewed by the system as a Probability Density Function (PDF). This representation of the ground assumes that between frames, all points undergo the same translation. A PDF of ground position is therefore available for each frame in the stereo video, which provides quantitative uncertainty information of the ground position. The PDFs change between frames as the ground and cameras move, however we may isolate the ground and camera motion by measuring and removing the camera motion. To remove the camera motion, we perform a coordinate transformation from right camera to world coordinate frame using equation 2.1 to form ${}^{w}_{r}\mathbf{H}$ for a particular frame. We note that the transformation matrix ${}^{w}_{r}\mathbf{H}$ contains camera motion information that is independent of the ground motion e.g. from an IMU. After camera motion is removed, we obtain a PDF from the collection of points representing the position of the ground in a consistent coordinate system as it varies with time. Summary statistics, such as the mean, may be computed from the collection of points to provide us with a 'trace' that represents ground motion. Similarly, we may compute the variance of point positions as a proxy for

the uncertainty of our measurements. Therefore measurements of the ground position, with associated uncertainty, are available from images of the ground taken remotely.

2.4 Numerical examples

We asses the feasibility of measuring ground motion with a UAV-mounted stereo vision system using realistic virtual simulations. Virtual simulations provide flexibility and precise control of UAV and ground motion, allowing us to simulate various UAVs, cameras, and ground motion signals. By using simulations, we know true ground and camera motion, can be compared to the recovered motion using stereo vision. We simulate two cameras separated by $b = 30$ cm in the x-direction of the left camera frame. Each camera has a focal length of 4.15 mm, a resolution of 1280×720 pixels, and an image sensor element size of 3.75 microns. These camera parameters are feasible and common, and were chosen to reflect current smartphone cameras. The cameras view a simulated moving ground surface from a height of 2 m, a reasonable height for a UAV hovering above the ground.

The vibrating ground surface is described by texture and topography (2.2) representing cracked clay. The appearance of cracks in the images intentionally does not reflect the true cracks in the ground surface in order to show that the recovered disparities are influenced by the topography, rather than by appearance.

An earthquake signal (Figure 2.3) recorded at USGS station OK034 in the fall of 2016 near Cushing, Oklahoma is used to displace the surface [31]. We note that the displacement of the signal is on the order of 3 mm, with many displacements below 1 mm. The vibrating ground surface is observed using the virtual stereo cameras, which hover above the ground (see Figure 2.3) as if mounted on a UAV. Next, we present recovered ground displacement results with and without drone motion.

We first show displacement recovery when the UAV is stationary. Videos are rendered for both the left and right cameras as the ground moves vertically according to the vertical ground displacement curve shown in Figure 2.3. Dense disparity values are computed at each time step, which are used to construct a PDF representing the ground location as viewed

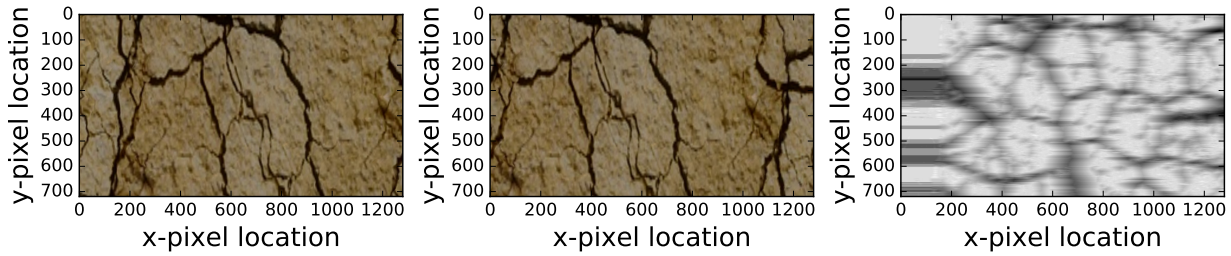

Figure 2.2: Left, right, and disparity image examples for the earthquake simulation (shown left to right, respectively). Note the left and right images are shifted versions of one another. The shift is quantified in the disparity image on the far right; smaller (darker) disparity values are farther away from the camera and indicate cracks in the ground.

from the stereo cameras. When estimating disparities using the SDW algorithm, we use a sub-sample precision of $\frac{1}{50}$ and a strain range of ± 0.02. The strain range chosen is low and narrow because of prior knowledge we posses: the disparities we seek are smoothly varying along a row. A wider strain range allows for more rapidly varying shifts along a row, and may be more appropriate when viewing a rugged surface. Here, the simulated ground is relatively flat, thus implying that the observed shifts vary smoothly.

The SDW sub-sample precision is chosen to be sufficiently small for recovering minute shifts between left and right images. We note that a higher sub-sample shift precision may be used, at the expense of an increase in computational memory requirements, however one may not observe benefits beyond a certain sub-sample shift precision value [29]. In contrast, choosing too low of a sub-sample shift precision value may lead to poor shift recovery. We test larger sub-sample precision values and find little benefit beyond $\frac{1}{50}$. The sub-sample shift value is best estimated by performing disparity computations on the first frame of the video and examining the recovered shifts. If the recovered shifts vary wildly, or seem discontinuous, then a higher degree of sub-sample precision may be required. We note that if computational time and memory is not an issue, then one may set the value of sub-sample

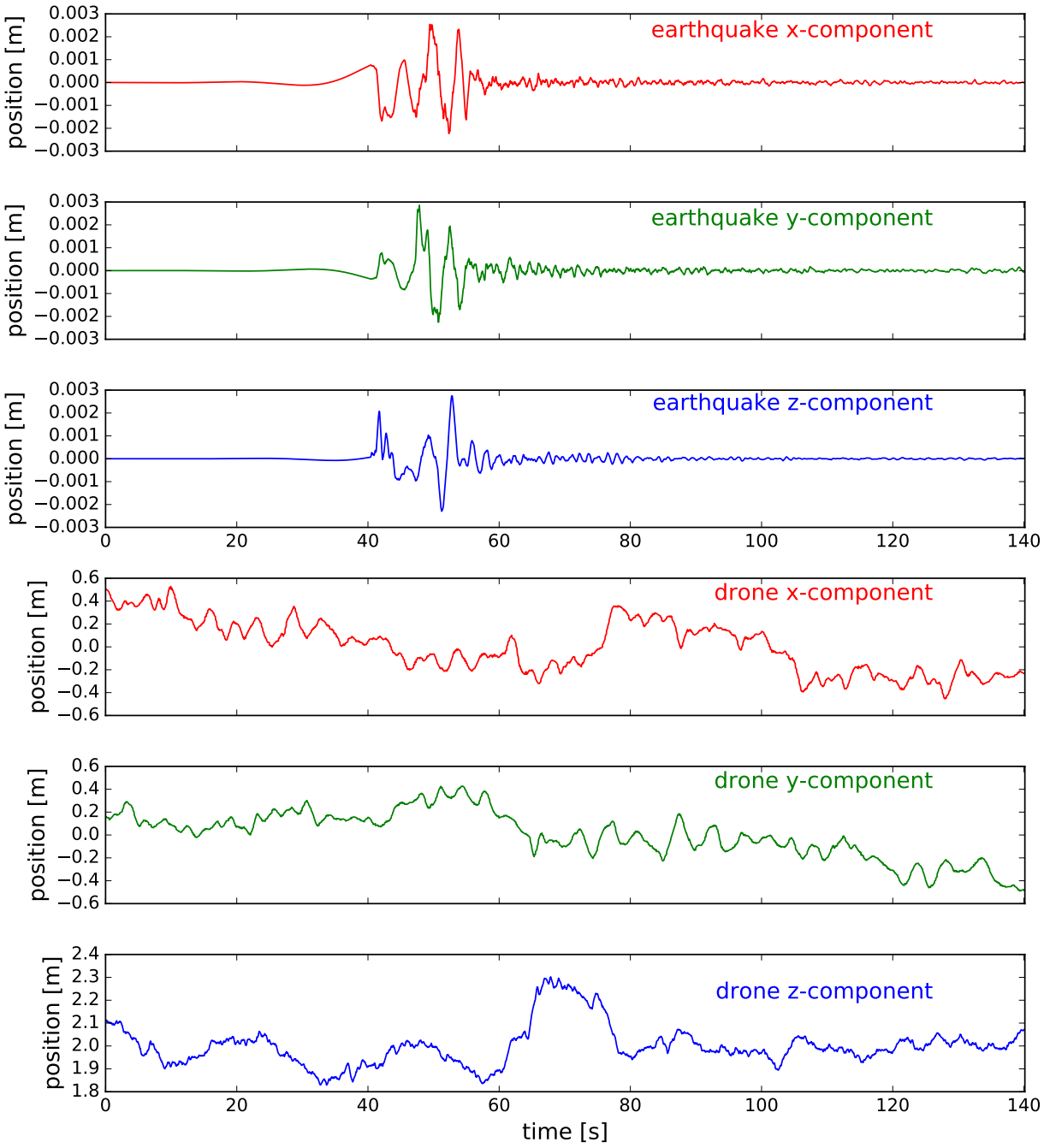

Figure 2.3: Earthquake (top three plots) and UAV motion (bottom three plots) used in hovering UAV simulation. The red, blue, and green curves show x, y, and z positions. Earthquake data is recorded ground motions for the 2016 (M5.0) earthquake near Cushing, Oklahoma at USGS station OK034. We note that the UAV motion is three orders of magnitude larger than the earthquake signal we wish to recover.

shift very high without risking the accuracy of recovered shifts. An example of recovered disparities for the first frame is shown in Figure 2.2. Note that the recovered disparities are somewhat smooth along a row, and they resemble cracks which reflect the cracks in the simulated ground surface.

The top plot in Figure 2.4 shows the recovered point location PDF in world coordinate frame for each frame in the video. The PDF gives insight on the statistical characteristics of our measurement. The PDF is smooth, broad, and contains horizontal bands. The horizontal banding in the recovered PDF is present due to discrete disparity values recovered using SDW, which are of limited precision. Regardless, we observe in the top plot in Figure 2.5 that the recovered ground displacement, after subtracting the initial distance to the ground, traces the true displacement of the ground surface. The true and observed displacement curves are on top of one another, which shows that the signal has been recovered well. The error, for this example, has a standard deviation of 0.011 mm. The standard deviation of the error is about a hundredth of a millimeter; five orders of magnitude less than the height at which the measurement was taken (h=2 m).

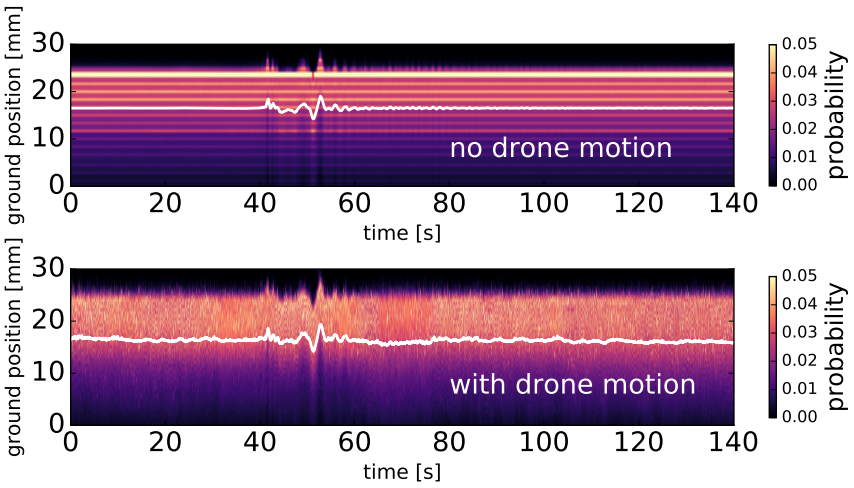

Figure 2.4: Recovered ground position PDF (top) without and (bottom) with UAV motion. White curve shows the mean value of ground position, which resemble the vertical ground motion from the simulated earthquake.

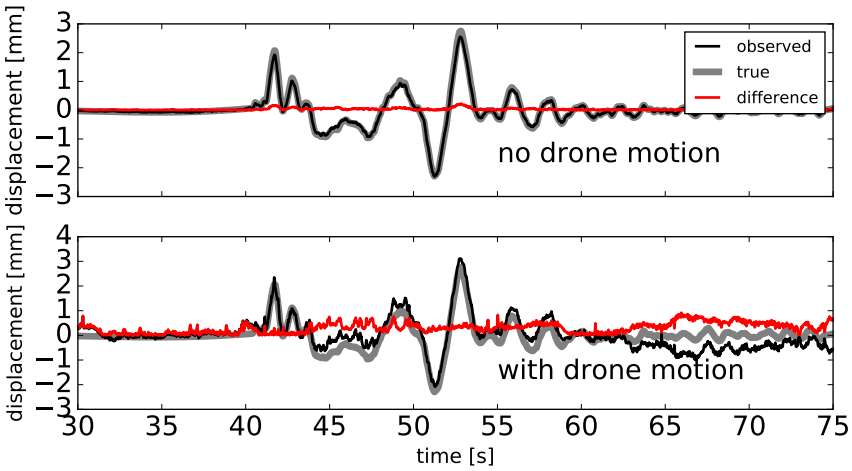

Figure 2.5: Recovered ground displacement signal compared with true displacement (top) without and (bottom) with UAV motion. Red curves show the absolute difference between recovered and true ground motion. Drone motion influences the recovery of the input signal.

We repeat the experiment with a moving UAV and the same ground motion signal. When the UAV is moving, the range of disparity values we must search through using SDW is considerably larger, making disparity estimates more computationally costly. We simulate UAV motion which resembles real-life motion we measured from a DJI Matrice 100 UAV. The UAV was instructed to hover at a fixed position for about two minutes; roughly the time spanned by the earthquake signal in Figure 2.3. The UAV moves a considerable amount during the simulation, roughly a quarter of a meter; this variation is orders of magnitude larger than the earthquake signal we wish to recover. The recovered PDF of point location in world coordinates for this second experiment is shown in the bottom plot of Figure 2.4. We note that the banding observed in the PDF for the first experiment is not present in the PDF for second experiment because of the coordinate transformation we use to correct for UAV motion. However, we see their remnants as scattered peaks in the recovered PDF which seem to mimic the vertical motion of the UAV. The errors present when the UAV is moving are larger than when the UAV is stationary, we observe an error standard deviation of 0.30 mm. Based on our results, we conclude that a stereo camera can feasibly measure earthquake-like sub-millimeter ground motion. The simulation parameters we use reflect

realistic UAV and camera parameters.

2.5 Conclusions

The UAV motion, earthquake motion, and camera specifications used in this work reflect real-life data. We assume known UAV position during acquisition, which may be available from IMUs and GPS. A dense disparity algorithm leads to many estimates of ground position at a given time, in turn allowing access to a statistical representation of ground position. We note that sub-pixel disparity estimates, provided by the disparity algorithm, are necessary to characterize the subtle earthquake ground motions. The strategy for disparity estimates used here dose not provide point correspondence in time, and therefore does not allow us to recover lateral ground displacement.

In general, current hardware and software limitations prohibit the practicality of a commercial large-scale UAV-borne exploration seismic acquisition system. The ground motion occurring during a exploration seismic survey is expected to be two to three orders of magnitude lower than the motion of an earthquake signal. Therefore, applying our current method to exploration seismic will require more sophisticated camera systems with higher resolutions and larger camera offsets. In addition, the seismic exploration scenario demands a more accurately known UAV position.

In terms of hardware, it is reasonable to assume UAV and camera systems will continue to improve, allowing for more detailed images and more precise UAV positioning systems, which result in more accurate and precise ground motion measurements. In terms of software, the disparity estimate algorithm may be modified and improved. More consistent and accurate disparities may be found by including information between video frames in addition to information within a video frame. Future and ongoing work focuses on augmenting our current method to recover lateral ground displacement and rotation, and on evaluating the use of fiducial markers and a single camera system to deduce ground motion. Based on current results, we conclude that UAV-borne stereo cameras can potentially be used to measure seismic signals, with associated uncertainties.

2.6 Acknowledgments

We thank the sponsor companies of the Center for Wave Phenomena, whose support made this research possible. We thank Matt Bailey and Ross Bunker for help acquiring UAV position data. Lastly, we acknowledge using the open source computer graphics engine Blender for our videos, and appreciate those who contributed to its creation.

CHAPTER 3

RECONSTRUCTING THE EVOLUTION OF A RAPID LANDSLIDE USING MULTIVIEW VIDEO

A paper submitted to *Journal of Geophysical Research: Earth Surface*

Thomas D. Rapstine[1,2], Francis K. Rengers[2], Kate E. Allstadt[2], Richard M. Iverson[2], Joel B. Smith[2], Maciej K. Obryk[2], Matt Logan[2], Michael J. Olsen[3]

3.1 Abstract

Non-contact measurements of spatially varied ground surface deformation during landslide motion can provide important constraints on landslide mechanics. Recent advances in technologies such as InSAR, lidar, and structure-from-motion (SfM) photogrammetry have made such measurements possible for landslides that move slowly or incrementally. On the other hand, analogous non-contact measurements have remained elusive for the most lethal landslides – those that fail abruptly and accelerate downslope at rates 1 m/s^2 or more – because many technologies are incapable of making measurements at sufficiently high rates. Here we present and test a new method for extracting the requisite high-speed measurements using sequences of stereo images obtained from a pair of inexpensive, stationary video cameras with nominal frame rates of 30 s^{-1}. The method combines elements of SfM with those of Particle Image Velocimetry (PIV) to extract data on 3-D evolution of the ground surface during slope failure. We apply the method to video images obtained during an experiment at the USGS debris-flow flume in which a high-speed, liquefying landslide was triggered by gradually adding water to a 6 m^3 prism of loosely packed sediment on a 31° slope. During the experiment we additionally used a lidar scanner configured in strip-scanning mode to

[1]Primary researcher and author.
[2]Department of Geophysics, Colorado School of Mines, Golden, Colorado, United States of America.
[2]United States Geological Survey
[3]Oregon State University

collect high-speed data on the evolution of a 2-D longitudinal transect of the ground surface. The lidar measurements corroborate our video-derived measurements. However, the video measurements have the advantage of portraying the entire ground surface – rather than just a longitudinal transect – and they were obtained using equipment of very low cost. Additionally, we use these new measurements to estimate dilation rates within the sediment that show detailed evolution of dilation and contraction as failure occurs. Our results indicate that the sediment did not behave as an incompressible fluid during failure.

3.2 Introduction

Landslides and debris flows can negatively impact people and infrastructure, but impacts might be mitigated if mathematical models can be used to make accurate predictions of landslide behavior. However, before models can be trusted to make reliable predictions, they must first be tested against data obtained in field studies and controlled experiments. One of the greatest challenges in data acquisition entails measuring changes that occur during the onset of abrupt slope failure that leads to rapid landsliding. This type of landslide motion generally occurs with little warning, yet spatially and temporally dense data are needed to reveal the character of the process (e. g., [32]). Recent advancements in computer vision and camera technologies hold great promise for acquiring such data because they enable measurements of landslide surface displacements at high spatial and temporal densities but low cost. In this study we demonstrate the feasibility of this approach by extracting 3-D surface displacement data from imagery acquired with two inexpensive high-resolution (4K) video cameras during a large-scale landslide experiment conducted at the U.S. Geological Survey debris-flow flume in 2017. We establish a testable hypothesis given the new ability to observe spatially and temporally dense displacements: Can surface displacements and velocities be used to derive soil dilation rates that agree with dilation rates derived using in situ pore pressure sensors?

Previous investigators have used a wide variety of methods to measure landslide motion, including both surface and subsurface motion, but here we focus on non-contact methods

used to measure surface displacements. The breadth of technologies used in this context includes satellite radar and optics [33], repeat photogrammetry [34], UAV-borne synthetic aperture radar (UAVSAR) [35], ground-based interferometric synthetic aperture radar (InSAR) (e. g., [36–38]), and lidar [39, 40]. The spatial and temporal resolution required to measure specific types of landslide movement influences the choice of technology used for monitoring. For example, satellite-based radar and repeat photogrammetry methods provide spatially dense and extensive information with temporal resolutions of days to years and are therefore most appropriate for measuring the behavior of large slow-moving landslides. In contrast, rapid motion during sudden slope failures requires high spatial and temporal resolution, which can be accomplished with lidar [40]. For example, in a recent experiment by Rengers et al. [41] high-rate lidar scans recorded along a narrow transect were used to track a debris flow front during an experiment at the U.S. Geological Survey debris-flow flume. Aside from this experiment, to our knowledge, there has not been an application of lidar or any other measurement that captures slide movement with both as high spatial resolution (order mm) and high temporal resolution (order seconds). However, the extent of current high temporal lidar data is currently limited to a narrow transect. In contrast, the work we present here measures surface displacement and velocity on a distributed surface, with time resolution tenths of a second, with cheaper instruments.

The technique we describe shares some features with standard stereo photogrammetry and structure-from-motion (SfM) methods. Recent detailed studies have used these methods to measure displacement for quantifying deformation (e. g., [42]) before and after a landslide event using repeat surveys several months apart. In contrast, the work we present here measures landslide deformation every few tenths of a second using multiple static video cameras and a modified SfM approach. Standard application of SfM involves a single camera viewing a static scene from many different viewpoints. Multiple images from each view point are used to reconstruct the scene geometry. The SfM process begins by quantifying image features at key pixel positions in each image, often called keypoints, using a descriptive array

of numbers, commonly called descriptors. Descriptors between each image are compared to one another to identify corresponding keypoints. Keypoint pixel locations are simultaneously processed to estimate the intrinsic camera parameters, the camera pose at each viewpoint, and a sparse 3-D geometry of the scene. Parameters intrinsic to the camera are focal length, sensor pixel size, and lens distortion parameters. After the camera poses are estimated, they are fixed, and a denser 3-D scene geometry is recovered up to an unknown scale factor. The scale factor can be found by specifying the location of surveyed ground control points within the images. In this way, a georeferenced 3-D geometry of a static scene can be found using a single camera. Further details of this approach can be found elsewhere [27, 43]. Despite excellent spatial resolution, SfM observations rely on repeat surveys of a static scene, which typically give temporal resolutions ranging from days to years. On the other hand, landslide dynamics may evolve rapidly, and measuring them therefore requires higher temporal resolution, such as that provided by video imagery.

Motion tracking techniques with high temporal resolution commonly utilize repeat images or video frames to observe markers in a moving medium. The moving markers, natural or man-made, provide a visible proxy for velocity between each video frame. A common technique for measuring velocity is the particle image velocimetry (PIV) method [44]. SfM and PIV are related and complementary computer vision methods. Conceptually, the markers used in PIV hold a similar purpose to the keypoints used in SfM; both the markers and keypoints are the primary sources required for recovering the geometry of a scene. SfM aims to recover geometry of a static scene, whereas PIV aims to extract time-varying geometry from repeat images. Numerous successful PIV applications utilize one or more cameras, and often utilize prior scene geometry information, such as surveyed marker locations. Some recent PIV applications involve measuring stream flow from drone platforms [45] and measuring stream discharge [46].

Stereo video also provides spatially and temporally dense information, but it does not require physical markers within a moving medium. Stereo video and PIV have recently

been used to monitor motion at a range of spatial and temporal scales to study debris flow front evolution [47, 48], snow avalanches [49], flooding stream beds [50], and laboratory-scale channel flows [51]. Our study is most similar to that conducted by Berger et al. [48], which involved a stereo camera setup triggered by upstream seismic sensors and measured the geometry of a debris flow front at a rate of 1 Hz over 10 minute periods. Increasingly, flow tracking studies avoid the longstanding compromise between temporal and spatial resolution by jointly utilizing stereo vision and tracking methods.

Modern stereo vision and tracking methods enable landslide surface motion measurements to be acquired at previously unattainable spatial and temporal resolutions at low cost. Herein we describe, apply, and verify a new technique for measuring landslide surface motion at high temporal and spatial resolution using multiview video imagery. Moreover, we focus on observing landslide initiation to better understand how sediment naturally fails in response to rising pore-water pressure. Using our new approach we obtain centimeter scale spatial resolution of a mass-failure at a temporal resolution of 30 s^{-1}, which allows us to quantify 3-D surface velocities as the sediment mass transitions from soil creep to progressive failure, and then a retrogressive failure. We link surface displacement and velocity observations to subsurface hydrology by showing that they are related to soil dilation and contraction within a failing sediment mass.

3.3 Methods

3.3.1 Experimental setup

The observations analyzed in this paper occurred on 17 May 2017 at the U.S. Geological Survey debris-flow flume during a natural-release experiment in which slope failure was triggered by gradually adding water to a static prism of sediment positioned behind a retaining wall (e. g., [52, 53]). The debris flow flume is a rectangular chute that measures 82.5 m long, 2 m wide, and tilts at a 31° angle from horizontal. The flume enables repeatable observations in a controlled setting [54]. Many previous natural-release experiments have been conducted at the flume to better understand physical processes governing landslide initia-

tion [32, 52, 53, 55] and to test models describing landslide dynamics [15, 54, 56]. In our experiment, 6 m^3 of thoroughly mixed, uncompacted sediment consisting of 75% sand and 25% loam by volume was placed behind a rigid, 65-cm-high retaining wall installed normal to the flume bed (Figure 3.1). The emplaced sediment had the form of a rectangular prism, except at its upslope end, which was tapered (Figure 3.1). For convenience we use the term "sediment prism" to denote both the initial static sediment body as well as the sediment body as it begins to move and deform. Colored rocks were placed on the sediment prism surface (Figure 3.2). Instrumentation within the sediment prism included pore pressure sensors as labeled in Figure 3.1. A video summarizing the experiment may be viewed online at https://pubs.usgs.gov/of/2007/1315/videos/2017/2017_05_17.mp4 [57]. During the experiment, water was initially applied on the surface of the sediment prism for 12 minutes, then after 2 minutes ground water application began. Slope failure occurred after 50 minutes of subsurface watering. The sediment prism failure resulted in a rapidly moving mass of sediment cascading over the retaining wall (Figure 3.2) as viewed in the videos provided by Logan et al. [57].

We analyze observations within a frame of reference in space and time relative to the sediment prism geometry and time of failure. We denote time as t_f, and define $t_f = 0$ to be at the approximate failure time; negative times precede failure and positive times occur after failure. We approximate failure time to be when the average sediment prism surface displacement along a lidar transect, relative to the elevation of the sediment prism surface at the beginning of the videos, exceeds 5 mm. For spatial reference, we define the origin $x = y = z = 0$ to be at the center of the retaining wall that supports the sediment prism (Figure 3.1). The positive z axis points upwards and is synonymous with elevation. The positive x axis is horizontal, being level with the ground surface, and is orthogonal to the z axis. We stress that x is not parallel to the flume surface, x is horizontally level. The positive y axis points across the sediment prism such that it is orthogonal to the x and z axes. Many results in the paper are represented as a change in elevation relative to the initial

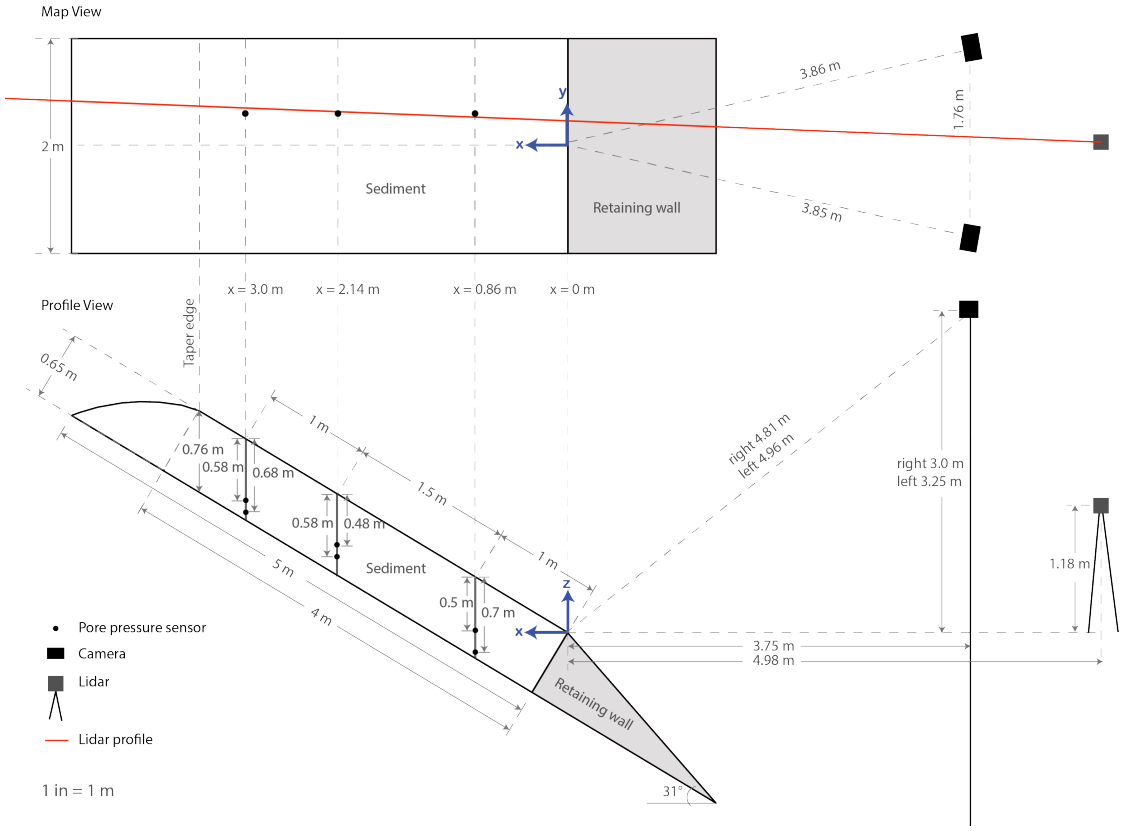

Figure 3.1: Schematic of the sediment prism and sensor layout during the experiment.

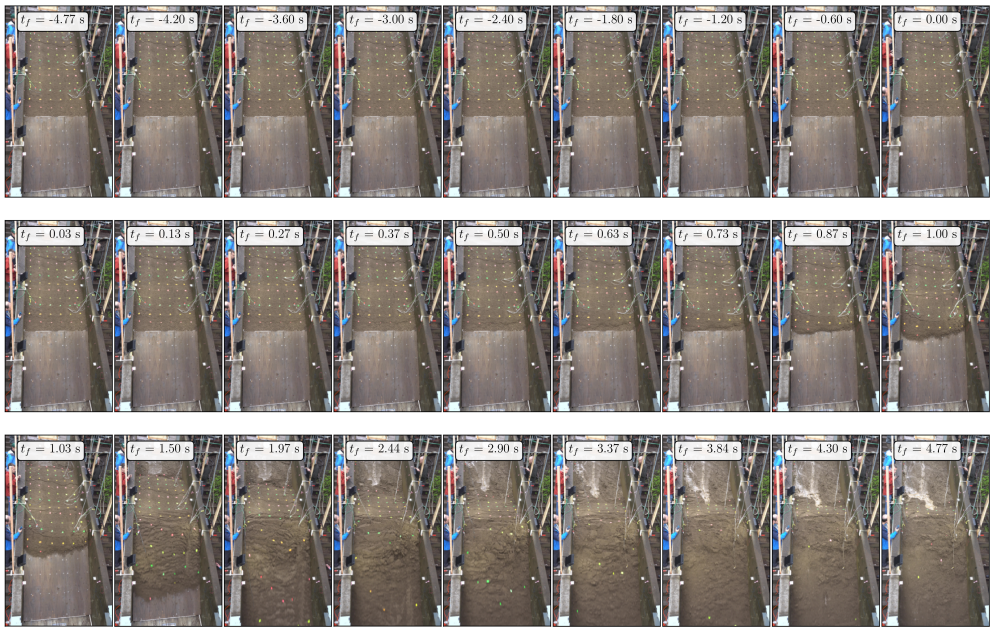

Figure 3.2: Views of the sediment prism from one video camera near failure time ($t_f = 0$). Failure occurs rapidly over a few seconds which calls for rapid measurements of surface deformation.

elevation at the sediment prism surface, we denote vertical displacement as Δz. Velocities in the direction of x and z are denoted as v_x and v_z, respectively. We represent observations of surface geometry, velocity, and sediment dilation rate within this frame of reference.

3.3.2 Reconstructing a dynamic 3-D surface from images

The dynamic 3-D geometry of the deforming ground surface was reconstructed using videos from two cameras. We used two Sony α6300 cameras each outfitted with Sony SELP1650 16-50 mm lenses to observe the sediment prism at oblique angles during the experiment. The cameras were mounted a few meters above the sediment prism and separated by a distance of 1.76 m. The precise camera pose, defined by camera position and orientation, was not recorded in the field. Each camera was manually triggered and recorded 4K (3840×2160) resolution videos at 29.97 fps for roughly 30 minutes leading up to failure (see Figure 3.2). The camera focal length was not captured in the video Exchangeable Image File Format (EXIF) metadata, so in our analysis we consider focal length unknown yet

fixed. The videos were roughly aligned in time but not exactly. However, a timing light was visible in each of the two Sony videos; the lights were triggered at known Universal Time Coordinated (UTC) times. In addition, audible hammer seismic strikes were recorded as audio within the videos. Six surveyed photogrammetric markers were also visible in the videos (Figure 3.1). The timing light, video images and audio, and hammer seismic strike UTC times provided sufficient information to synchronize the video timing before deploying computer vision techniques for quantifying the evolution of the sediment prism surface geometry.

Temporally aligning each video, in a relative sense, was a first order requirement for 4-D (x,y,z,t) reconstruction to succeed. Misalignment by even half a second resulted in erroneous results, especially during dynamic failure, since during this amount of time a considerable amount of motion could occur in the video. Each of the two videos were temporally aligned to one another using color and audio signals from the timing light and hammer seismic strikes, respectively. Color-based alignment was achieved by recording and aligning the pixel color intensity of the timing light in each video. We computed color intensity as the summation of red, green, and blue color channel pixel values associated with the timing light (Figure 3.3a). When the timing light turned on, the intensity rapidly increased, remained constant, then rapidly decreased as the light turned off. This off-on-off pattern was observed in the intensity curves from both videos, but appeared at different frame indices. The frame shift corresponding to the maximum cross-correlation coefficient between the two curves provided an appropriate shift in frames between videos for temporal alignment. The voltage of the timing light was recorded with the associated UTC time stamps, which allowed the relatively aligned frames to be associated with a UTC time. Similarly, we achieved a second estimate of a relative time shift and UTC time using the audible hammer seismic strike (Figure 3.3b). The sound of the hammer strike was quantified as a 48,000 Hz digital audio signal embedded in each video. The high sample rate of the audio signal provided excellent temporal precision for picking the hammer strike time using the same cross-correlation approach.

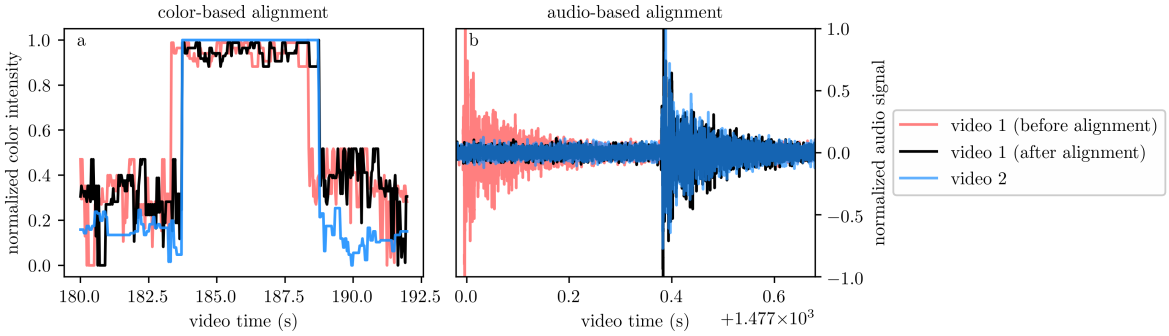

Figure 3.3: (a) Appearance-based and (b) audio-based timing alignment results. The timing of events in (red) video 1 were aligned to match (blue) video 2 to obtain (black) shifted versions of signals in video 1. The horizontal-axis denotes video time corresponding to each signal as labelled in the legend. In (a) the vertical-axis denotes normalized color intensity whereas in (b) the vertical-axis denotes the normalized audio signal. Appearance-based and audio-based signal alignment results agree with each other, and are imperative for successfully applying 4D reconstruction using video images.

After temporally aligning video frames and UTC time derivation, we exported the video frames to high fidelity image files and picked the pixel location of photogrammetry markers. We used the open source multi-media tool FFmpeg to export each video frame to a 4K Portable Network Graphics (PNG) image. The PNG format was chosen because it supports loss-less image compression and thereby retained detailed information in the images. After export, we manually selected pixel locations of the six surveyed photogrammetry targets in each view (Figure 3.1). The corresponding x, y, and z surveyed coordinates aid in recovery of unknown camera parameters and pose, while also providing the means to georeference the reconstructed surface [27]. The aligned video frame images, pixel locations, and surveyed marker locations provided the necessary inputs for photogrammetry algorithms.

We applied a new method which deviated from the standard SfM process since the natural-release failure was a dynamic process. In our application we used two static video cameras that observed a dynamic scene, as opposed to the standard SfM process of observing a static scene with a single moving camera. The modified process enforces recovery of two static camera poses, instead of recovering many moving camera poses. Once the static camera poses are found and fixed, the standard SfM technique is used to estimate the dense 3-D

geometry of a scene at each frame in a video. This modified SfM process was implemented within the photogrammetry software Agisoft PhotoScan 1.4.2 [43]. Within PhotoScan, we provided temporally aligned image pairs and marker locations. A collection of points with associated color were constructed for each frame of the video. These colored point clouds represented a snapshot of the topography of the deforming ground surface at rate of 30 s^{-1}.

The point clouds and videos were processed further to obtain georeferenced rastered elevation maps and orthoimages. Each point cloud was rotated and rasterized into an elevation raster representing the surface geometry of the sediment prism surface at regularly sampled 2 cm by 2 cm cells in x and y. Point cloud elevations were interpolated onto the raster grid using Sibson interpolation. Sibson interpolation was performed using 31 nearest-neighbors and an inverse squared-distance for interpolation weights [58]. This process was repeated for all point clouds. On the same raster grid as the elevation images, we construct orthophotos at each frame of each video; as if the sediment was being observed from directly above (i.e. orthogonal to the $x-y$ plane). The orthophotos enable us to track surface velocities in the $x-y$ plane using optical flow. Orthophotos were constructed by finding a homography between the pixel locations of the photogrammetry markers (see Figure 3.1) and their corresponding (x, y) locations in space [27]. The homography maps points on the plane formed by the camera's image sensor (i.e. pixel coordinates) to the $x-y$ plane (i.e. map view coordinates) which results in an orthophoto as if the videos were taken orthogonal to the $x-y$ plane [27]. The collection of georeferenced rasterized elevation maps and orthophotos, along with associated timestamps, represent the state of the natural-release deforming ground surface in a consistent coordinate system at universally comparable times.

The georeferenced rastered elevation images of the deforming ground surface were used to quantify spatiotemporal velocity variability. We represent vertical and horizontal velocity variations as those present in a particular raster cell. Note that this representation of velocity is not particle velocity. We focused our study on velocity variability at each of the three pore pressure measurement locations at the upslope, midslope, and downslope portions of

the sediment prism surface (Figure 3.1). We first pixel-wise subtracted the rastered elevation in the first frame from the elevation in all raster images to compute vertical displacement as a function of time at each pixel of our rasterized images (Figure 3.4). The time derivative of vertical displacement provides the vertical velocity of the deforming ground surface. However, our elevation observations contain spike-like errors that are amplified by a numerical time derivative operation. We discuss the possible sources of these errors in the Discussion section. To remedy the effects of computing a numerical time derivative on noisy observations, we first smoothed the vertical displacement in time at each pixel of the raster images. We chose to use a Savitzky−Golay filter characterized by a window size of 31 frames (approximately one second) and a 3rd order polynomial fit [59, 60]. We note that sharper videos that result in cleaner elevation observations will allow smaller window sizes. Following smoothing, we approximated the vertical velocity of the deforming ground surface using the scaled second order accurate central difference of the time-smoothed displacements; resulting in a quantification of vertical velocity at each grid cell during failure. Then we computed the median and standard deviation of vertical displacement and velocity within a 0.3 m window around each pore pressure sensor group location (upslope, midslope, and downslope) at each time frame (Figure 3.5a-b).

The downslope velocities at each sensor group location were computed by deploying a dense Farneback optical flow algorithm on adjacent pairs of orthoimages [61]. In general, optical flow algorithms estimate 2D (image row and column) shifts in pixels which optimally warp one frame to another. This algorithm estimates the pixel shifts by comparing localized polynomials fit on each of two successive video frames. During the process, localized polynomials fit the color intensities within multi-scaled overlapping windowed portions of each image. The polynomial coefficients predictably change under a given amount of image translation, or shift. In our orthoimages, the pixel size and frame rate are known, thus the row- and column-wise pixel shifts between frames correspond to those in the x and y direction, respectively. Specifically, for each pixel in a frame, the velocity at that pixel is equivalent

to the pixel shift derived by optical flow scaled by the pixel size and the frame rate of the video. The parameters for the optical flow algorithm included two image pyramid levels, a 51 pixel Gaussian window, three optimization iterations, and a 3rd degree polynomial fit. We computed shifts using gray-scaled versions of orthoimages from each video. In order to make our velocity estimate more robust, we averaged the horizontal velocities recovered from each of the two videos. As with vertical velocity measurements, the variability in the downslope velocities across the sediment prism were illustrated by computing the median and standard deviation at each of the sensor group locations (Figure 3.5c). Summarizing vertical displacement, downslope and vertical velocities allowed us to jointly analyze collocated geometric and pore pressure variations. The process workflow for 3-D surface reconstruction is summarized as:

1. Record videos of natural-release experiment from two static video cameras
2. Align video frames to UTC time using timing light or hammer seismic audio signals
3. Extract video frames as PNG images
4. Apply modified SfM to obtain point clouds for each frame
5. Rasterize point cloud elevations
6. Construct orthovideo frames
7. Compute vertical displacement by subtracting initial elevation at each video frame
8. Compute downslope velocities using optical flow on orthovideos
9. Compute vertical velocities by smoothing and differentiating vertical displacement
10. Summarize vertical displacement and velocities along and across the sediment prism

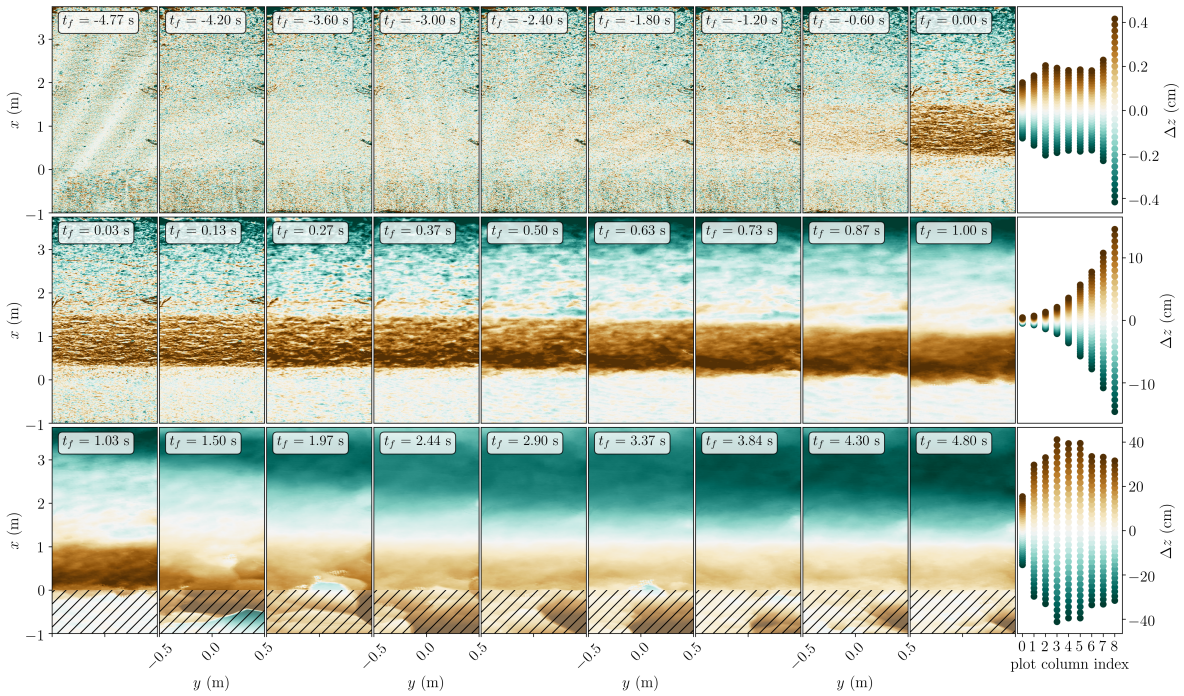

Figure 3.4: A subset of georeferenced vertical displacement maps of the sediment prism surface from its original state over an approximate 10 second interval of the video. Blue colors show downward displacement, white indicates zero displacement, and brown indicates upward displacement. During failure, height change varies over several orders of magnitude, so each panel has a different colorbar; each colorbar is shown in the rightmost column as a function of column index within the plot. The area of upward motion gradually propagated downslope as failure progressed. The effects of uncalibrated lens parameters are apparent in the upper left panel at 0.03 seconds as slanted stripes. The hatched areas in the bottom row denote areas where block-like processing artefacts occur due to image blur.

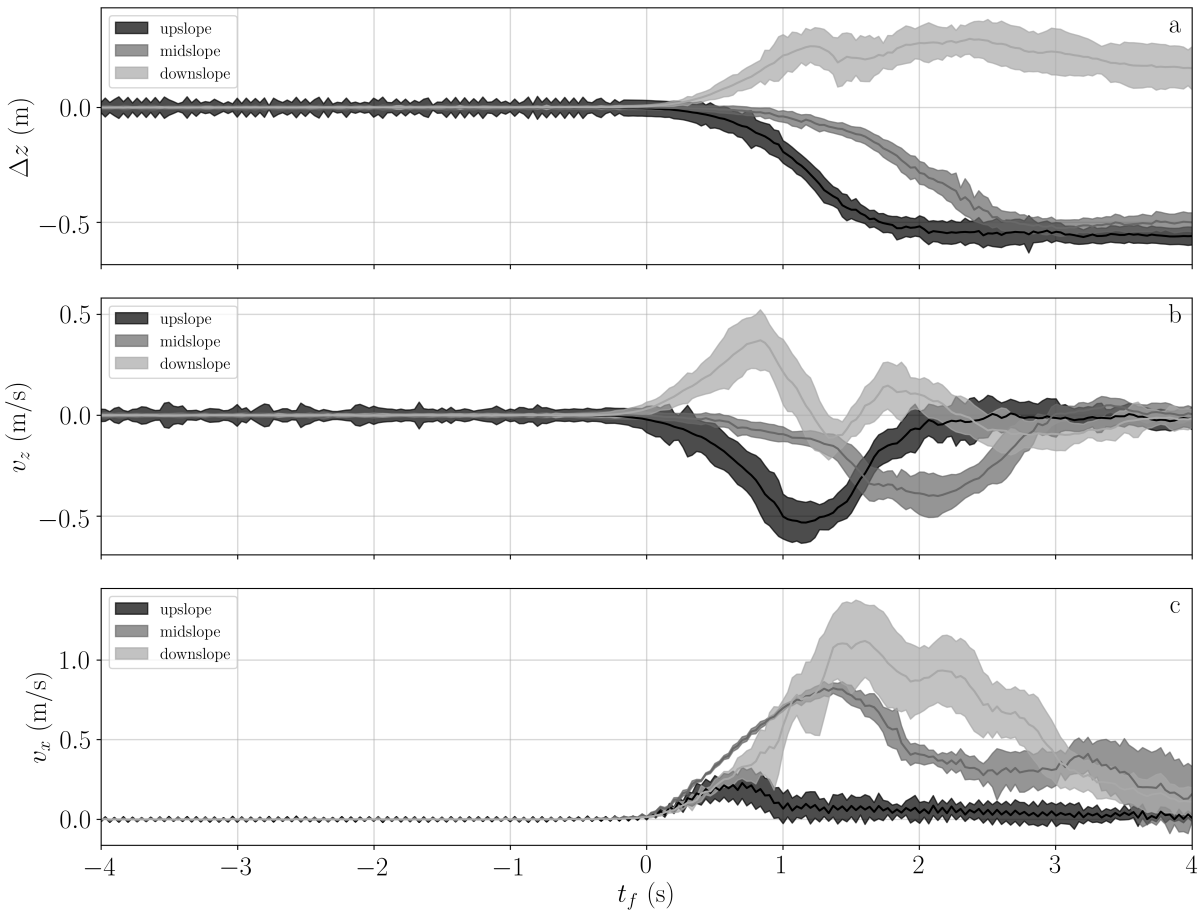

Figure 3.5: Video-based observations of (a) Δz, (b) v_z, and (c) v_x variations near the upslope, midslope, and downslope pore pressure sensors. During failure ($t_f = 0$), the upslope and midslope portion of the sediment prism moved downwards and the downslope portion moved up as sediment flowed downslope.

3.3.3 Reconstructing a transect of the deforming ground surface using lidar

Lidar data were gathered along a narrow transect (see Figure 3.1) of the deforming ground surface and were used to cross-validate the video-based reconstruction [41]. The lidar transect is at most only a few millimeters wide. Lidar data were obtained with a Riegl VZ-400 terrestrial lidar scanner. We used a custom C++ program, Drive VZ-400 [62], to scan along a fixed vertical profile with a vertical field of view of 44°. We limited the horizontal angles of the lidar profile to only 0.13° due to the angular precision and leveling capabilities of the scanner. The lidar scan rate was set to re-scan every 0.017 s or 60 Hz, and the raw scan data were processed to extract the time stamp, x, y, and z coordinates of each laser observation at a desired time range, time interval, and vertical angle resolution using a custom program written in C++ using the RivLib Library [63]. As with the video-based results, we converted the lidar timestamps to t_f by setting $t_f = 0$ at the time when change in z exceeded 5 mm. The data was also georeferenced using the program, which applies the scanner position and orientation information to the lidar dataset. Lastly, individual lidar swaths (the points obtained as the lidar mirror rotates one cycle from the top to the bottom of the sediment prism) were uniquely numbered, which allowed us to isolate point clouds from a single swath. This configuration resulted in point returns that record the deforming ground surface (Figure 3.6a) along a narrow transect (Figure 3.1). The lidar data was post processed by removing points that were not located at the sediment prism surface. In order to quantitatively compare the video results with lidar, we linearly interpolated the lidar data, in both time t_f and space x, to coincide with the video results summarized across the sediment prism (Figure 3.7).

3.3.4 Computing dilation rate from surface displacements and velocities

Here we outline a relationship between basal pore pressure disequillibrium within the sediment prism to the remote measurements of surface displacements and velocities described in section 3.3.2. The relationship can be describe through the dilation rate of the sediment

prism under a depth-averaged debris flow model. It has previously been established that, under the assumptions of a depth-averaged debris flow model, the dilation rate present within a sediment mass can be related to basal pore pressure that is in disequillibrium [16]. This relationship can be represented as

$$D = -\frac{2k}{\mu h}\left[p_b - \rho_f g_z h\right], \tag{3.1}$$

where D is the dilation rate, k is the hydraulic permeability within the sediment mass, μ is the shear viscosity of the sediment mass, p_b is the basal pore pressure, ρ_f is the fluid mass density, and h is the sediment thickness normal to the slope. In addition to this relationship, we can express the depth-averaged mass conservation of the sediment as

$$\frac{\partial h}{\partial t} + \frac{\partial\left(h\bar{u}\right)}{\partial x'} + \frac{\partial\left(h\bar{v}\right)}{\partial y'} = D, \tag{3.2}$$

where $\frac{\partial}{\partial t}$ denotes a partial time derivative, $\frac{\partial}{\partial x'}$ denotes a partial spatial derivative down-dip, $\frac{\partial}{\partial y'}$ denotes a partial spatial derivative along-strike, $\bar{u}$ denotes depth-averaged velocity down-dip, and $\bar{v}$ denotes depth-averaged velocity along-strike [16]. In order to test our hypothesis, we test whether dilation rates derived from measurements of surface displacements and velocities, as defined in equation 3.2, lie within expected ranges of the dilation rates computed using in situ basal pore pressure data, as defined in equation 3.1.

In order to use equations 3.1 and 3.2 to estimate the dilation rate, the displacements and velocities measured in section 3.3.2 must be represented in the down-dip and slope-normal direction (instead of in the direction of the x and z axes). We convert the vertical displacement $\Delta z(x,t)$ to the change in sediment thickness normal to the slope, denoted $\Delta h(x,t)$, using

$$\Delta h(x,t) = \Delta z(x,t)\cos(\theta), \tag{3.3}$$

where $\theta = 31^\circ$ denotes the slope angle (see 3.1). The sediment thickness normal to the slope, denoted by $h(x,t)$, is computed by adding the change in thickness to the initial thickness of

the sediment prism

$$h(x,t) = h_0 + \Delta h(x,t), \tag{3.4}$$

where we use $h_0 = 0.65$ m as the initial sediment prism thickness (see 3.1). Similarly, we project the surface velocities v_x and v_z (computed in section 3.3.2) onto the down-dip direction, denoted by x', to compute the down-dip surface velocity, denoted by u, using

$$u(x,t) = v_x(x,t)\cos(\theta) - v_z(x,t)\sin(\theta). \tag{3.5}$$

The surface velocity u is used to infer the down-dip depth-averaged velocity $\bar{u}$ by assuming a velocity-versus depth relationship $f(z/h)$ where

$$u = f(z/h)\bar{u}. \tag{3.6}$$

We use a velocity-versus depth-relationship established by Johnson et al. [64] during previous experiments at the flume. This relationship is given by

$$f(z/h) = \alpha + 2(1-\alpha)(z/h). \tag{3.7}$$

We choose to use $\alpha = 0.5$ which assumes the sediment undergoes shearing and basal slips as the sediment is moving [64]. Our measurements of velocity occur at the surface where $z = h$, so our velocity-depth relationship becomes $f(h/h) = f(1) = \frac{3}{2}$. Using equation 3.6, we now establish our relationship between our surface and depth averaged velocities as

$$\bar{u}(x,t) = \frac{2}{3}u(x,t). \tag{3.8}$$

Next we expand the terms in the left-hand-side terms of equation 3.2 to derive at an expression that only relies on the displacements and surface velocities estimated in section 3.3.2. To simplify our derivation, we assume that the along-strike depth-averaged velocity $\bar{v}$ is negligible and therefore set $\frac{\partial(h\bar{v})}{\partial y'} = 0$. The remaining partial derivative terms in equation 3.2 require us to prepare the variables $h(x,t)$ and $\bar{u}(x,t)$ for numerical derivatives. Note that these variables are a function of (x,t), but we require derivatives in the x' direction in equation 3.2. In preparation for applying the chain rule to equation 3.2, we compute the

change along the x' direction given a change in the x direction as

$$x(x') = \frac{x'}{\cos(\theta)} \rightarrow \frac{\partial x}{\partial x'} = \frac{1}{\cos(\theta)}. \tag{3.9}$$

Lastly, we expand equation 3.2 by applying the product rule to find that

$$\begin{aligned} D(x,t) &= \frac{\partial h(x,t)}{\partial t} + \frac{\partial \left(h(x,t)\bar{u}(x,t)\right)}{\partial x'} \\ &= \frac{\partial h(x,t)}{\partial t} + \frac{\partial x}{\partial x'}\frac{\partial}{\partial x}h(x,t)\bar{u}(x,t) \\ &= \frac{\partial h(x,t)}{\partial t} + \frac{\partial x}{\partial x'}\left[h(x,t)\frac{\partial}{\partial x}\bar{u}(x,t) + \bar{u}(x,t)\frac{\partial}{\partial x}h(x,t)\right], \end{aligned} \tag{3.10}$$

where the terms $\frac{\partial}{\partial t}h(x,t)$, $\frac{\partial}{\partial x}\bar{u}(x,t)$, and $\frac{\partial}{\partial x}h(x,t)$ in equation 3.10 are readily computed using second order accurate central finite differences. Equations 3.1 and 3.10 both describe dilation rate, but the former requires observations of basal pore pressure and the later can be found using surface displacement and velocity observations.

We test our hypothesis by observing if the dilation rate computed using equation 3.10 is similar to the dilation rate computed using equation 3.1. When evaluating equation 3.1, we use $\mu = 0.001$ Pa·s as the pore fluid viscosity of pure water and $g_z = 9.81\cos(\theta)\ \frac{m}{s}$. Values for p_b are measured by the pore pressure sensors in the sediment prism (see 3.1). We use the pore pressured measured in the deepest sensors to approximate the basal pore pressure. The hydraulic permeability k can vary over several orders of magnitude, so we present results using values $k_{min} = 1 \times 10^{-11}$ and $k_{max} = 1 \times 10^{-7}\ m^2$.

3.4 Results

We obtained spatially and temporally dense and georeferenced representations of the deforming ground surface during slope failure. The signal-based timing alignment approach, using the timing light, resulted in a shift of 12 frames, or 0.4 seconds, from one video to the other. We confirmed the frame shift by applying it to the timing light pixel color intensity curves and visually inspecting alignment (3.3a). The audio-based timing alignment approach, using the audio signals embedded in each video, resulted in an optimal shift of 0.3865 seconds

or 11.58 frames. The appearance-based and audio-based timing results agreed within a single frame. Thus, we confidently shift by 12 frames to temporally align the videos to each other before proceeding with the modified SfM process.

We tracked surface displacement during landslide failure using elevations interpolated from the SfM point clouds (3.4). Generally, we observe downward displacement at upslope portions of the sediment prism and upward displacement in the lower portion, as the sediment moves over the retaining wall (3.4). Displacement is relatively constant in the cross-slope direction of the sediment prism (3.4). The concurrent video-based and lidar-based elevation transects (3.6) show close correspondence in both space and time (3.7). Note that the video-based results along the lidar transect are taken as the median z value across the y dimension. The difference in z between lidar and video results, denoted as ϵ_z=(lidar−video), changes dramatically after failure at $t_f = 0$ (3.8). Before failure ($t_f < 0$), ϵ_z has a mean $\mu = -0.47$ cm, a median $\tilde{\mu} = -0.54$ cm, and a standard deviation $\sigma = 1.42$ cm. After failure ($t_f > 0$), $\mu = 1.58$ cm, $\tilde{\mu} = 3.03$ cm, and $\sigma = 10.03$ cm. The evolution of the sediment prism surface along the lidar transect (3.6) matches the appearance of the failure event in the experiment video [57].

The elevation and velocity across the sediment prism changes with time and downslope distance (3.5 and 3.9). The local vertical displacement that occurred over the entire failure process was less than 0.6 meters. At the beginning of failure, upslope sediment moved downwards, midslope sediment remained at a constant elevation, and downslope sediment moved upwards (3.5), indicating rotation occurred during failure onset. The displacement across the sediment prism was < 1 cm before failure and reached as much as 50 cm after failure (3.5), indicating that the variability in displacement across the sediment prism increased after the onset of failure. At the onset of failure, the vertical velocities were negative (downward) for the upslope and midslope portions of the sediment prism and positive (upward) for the lower portion (3.5-3.9). The downslope velocities show apparent rapid oscillation several seconds before failure and positive (downslope) velocities as failure occurred; the lower and middle

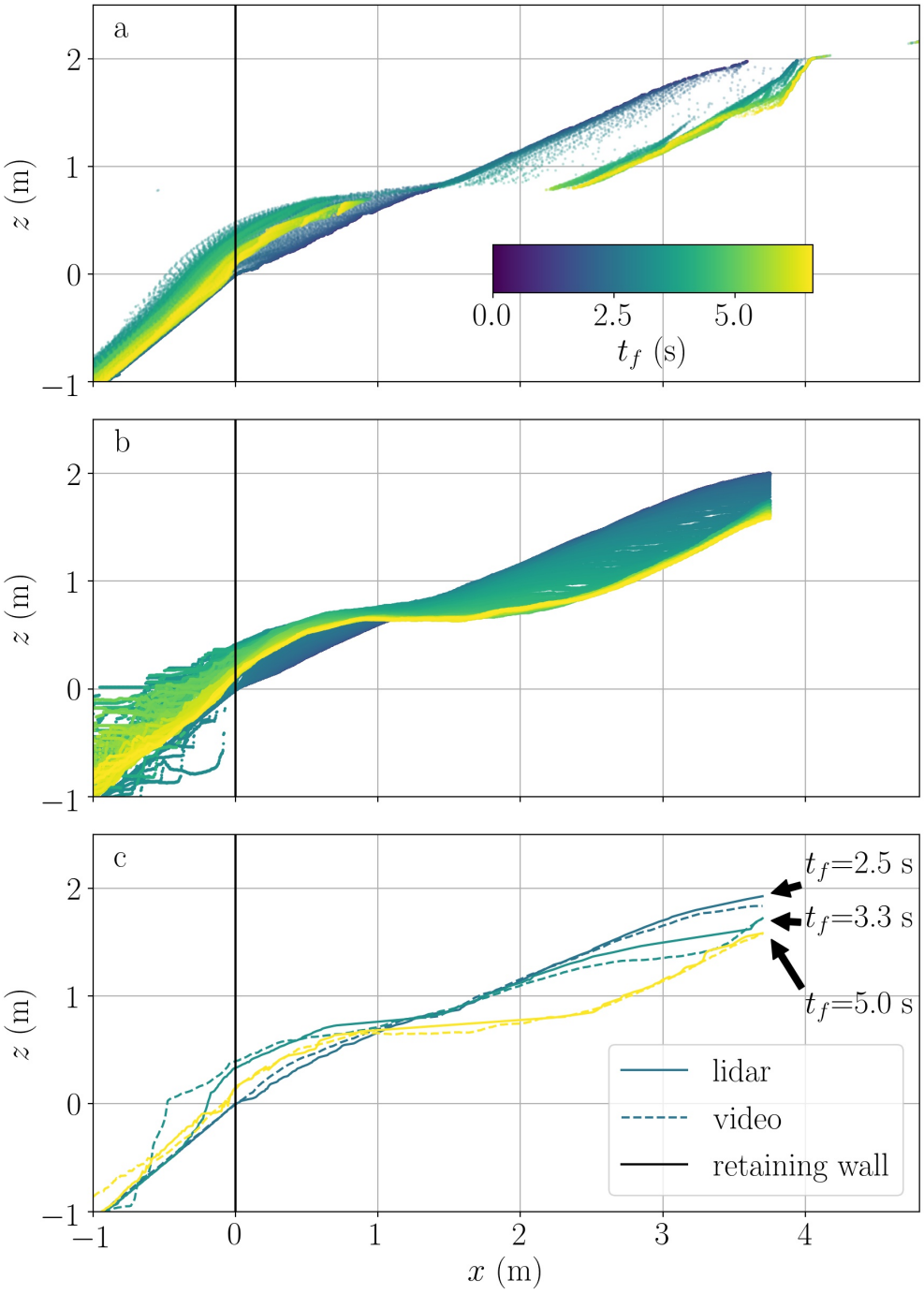

Figure 3.6: Deforming ground surface observations during natural-release failure measured along the lidar transect. The point color brightness increases with time in t_f (yellow points occur at greater times t_f). (a) Lidar and (b) video-based results show similar results. (c) Lidar and video-based results at a subset of times t_f. Lidar and video-based results are more similar before failure than after. The absence of dense lidar points in the upper portions of the sediment prism ($x > 1.5$) is caused by moving sediment blocking the lidar laser.

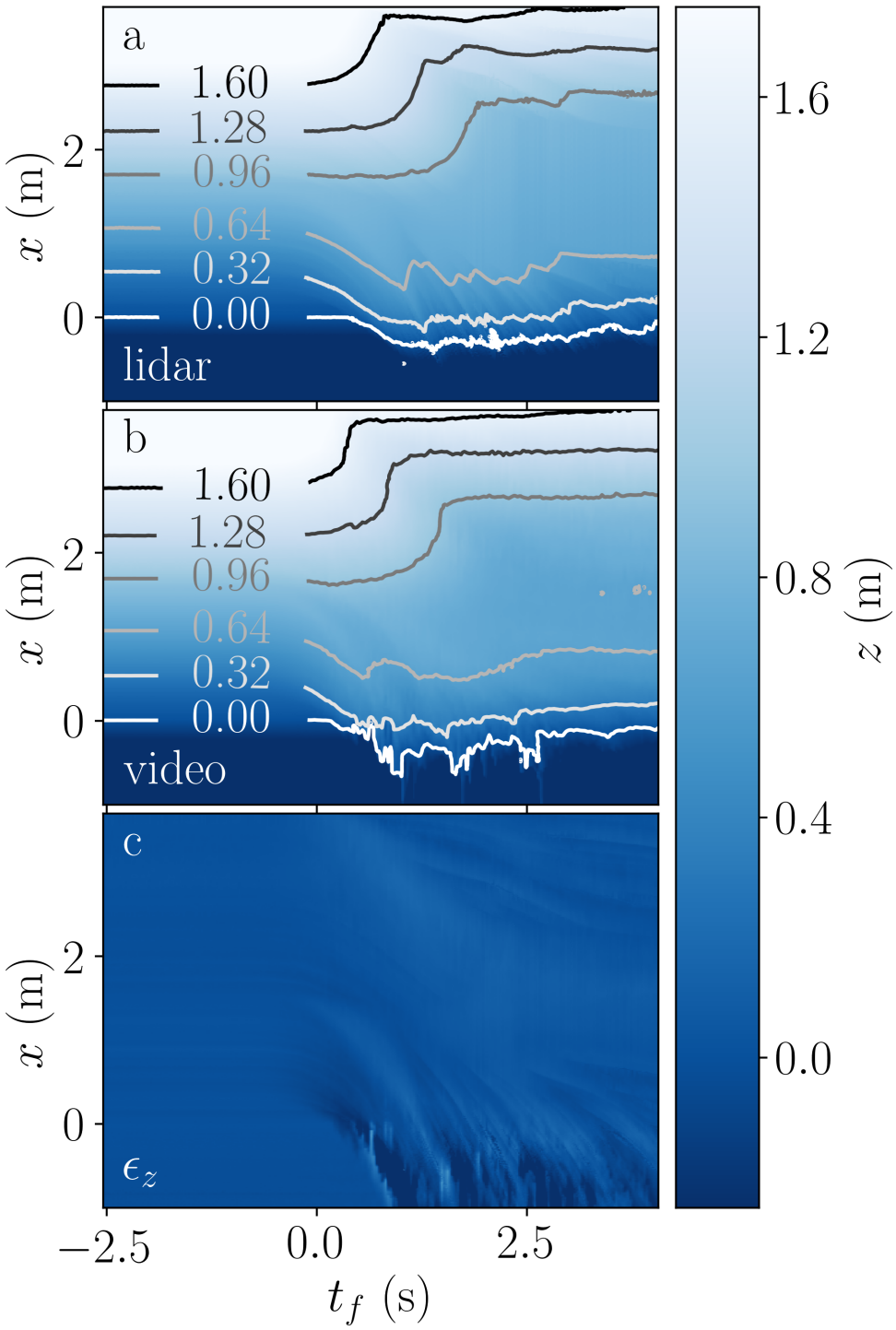

Figure 3.7: Observations of surface elevation z along the lidar transect derived from (a) lidar and (b) video as a function of time and space. The (c) difference between lidar and video is small.

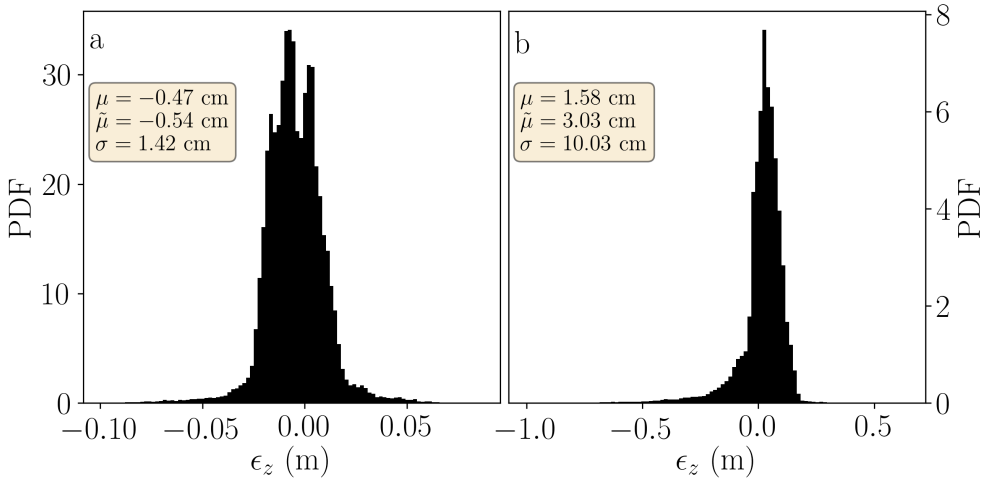

Figure 3.8: Empirical probability density function (PDF) of the difference ϵ_z between lidar and video results along the lidar transect (a) before, and (b) after failure at $t_f = 0$. Note that horizontal and vertical axis in (a) and (b) are at different scales. The difference is characteristically smaller before failure than after. After failure, image blur and the sediment blocking the lidar laser cause larger differences between results.

portion of the sediment prism surface moved fastest. The rapid oscillations in downslope velocity are an artefact due to video compression and imperfect camera calibration, which we discuss below. Negative downslope velocities indicate upslope motion, which is unrealistic. We observe fluctuations in pore pressure in the upslope portion of the sediment prism a few seconds before the surface moves a measurable amount (3.9).

Dilation rate computed using pore pressure data (see equation 3.1) indicates that upslope sediment rapidly dilated then contracted at failure (see 3.10). An alternative representation of the dilation rate computed using video data alone (see equation 3.10) shows that just after $t_f = 0$ a compact area of contraction initiated upslope while a broader area of dilation developed downslope (3.11). The narrow band of contraction moved downslope at a rate of approximately 0.5 m/s (see 3.11). The video-based dilation rate at the upslope sensor location (3.10a) does not show the rapid increase in dilation rate indicated when using pore pressure data to compute dilation rate (3.10b). However, the dilation rates computed using both equations 3.1 and 3.10 agree that downslope dilation and subsequent contraction

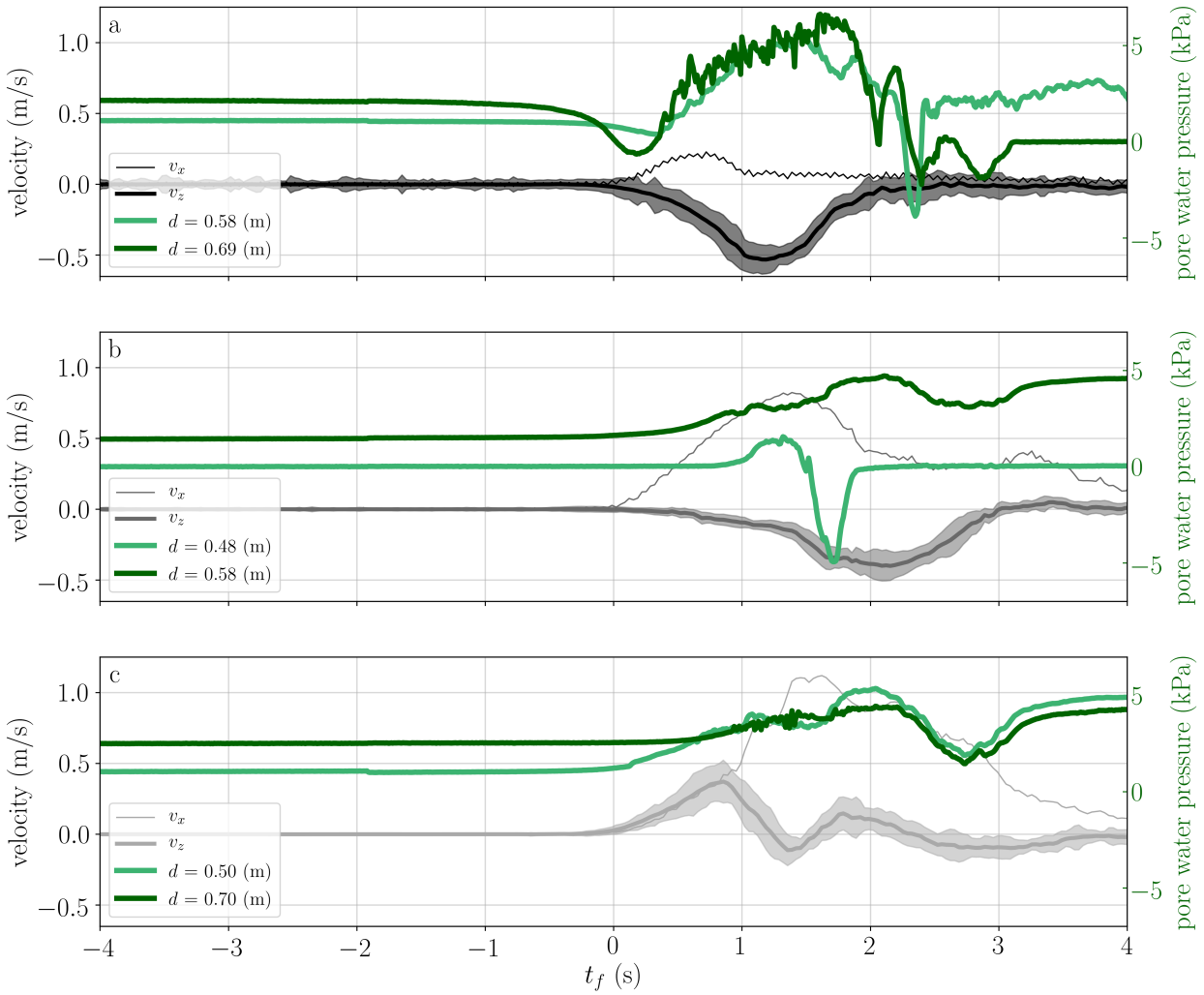

Figure 3.9: Pore pressure and velocity variation near failure for the (a) upslope, (b) midslope, and (c) downslope sensor locations. Two pore pressure sensors were placed at each location upslope, midslope, and downslope; the depths d of each sensor are noted in the legend. Pore pressure suddenly decreased in the upslope portion of the sediment prism before failure initiated. After failure, sediment rapidly moves downslope indicated by the velocity curves.

occurred just after failure (3.11).

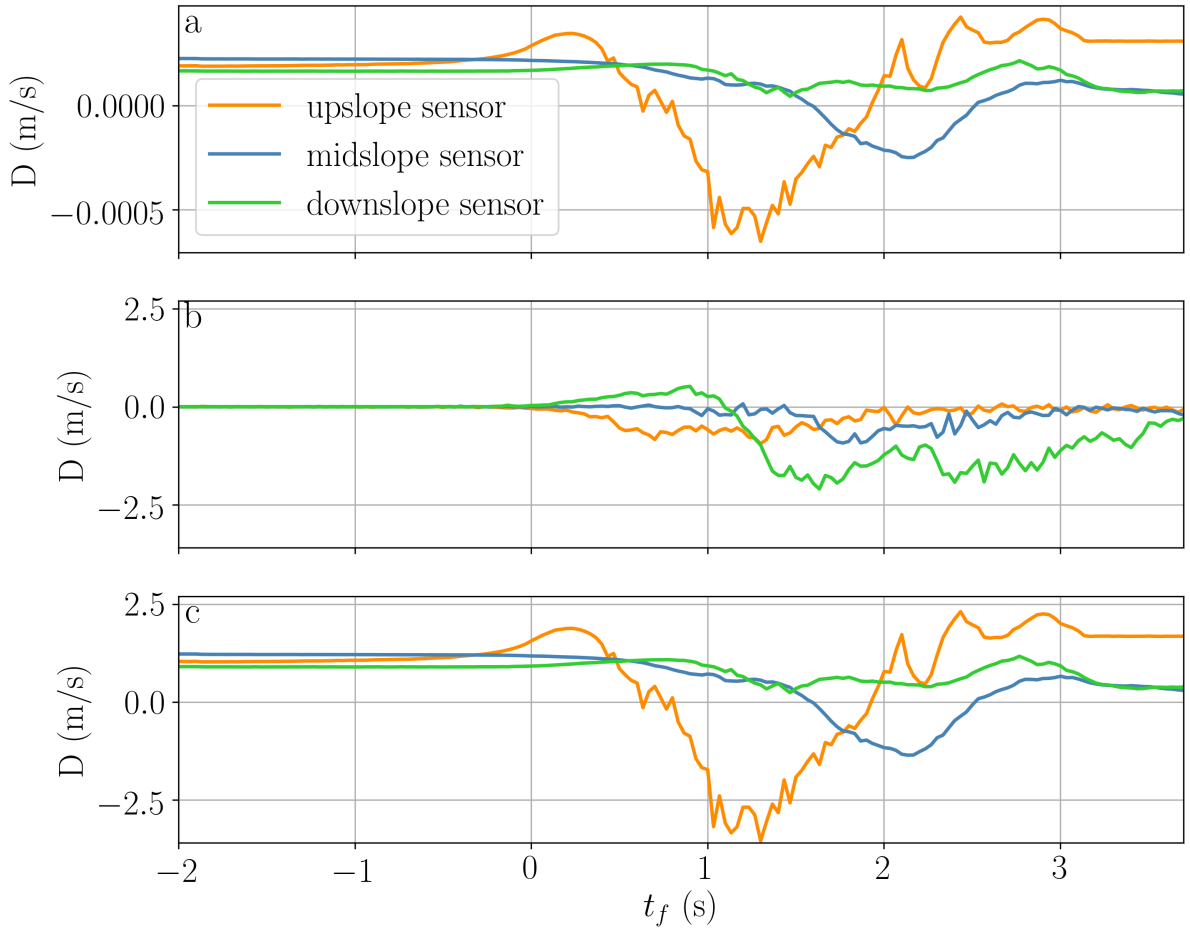

Figure 3.10: Soil dilation rate computed using (a) equation 3.1 and $k_{min} = 1 \times 10^{-11}$ m^2, (b) using equation 3.10, and (c) using equation 3.1 and $k_{max} = 1 \times 10^{-7}$ m^2. Results from equation 3.1 (a & c) should only be trusted for $t_f < 2$ s since the pore pressure sensors were being pulled by cables beyond this time. These curves confirm our hypothesis that (b) video-based estimates of dilation rate are within reasonable ranges of (a & c) estimates that depend on in situ measurements of pore pressure.

3.5 Discussion

3.5.1 Error Analysis

Temporal and spatial errors are present, hence we cross-validate video-based results with those from lidar. We consider error as an incorrect observation of reality. The temporal

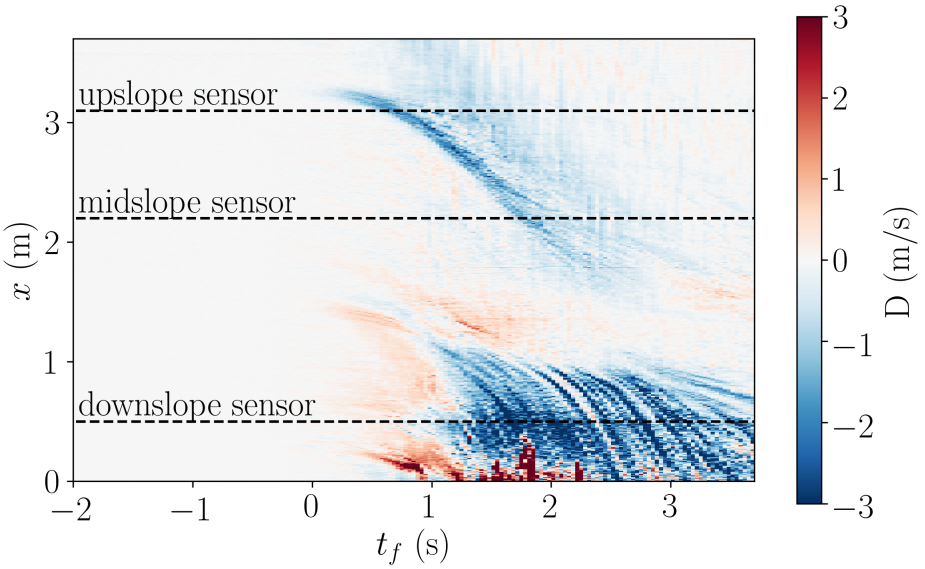

Figure 3.11: Soil dilation rate along the x-axis of the sediment prism as computed using video observations and equation 3.10. Red colors indicate positions and times which exhibit dilation and blue colors indicate contraction. The location of pore pressure sensors are noted by the dashed lines. When the sediment fails ($t_f = 0$) a narrow band of contraction initiates upslope then propagates downslope. The sediment dilated and contracted during and after failure; the sediment did not strictly behave as an incompressible fluid.

error in our results exist due to imprecise video alignment and video compression artefacts. We aligned each video using the pixel color intensity of a timing light and using audio signals of a hammer seismic strike (3.3). The temporal alignment precision when using the timing light is limited by the frame rate of the camera, 29.97 fps, whereas the alignment precision when using the audio signal is limited by the audio sampling frequency, 48 kHz. The latter is far more precise and, when rounded to the nearest frame, agrees with the timing alignment derived from the timing light pixel color intensity. We note that the distance between the hammer and microphone is at most 5 meters (the full length of the sediment prism), which corresponds to the hammer strike sound wave traveling to the microphone in $5\ m \div 343\ \frac{m}{s} = 0.0146\ s$. However, the amount of time between video frames is only $1 \div 29.97\ \text{fps} = 0.03\ s$, so the maximum error in the time shift derived from the hammer strike audio signal is less than the time between frames. In addition, we assumed that the frames exactly overlapped in time, which is only true up to the temporal resolution of the camera frame rate of 29.97 fps. Any physical change within the scene that is more rapid than the frame rate results in blurred images. In addition, changes that occur more rapidly than the Nyquist frequency of our video camera, which is half the sampling rate, result in temporally aliased observations according the the Shannon-Nyquist sampling theorem [65–67]. Aliased observations erroneously contain low frequency changes that are caused by high frequency changes beyond the Nyquist frequency; high frequency signals beyond Nyquist are aliased as lower frequency observations. Thus, image blurring and temporal aliasing cause erroneous, possibly periodic, image features that SfM will incorrectly use to reconstruct the deforming ground surface. Lastly, the videos were recorded and stored as compressed MP4 files. MP4 compression is often performed on blocks in a video and identifies redundancies between and within video frames to reduce storage space. The block-based processing used in MP4 compression involves processing videos in the Fourier domain and can introduce artificial, localized, and coherent ringing artefacts between video frames due to the Wilbraham-Gibbs Phenomenon [68, 69]. Removing these artefacts from compressed

videos is an active area of research (e.g., [70]). These subtle coherent shifts will also be misinterpreted as surface motion during an optical flow or SfM process, which partially explains the oscillations in the downslope velocities during $t_f < 0$ (3.5). These oscillations could also be caused by a combination of lens distortion effects, a vibrating camera, image blurring, and temporal aliasing. The oscillation effects are more relatively significant earlier in time because, although minor, they are comparable to the amplitude of the total elevation during times $t_f < 0$ s. They become less significant as motion increases after failure.

The spatial, or geometrical, error in the video-based observations is due to many interconnected error sources influencing the SfM process. Image noise, unknown camera or marker positions, and unknown camera parameters are primary sources of error. Without prior knowledge and additional measurements, we are unable to directly estimate the error in derived camera parameters, such as position and focal length. However, we measured the position of photogrammetric markers in the experiments and can therefore quantify their positional error. The photogrammetric marker positioning error is computed after the SfM process by comparing the true marker position with the estimated marker position in the derived point clouds. The maximum root-mean-squared (RMS) error in the position of each marker was less than 1 cm for all markers. The error due to lens distortion manifests as ripples that laterally span across the sediment prism in the expression of the deforming ground surface [71]. These ripples are especially apparent in upslope portions of the sediment prism at $t_f = -4.77$ s (3.4). These ripples falsely suggest the presence of small scale slope and curvature deviations on the deforming ground surface; the persistent ripple-like features could be misinterpreted during a curvature or slope analysis of the deforming ground surface. These negative effects may be directly remedied by deriving lens distortion parameters prior to the experiment via common camera calibration techniques. We have identified and quantified estimated error in marker position and timing, however other error sources such as lens distortion are difficult to quantify.

We improve our understanding of the error present in video-based results by validating them with alternative independent observations from a lidar sensor (3.6 - 3.8). The observations from lidar are more spatially dense, and presumably accurate, than video as we move downslope. The accuracy disparity downslope is caused by rapidly moving sediment which resulted in blurry video images. However, along the sediment prism surface the observations from video are more spatially dense than lidar observations; the video is not limited to the narrow transect viewed by the lidar. The accuracy disparity in the surface is due to the viewing angle difference between the lidar and video cameras. From the lidar system's point of view, portions of the sediment prism surface are occluded due to sediment cascading over the retaining wall during failure; the video cameras were mounted more directly above the sediment prism and did not suffer from occlusion. Dynamic point clouds derived from videos and lidar along the transect show agreement in deforming ground surface geometry (3.6). The cross-sectional area derived from lidar and video are similar despite being independently derived. A quantitative view of this similarity as a function of distance x and time t_f (3.7) indicates that the difference ϵ_z is on the order of centimeters. The distribution of ϵ_z before and after failure at $t_f = 0$ (3.8) shows that video and lidar agree more before failure than after. Considering the median and standard deviation of ϵ_z before failure, the video and lidar agree within -0.54 $\pm$ 1.42 cm, and after within 3.03 $\pm$ 10.03 cm. Larger disagreement between lidar and video after failure is caused by image blur and the sediment blocking the lidar laser. The validation of video-based deforming ground surface geometry with lidar provides confidence in the distributed geometry of the deforming ground surface observed via video.

3.5.2 Mechanical Interpretation of Deformation during Slope Failure

Our measurements of the ground surface velocity during slope failure were accompanied by contemporaneous measurements of evolving pore-water pressure made with six electronic sensors buried at the depths and locations shown in 3.1 (Iverson et al. [53] described the pore-pressure sensor properties.) The sensors initially traveled downslope with the moving

sediment, but they were tethered by cables that caused them to pull free from the sediment after a few meters of downslope displacement. The pore-pressure data consequently have clear physical meaning for only about 2 s after failure commenced at $t_f = 0$. Nevertheless, taken in conjunction with the measured ground surface velocities, the pore-pressure data facilitate mechanical interpretation of deformation that accompanied slope failure. The interpretation is informed by the results of prior experimental and theoretical studies that illustrate clear relationships between pore pressure changes and dilation or contraction of sediment that can occur as slope failure proceeds [52, 53, 56].

Pore pressures measured at all locations slowly increased as we added water to the sediment, but during the several seconds prior to slope failure at $t_f = 0$, they were essentially constant and had values > 0 and < 2.5 kPa (3.9). Then, roughly 1 s before the onset of slope failure, the pore pressure began to decline noticeably at a depth of 0.69 m in the upslope sensor nest (3.9a). This decline indicated that localized dilative deformation had begun to occur - likely related to opening of a macroscopic subsurface crack associated with an incipient headscarp that developed in the vicinity [57]. A smaller decline in pore pressure also occurred at a depth of 0.58 m in this location, and this evidence of localized dilation persisted for roughly 0.5 s. We confirm pore pressure indications of upslope dilation using the upslope dilation rates computed using equation 3.1 shown in 3.10b. Thereafter, the onset of slope failure became conspicuous and pore pressures began to increase at all locations where measurements were made (3.9).

Dramatic pore-pressure increases, indicative of contractive deformation, occurred at most locations as downslope sediment movement attained speeds > 0.1 m/s (3.9). This behavior mirrors that observed in prior landslide experiments using loosely packed sediment [52, 53, 72, 73], and it documents the development of a nearly liquefied state. A highly fluid style of downslope motion, characteristic of liquefied sediment, is also evident in video recordings of the experiment [57].

The temporal alignment of the pore-pressure changes and surface velocity changes measured in our experiment generally shows that a liquefied (or nearly liquefied) state persisted as the sediment evacuated the source area (3.9). This behavior is consistent with a well-known style of debris-flow mobilization from landslides [52]. However, no previous studies of such mobilization have provided the detailed resolution of accompanying surface deformation that we provide here. Our new detailed observations of surface deformation enable us to further study how the sediment contracted and dilated during failure.

The dilation rates we compute indicate that the sediment did not behave strictly as an incompressible fluid since it dilated and contracted following failure. This observation is supported by dilation rates computed with and without in situ pore pressure measurements (3.10). There are distinct differences between the dilation rates we present with and without in situ pore pressure measurements. One difference is that the dilation rates computed using pore pressure data (equation 3.1) are positive for t_f <0 whereas those computed using video (equation 3.10) are zero. Another difference occurs during the onset of failure (t_f=0) at the upslope sensor location; dilation is indicated when computed using equation 3.1 is not when we use video to compute dilation rate (equation 3.10). We believe both of these differences are due to there only being slight changes in surface elevation and velocity before and at t_f=0; the video cameras simply aren't sensitive enough to see the subtle difference and thus terms in equation 3.10 are very small. Nevertheless, the amplitude and shapes of dilation rates with and without pore pressure date (3.10) are similar which does not disprove our hypothesis.

3.5.3 Future Directions

Acquisition changes in future experiments could reduce the errors and uncertainties we observed in this study and provide a more accurate reconstruction of the deforming ground surface. Camera position, orientation, focal length, and lens distortion parameters could be measured prior to the experiment using standard camera calibration technique. Improving video frame rate and shutter speed could reduce the negative effects of image blur and

temporal aliasing during rapid failure. In addition, the spatial and temporal resolution of our results may improve as we use higher resolution and higher frame rate cameras. Additional static cameras at more diverse viewing angles would improve our results, as would additional photogrammetry markers. Gathering high speed videos in a raw uncompressed format would remedy the compression artefacts that influenced results. Despite the room for improvements, the validation of results in this work show that even a modest multi-view video camera setup enables novel ways of quantifying spatially dense landslide evolution observations.

In large-scale natural settings we recommend gathering more than two videos, from a variety of viewing angles, with calibrated cameras at known locations and orientations. For syncing the videos, we recommend using either GPS clocks, natural sound, or perhaps solar powered timing lights visible in each video. In addition, establishing visible markers (with the capacity to broadcast their location via GPS) in the field would aid the displacement and velocity recovery using the methods we present.

3.6 Conclusion

Rapid and dense observations of surface displacement and velocity are obtained using two unsychronized video cameras. Our video-based observations align with lidar-based observations and provide information at spatial and temporal resolutions useful for studying detailed rapid landslide failure. We use these new detailed observations to infer soil dilation rate that would otherwise require in situ measurements of basal pore pressure and estimates of hydraulic permeability, fluid shear viscosity, and density. Our results show that the failing sediment did not behave as an incompressible fluid. Based on our methods and results, it is feasible to retroactively process existing unsychronized multi-view footage of landslides to quantify behavior before and during failure. Moreover, the video-based observations of landslide movement are a low-cost method that can be used broadly in areas where detailed temporal and spatial measures of mass movement are required.

3.7 Acknowledgments

This work was supported by the U.S. Geological Survey Landslide Hazards Program. The use of trade, product or firm names in this paper is for descriptive purposes only and does not constitute endorsement by the U.S. Geological Survey. Raw video frames, lidar data, and derived height change maps will be made available via ScienceBase.

CHAPTER 4

A TECHNIQUE FOR MEASURING THE VELOCITY FIELD OF A DEBRIS FLOW USING A SINGLE VIDEO

Ready to submit

Thomas D. Rapstine[1,2], Kate E. Allstadt[2], Francis K. Rengers[2], Richard M. Iverson[2], Joel B. Smith[2], Maciej K. Obryk[2], Matt Logan[2], Michael J. Olsen[3]

4.1 Abstract

Debris-flows are dangerous natural occurrences that impact infrastructure and exhibit complex granular flow properties. The velocity of a debris-flow is a key parameter of interest for understanding the physics of granular flow and furthering knowledge of how debris-flows move. Here, we propose a method for quantifying the velocity field of a debris-flow at the U.S. Geological Survey debris-flow flume using a single video. The debris-flow front was previously tracked at the flume by picking the front location in each frame of a video or by denoting the time the flow front passed each of only a few sparse sensors along the flume. Instead, we measure velocity by analyzing edges and structure tensors in a warped image taken as a slice long the direction of flow in a video. Our method deviates from previous methods in that we estimate the surface velocity of the debris and the velocity of the debris-flow front at temporal resolutions of 29.97 Hz and spatial resolutions on the order of 10's of cm with an inexpensive camera. Additionally, our method provides measurements using only minor human intervention and can be retroactively applied to past videos at the flume to provide a more complete dataset of debris-flow surface velocity fields. The images that are a result of our proposed method resemble seismic shot gathers, so we refer to them as

[1]Primary researcher and author.
[2]Department of Geophysics, Colorado School of Mines, Golden, Colorado, United States of America.
[2]United States Geological Survey
[3]Oregon State University

flow gathers (since they visualize flow dynamics). Flow gathers represent the appearance of a debris-flow surface as a function of time and space and can be used to interpret and quantify various flow characteristics. Our method recovers debris-flow front positions that agree with independent measurements from lidar within tenths of a second and can be used to quickly identify and quantify the motion of roll waves.

4.2 Introduction

Debris-flows are deadly and costly natural hazards that exhibit complex granular flow physics. The velocity of a debris-flow directly relates to the momentum of material within it and to how the flow deposits sediments as it moves [54, 64]. Thus, the velocity of a debris flow plays a key role in designing structures for debris-flow mitigation [74]. In addition, debris-flow velocity is used in empirical relationships used to formulate models for describing debris-flow motion [75]. A key problem is therefore how to measure the surface velocity of a debris-flow and the velocity of the debris-flow front as a function of time and space. Many large scale experiments aimed at better understanding debris-flows have been conducted at the U.S. Geological Survey debris-flow flume in Blue River, Oregon, USA (hereafter referred to as the flume) and have led to data that are useful for formulating and testing debris-flow models that include debris-flow surface and front velocity [15, 16, 54]. In the past, the debris-flow front position and velocity was measured at four discrete locations along the flume using laser-based flow-depth sensors or by manually tracking the flow front in each frame of a video and comparing to reference markers at 5 m intervals along the flume axis [54].

Recent advancements in repeat lidar technology allow for non-contact measurements of the debris flow surface at high sample rates, which can be used to measure debris-flow front velocity. In recent years, repeat lidar surveys have been used to quantify changes in topography at increasingly higher frequencies. In field settings, lidar repetition rates have increased from years [4, 6] to months [3, 5, 76] down to hours [7, 8]. Recently, sub-second lidar repetition rates have been achieved at the flume that provide accurate estimates of the flow front position [41, 77]. While lidar has proven to show accurate and useful estimates of

debris-flow velocities, it is still a relatively expensive acquisition system when compared to video camera technology.

Here we propose a method that also achieves sub-second measurements of flow front position, and velocity, that relies on a single video camera. Our method accommodates unique challenges posed when processing videos of debris-flows at the flume. Namely, we develop an automated method that allows us to track details of flow dynamics from videos recorded from a large distance with strong perspective effects influencing the appearance of the debris-flow in a video. In addition, our method does not require particle tracers to be placed within the debris-flow as many particle imaging velocimetry (PIV) methods often do [44–46]. We describe our method then apply it to two videos recorded at the flume in May 2017. In order to validate our results, we compare the flow front position and velocity derived using video with that derived using lidar.

4.3 Methods

4.3.1 Experimental Setup

The experimental data we use to demonstrate how to measure debris-flow surface and front velocity was recorded on May 23rd and 25th, 2017 at the flume [52, 53, 57]. The flume is a 95 m long, 2 m wide rectangular chute which tilts at a 31° angle from horizontal most of its length [54]. Results in this paper are presented as a function of distance down-flume from a gate located 12.5 m from the top of the flume that opens to initiate a debris-flow experiment at time $t = 0$ s [54]. We denote distance down-flume as d where $d = 0$ m is located at the gate and increases down-flume. At $d = 74$ m down-flume, the tilt of the flume becomes more shallow following a catenary curve and drops 2.2 m down to a slope of 4° at base of the flume at 82.5 m [54].

The experiment on May 23, 2017 included a 8 m^3 mixture of sand, gravel, and large rocks; the May 25th, 2017 experiment included a larger 10 m^3 mixture of sand, gravel, and large rocks [78]. Flow-depth normal to the flume bed were measured by laser depth-sensors at $d = 2.5, 31.7, 65.4$, and 80.0 m. We exclude the laser-based flow-depth measurement at

$d = 2.5$ m from our analysis since at that location our the lidar data appeared blocked by the gate that released the debris-flow. During each experiment a Canon HFM500 video camera located at approximately $d = 115$ m down-flume recorded the debris-flows at 29.97 frames per second (fps) and a resolution of 1920×1080 pixels (Figure 4.1). A summary video recording of the May 23rd debris flow can be found online at `https://pubs.usgs.gov/of/2007/1315/videos/2017/2017_05_23.mp4` and the May 25th video recording can be found at `https://pubs.usgs.gov/of/2007/1315/videos/2017/2017_05_25.mp4`. Timing lights turned on to indicate when the gate was opened at $t = 0$ s. We identify $t = 0$ s in each video by denoting the frame when the timing lights turned on. We use these videos to measure debris-flow surface and front velocity.

In addition to video footage, lidar data were gathered during the experiment on May 25th, 2017 [79]. The lidar data were gathered using a non-standard application of a Riegl VZ-400 terrestrial lidar scanner. This scanner is designed to rotate 360° horizontally with vertical field of view of 100° in order to obtain a 3D point cloud focused about the center of the lidar unit. However, we used a custom C++ program, Drive VZ-400 [62] to focus the lidar unit along a narrow profile (approximately 1 mm in width), from the top to the bottom of the flume. Rather than rotating a full 360°, the lidar unit was limited to a horizontal angle movement of only 0.13°. By restricting the horizontal rotation of the unit, we were able to scan the narrow profile along the flume rapidly (60 Hz), thus measuring the change in geometry as the debris-flow moved over the flume surface [41, 77]. We identify $t = 0$ in the lidar data by manually denoting the time when the gate opened. The lidar data was used to verify front position and velocity we derived from videos of each debris-flow.

4.3.2 Constructing a flow gather

Here we describe how to compute a flow gather from a video of a debris-flow at the flume. First, we establish notation for referring to a video, the video frames, and pixels within each frame. We denote the video as an ordered set $V = \{I_1, I_2, ..., I_k\}$, where $I_i \in \mathbf{R}^{h \times w}$ for $i \in [1, ..., k]$ denotes a frame, or image, with h rows and w columns. Each image I_i is

separated in time by a constant amount Δt; the frame rate of the video is $fps = \frac{1}{\Delta t}$. We denote pixel coordinates in an image using p, where each pixel coordinate p has a column x and row y; $I[p]$ refers to a pixel in image I at pixel p. When necessary, we can convert from frames i to time t using $t = i \times \Delta t$ where $t = 0$ s is when the gate opens to release the debris down the flume.

We focus our analysis on a slice through the video V along the flume axis. The slice is formed through pixel locations $P = \{p_1, p_2, ..., p_n\}$, which have corresponding distances down-flume $D = \{d_1, d_2, ..., d_n\}$, where p_1 and $d_1 = 0$ represent the location at the top of the flume. The pixel locations with known distance down-flume in P are manually picked once by hand along the flume axis as illustrated in Figure 4.1. The slice can be visualized as an image $S \in \mathbf{R}^{k \times w'}$, where w' denotes the number of pixels along the shortest path made by the hand-picked locations P. Each column of S represents a particular distance down-flume in pixels, each row in S represent a particular frame in the video. We seek a function that maps distance down-flume in pixels to distance down-flume in meters so that we can represent the appearance of the debris-flow surface from the viewpoint of the camera as a function of down-flume distance and time.

We find a function that maps pixel coordinates in P to their corresponding distances down-flume in D. We deduce this function by fitting a cubic-spline between corresponding pairs of pixel locations and distances down-flume. In other words, we find a cubic spline f that satisfies $f(p_j) = d_j$ for $j = \{1, ..., n\}$. We use f to convert the distance down-flume indicated by the column index in S from pixels to meters. The rows of S are converted from frame indices to time in seconds by multiplying by Δt.

After converting to distance in meters and time in seconds we construct a new image F we refer to as a flow gather. F has columns which represent distance down-flume in meters and rows that represent time in seconds. Thus, F represents the appearance of the debris flow surface as it evolves in time and space; slopes in the image F have units that correspond to the velocity down-flume during the debris-flow.

We use the slope of the warping function f to estimate the uncertainty in the position down-flume represented by each column of F. The perspective correction provided by the warping function f is not perfect, which implies that the derived position down flume for each pixel in a flow gather is also not perfect. The uncertainty of pixel locations warped by f to their coordinates down flume is computed by considering how much one pixel warps as a function of down flume distance (i.e. the slope of the warping function f). We denote the uncertainty in the warping function as ϵ_f. Since f is a cubic spline, we have access to an analytic form of the first derivative of f, which can be used to express positional uncertainty in the columns of a flow gather.

4.3.3 Quantifying surface velocity using a flow gather

As a debris-flow moves down the axis of the flume it changes in appearance in the video, and thus, in the flow gather. An advantage of displaying the debris-flow as a flow gather is that each pixel in the flow gather image relates the appearance of the debris-flow surface to a specific time and position down-flume. Thus, the velocity of certain features at the surface of a debris-flow can be measured by quantifying the inverse of the local slope of features in the flow gather, which have units seconds per meter. Here, we choose to quantify the local slope in a flow gather using structure tensor analysis. Structure tensors excel at describing local structure and have been used for densely analyzing the slope of features in images and for structure-oriented filtering applications [80–82]. We compute 2D structure tensors at each pixel in our flow gather image F. Each structure tensor is formed by smoothing the outer product of image gradients of F (i.e. the slopes in F); we denote the x component of the gradient of F as F_x and the y component as F_y. We use Sobel operators to compute image gradients and smooth using a Gaussian filter with a standard deviation of 3 pixels in F [83]. We denote the 2D structure tensor at pixel p as the 2×2 symmetric positive semi-definite matrix

$$\mathbf{T}[p] = \begin{pmatrix} (F_x[p])^2 & F_x[p]F_y[p] \\ F_x[p]F_y[p] & (F_y[p])^2 \end{pmatrix} = \begin{pmatrix} t_{11}[p] & t_{12}[p] \\ t_{21}[p] & t_{22}[p] \end{pmatrix}. \tag{4.1}$$

Hereafter we simplify notation and use $\mathbf{T}$ in place of $\mathbf{T}[p]$. The eigenvalue decomposition of $\mathbf{T}$ allows us to quantify the direction and magnitude of local structure. We denote the eigenvalue decomposition of $\mathbf{T}$ as

$$\mathbf{T} = \lambda_1 \mathbf{v}_1 \mathbf{v}_1^T + \lambda_2 \mathbf{v}_2 \mathbf{v}_2^T, \tag{4.2}$$

where $\lambda_1 \geq \lambda_2$ are eigenvalues of $\mathbf{T}$ corresponding to eigenvectors $\mathbf{v}_1$ and $\mathbf{v}_2$, respectively [81]. The direction of $\mathbf{v}_1$ aligns with that of the strongest image gradient; $\mathbf{v}_2$ aligns with smoothly varying coherent features in the image. The magnitude of λ_1 relates to the strength of structure along $\mathbf{v}_1$, whereas the magnitude of λ_2 relates to the strength along $\mathbf{v}_2$. So, when $\lambda_1 \approx \lambda_2$ the strength of structure along $\mathbf{v}_1$ and $\mathbf{v}_2$ are similar, thus indicating that the direction of structure in the image is ambiguous or isotropic. In our work we avoid interpreting structure in areas that have ambiguous directions of $\mathbf{v}_1$ and $\mathbf{v}_2$. A metric for quantifying how isotropic image gradients, and thus how ambiguous the direction of structures, are at the location of $\mathbf{T}$ can be computed using the eigenvalues of the structure tensor as

$$c = \frac{\lambda_1 - \lambda_2}{\lambda_1 + \lambda_2}, \tag{4.3}$$

which is often referred to as coherency [84]. If $\lambda_1 \approx \lambda_2$ then the coherency will be low, and therefore the image structure described by $\mathbf{T}$ is mostly isotropic. In contrast, high coherency implies that the eigenvalues of $\mathbf{T}$ are very different and thus structure aligns mostly with $\mathbf{v}_1$ (i.e. structure is more linear).

4.4 Results and Discussion

4.4.1 Flow gathers on May 23rd and May 25th, 2017 experiments

We successfully constructed flow gathers corresponding to each experiment on May 23rd and May 25th. In videos of each experiment, we selected 19 surveyed locations along the flume axis (Figure 4.1) in order to fit the smooth warping function f for converting distance in pixels to distance in meters (Figure 4.2a). We found that the uncertainty in f is largest for pixels located furthest up-flume and compute a mean uncertainty in f to be 0.055 m/pixel

with a standard deviation of 0.041 m/pixel (Figure 4.2b). Larger uncertainty in f up-flume is expected since the area represented by one pixel in the video increases with distance up-flume (Figure 4.1). The image S formed by slicing each video through the location of hand-picked surveyed points along the flume axis (Figure 4.3a) was warped using f to compute a flow gather F that showed the evolution of the appearance of the debris-flow as a function of time and down-flume distance for each experiment (Figures 4.3b, 4.4, and 4.5).

The flow gathers computed for the May 23rd and May 25th, 2017 experiments resemble an image of a brown wedge containing dipping features with vertical lines extending above the upper outline of the brown wedge (Figures 4.4 and 4.5). The brown wedge itself represents appearance of the debris-flow surface as a function of time and distance down-flume. The time and distance down-flume corresponding to the upper outline of the brown wedge in each flow gather (as outlined by the line labelled as "front pick" in Figures 4.4 and 4.5) represents the time and location of the debris-flow flow front. The vertical features in Figure 4.4 represent features along the flume axis that did not change in appearance. For example, the wide black vertical strip at approximately $d = 27$ m down-flume in Figure 4.4 was caused by the static bracket that held the laser flow-depth sensor at $d = 32$ m. Similar vertical black striping is observed near the laser flow-depth sensors at $d = 62.5$ and $d = 80.0$ m. The vertical features that are above the debris-flow flow front pick in Figure 4.4 represents the static appearance of the flume bed before the flow front arrives.

Non-vertical features in flow gathers represent changes in appearance with time and distance down-flume. For example, we note the presence of darker dipping features in the flow gather that coincide with increases in laser flow-depth thickness at $d = 32$ m (Figure 4.4). These dark, dipping features are caused by roll waves moving down the flume which are readily viewed in videos of the debris flow [57]. Roll waves are more abundant in the flow gather from May 25th (Figure 4.5). Many roll waves begin forming at $d = 20$ m down-flume and persist for times up to $t = 20$ s as the debris-flow evolves. We see that roll waves intersect and have varying dips which can readily be quantified by analyzing the slopes of

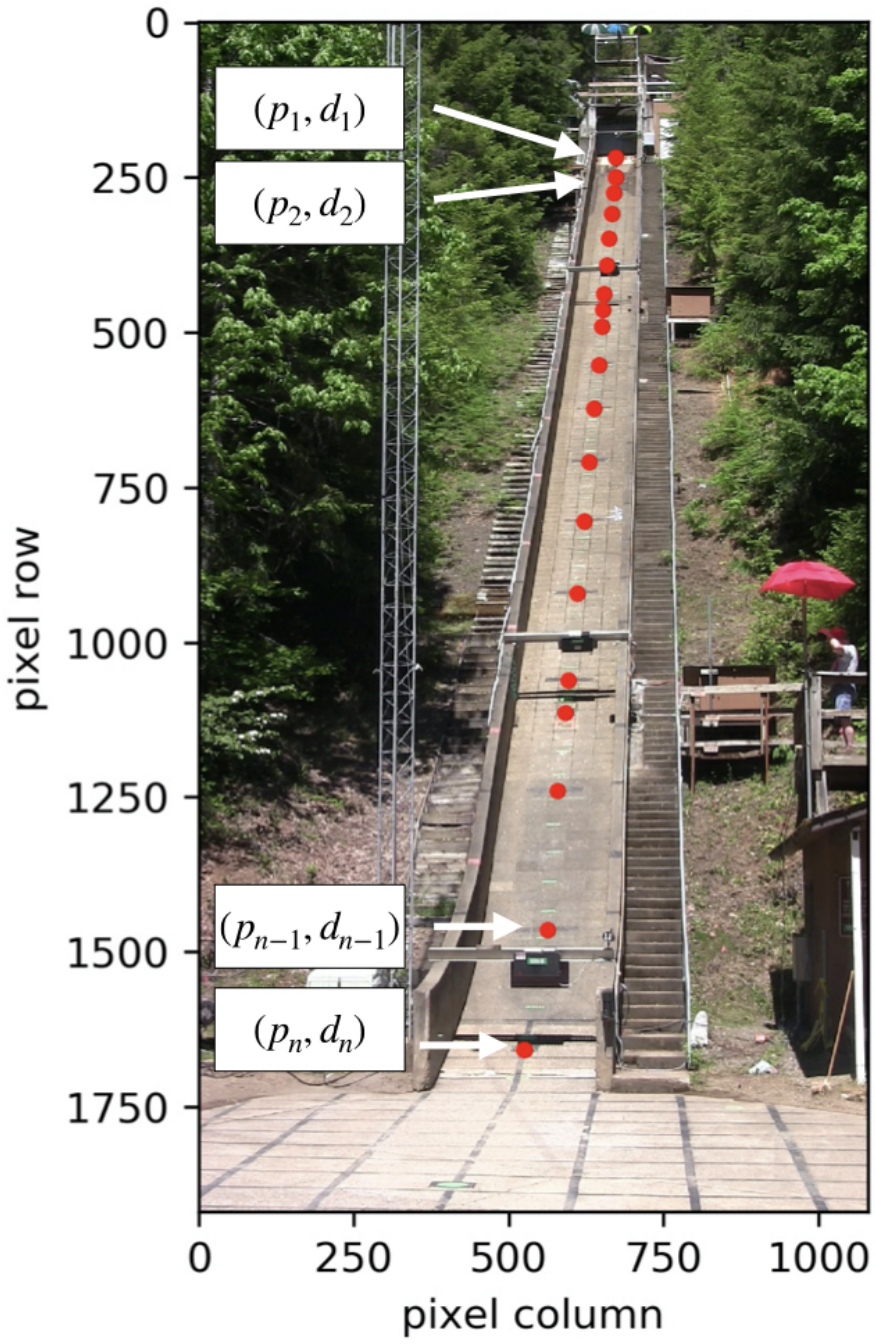

Figure 4.1: First frame of May 23rd video with hand-picked locations along the flume axis marked in red. Each location has a corresponding distance down-flume in p_i pixels and d_i in meters for $i \in \{1, ..., n\}$. These locations are used to form the warping function f for converting between distance in pixels to distance in meters.

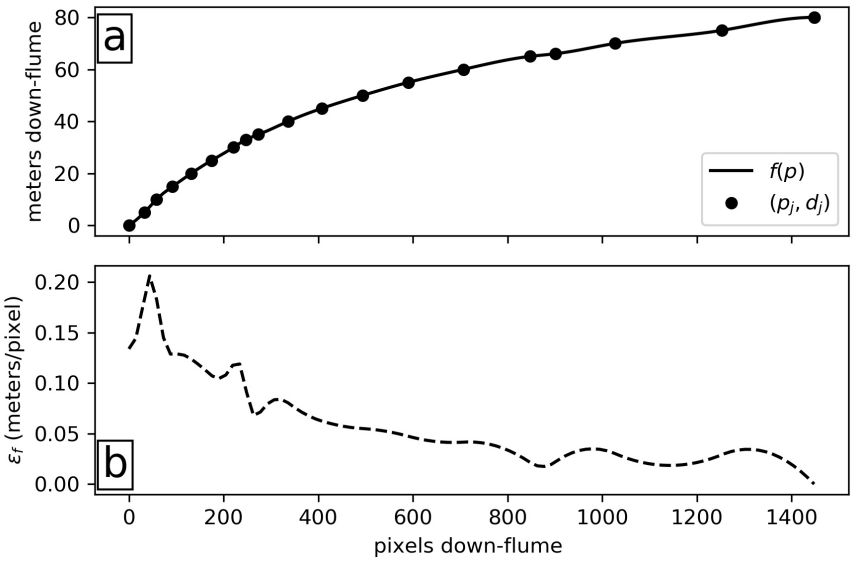

Figure 4.2: (a) Warping function to convert distance in pixels to distance in meters down-flume for the May 25th video and (b) the uncertainty in the warping function. Warping uncertainty is larger up-flume since pixels represent a larger area at those locations in the video (see Figure 4.1)

dark dipping features in the flow gathers.

4.4.2 Debris-flow flow front position and velocity

We focus our analysis of the debris-flow flow front position and velocity derived during the May 25th experiment in order to validate our video-based method for characterizing debris-flow motion (Figures 4.6, 4.7, and 4.8). First, we picked the debris-flow flow front on the flow gather on May 25th on flow gathers from video and lidar (Figure 4.6) and compared the front arrival time at each of laser flow-depth sensor locations (Figure 4.7). Both the flow-depth sensor and lidar measurements rapidly increased as the front passed over each of the sensor locations shown in each subplot of Figure 4.7. We observe a discrepancy in the arrival time that is fractions of a second between flow-depth sensor, lidar, and video-based measurements. These disagreements can be explained by the fact that the flow-depth sensors, lidar, and video were not measuring the front arrival time at the exact same location across the flume axis [77].

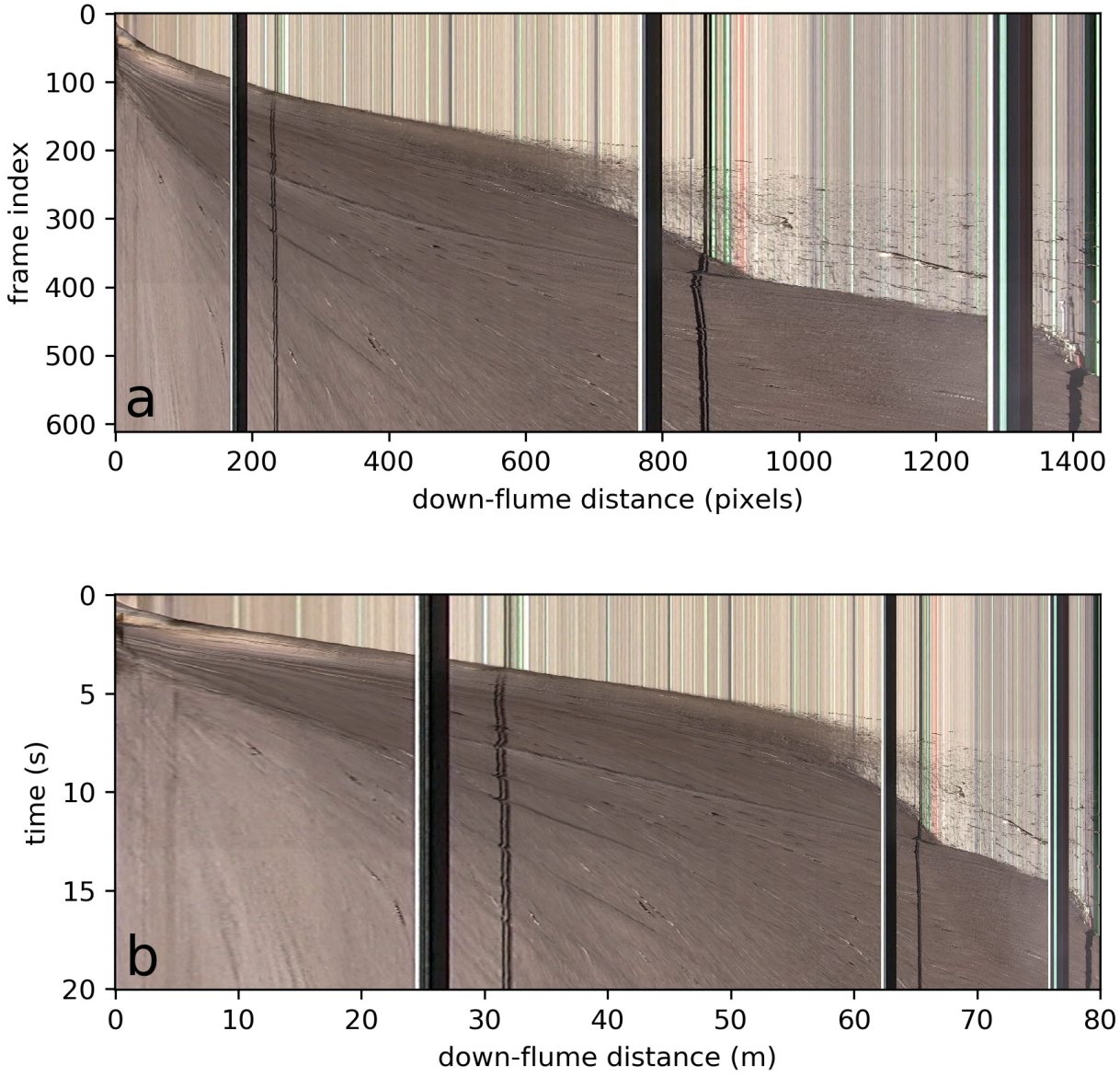

Figure 4.3: (a) Illustration of the pixel color from all frames as a function of down-flume distance. At each frame index (row) in (a), the down-flume distance in pixels is converted to down-flume distance in meters using the warping function f in order to construct a (b) flow gather. Results are shown for the May 23rd debris-flow. Detailed images of the flow gathers on May 23rd and May 25th are shown in Figures 4.4 and 4.5

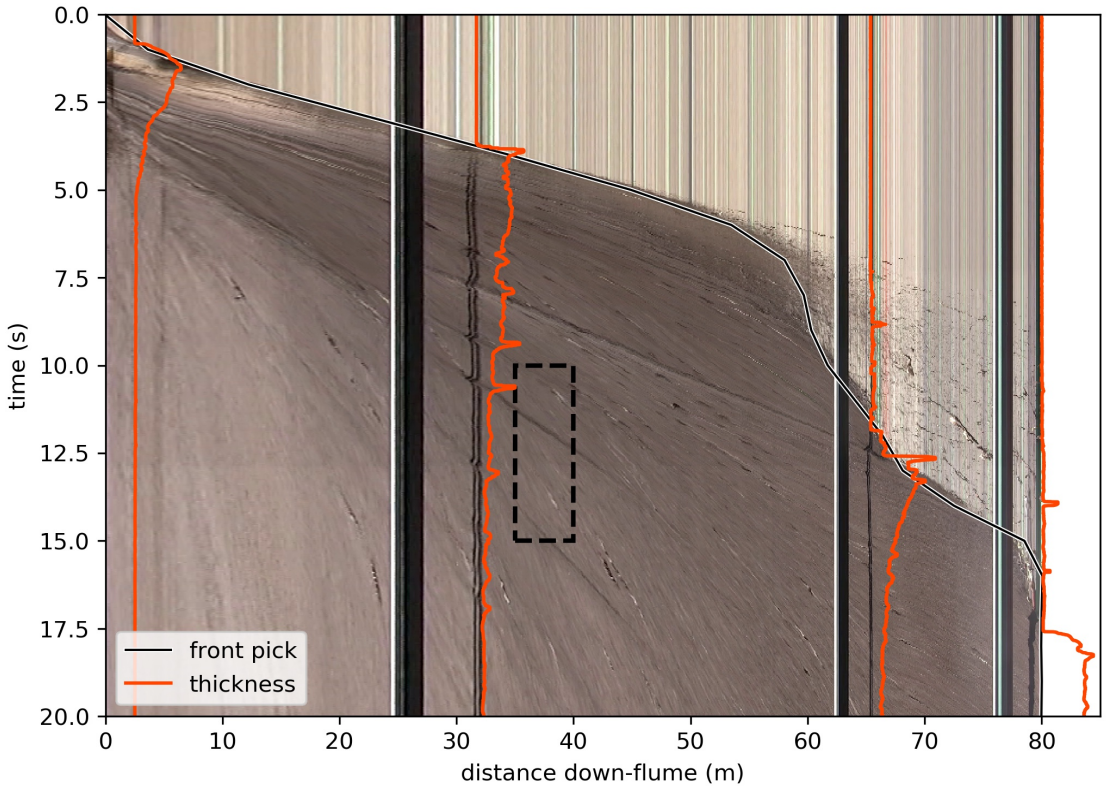

Figure 4.4: Flow gather from the May 23rd experiment with overlaying flow-depth sensor data. Flow-depth data are plotted at their respective locations as red curves and are scaled for displayed purposes with increasing flow-depth to the right. The flow-depth appears to increase when roll waves (dark linear streaks in the flow gather) move past each flow-depth sensor. The dashed black outline shows the zoomed area displaying structure tensors in Figure 4.9.

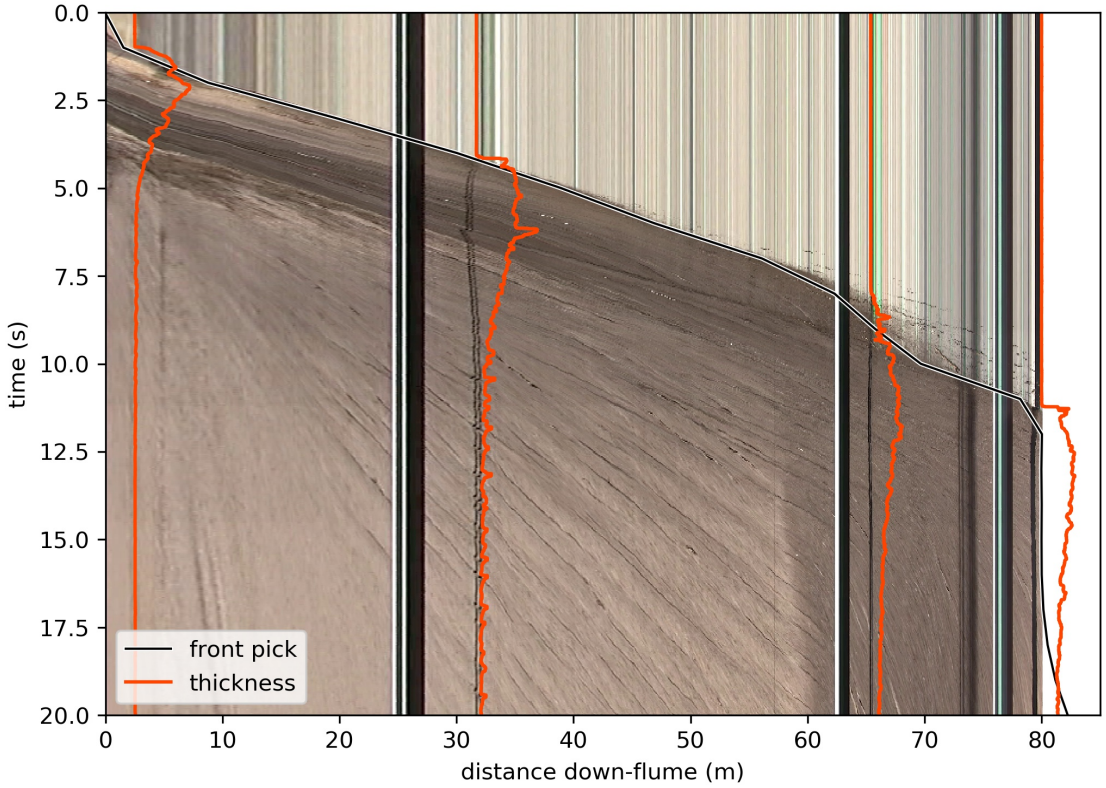

Figure 4.5: Flow gather from May 25rd experiment with overlaying flow-depth sensor data plotted in the same fashion as Figure 4.4. We see that flow-depth appears to change with the appearance in the flow gather. Roll waves are visible as dark dipping features in the flow gather. The velocity of each roll wave can be quantified by the inverse slope of each dark dipping feature.

We extend our comparison of lidar and video-based debris-flow flow front tracking beyond the location of the sparse flow-depth sensors and find that front arrival times measured using lidar and video agree at many positions along the flume (see Figure 4.8). During the May 25th experiment the lidar and video measurements both showed comparable arrival times and general shape for the flow front trajectory at all locations along the flume (Figure 4.8a) which shows that both methods are reasonable ways to track the flow front. However, the flow front derived using lidar is consistently earlier for times 0-10 seconds (Figure 4.8a), which is likely due to the lidar and video not sampling the same part of the debris-flow. We find the mean difference between front arrival times derived using lidar and video to be -0.36 s. This disparity in sampling can also explain the disagreement in the velocity profiles (Figure 4.8) as they appear to be shifted versions of each other.

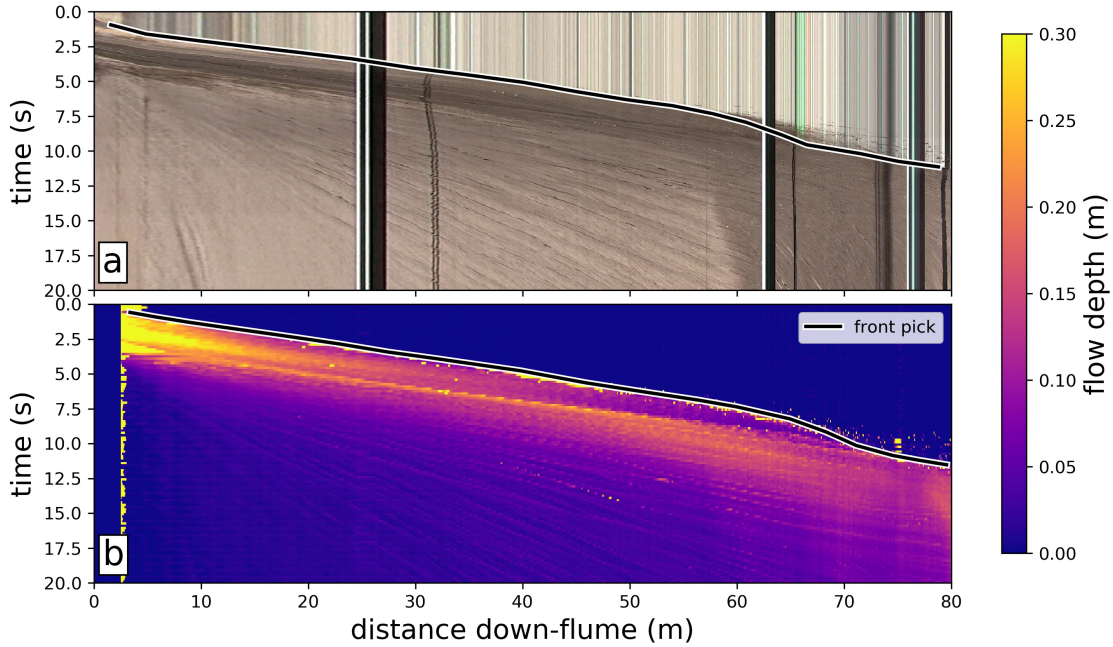

Figure 4.6: Flow gathers during May 25th experiment using (a) video and (b) lidar. The location of the front picked from video is plotted over each flowgather. We see that the features in (a) and (b) are similar for most times and distances down-flume. The largest difference in the arrival of the debris-front occurs around 10 seconds and distance of 70-80 m down-flume.

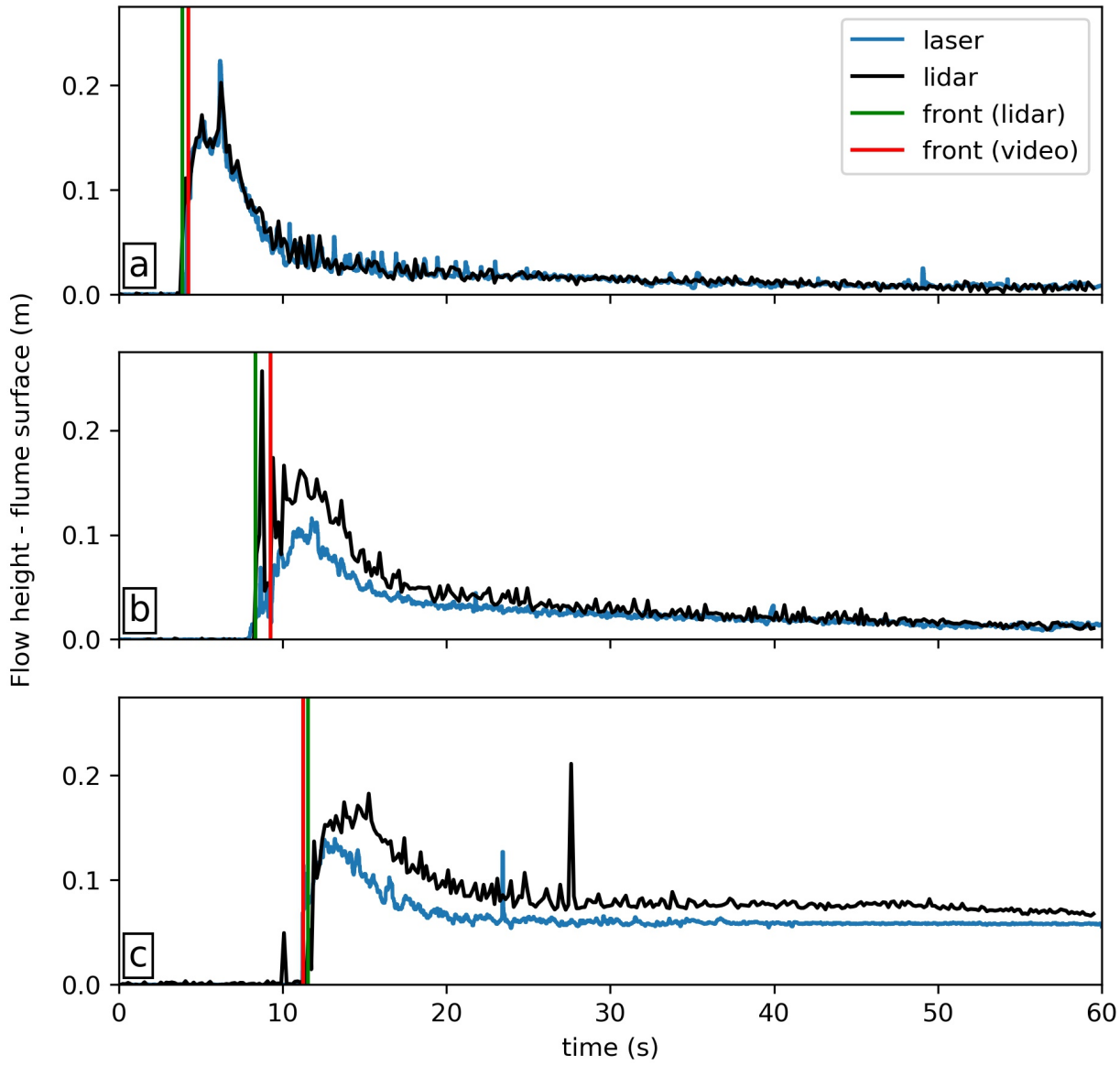

Figure 4.7: Vertical thickness as a function of time at flow-depth laser sensor locations (a) $d = 31.7$ m, (b) $d = 65.4$ m, and (c) $d = 80.0$ m for both lidar and flow-depth laser sensors. Lidar and flow-depth curves disagree since they sample a different location across the flume axis – especially at large distances down flume. The video-based flow front pick in red matches lidar-based flow front pick in green within fractions of a second, which can also be explained by the two sensors measuring the front location at different locations across the flume axis.

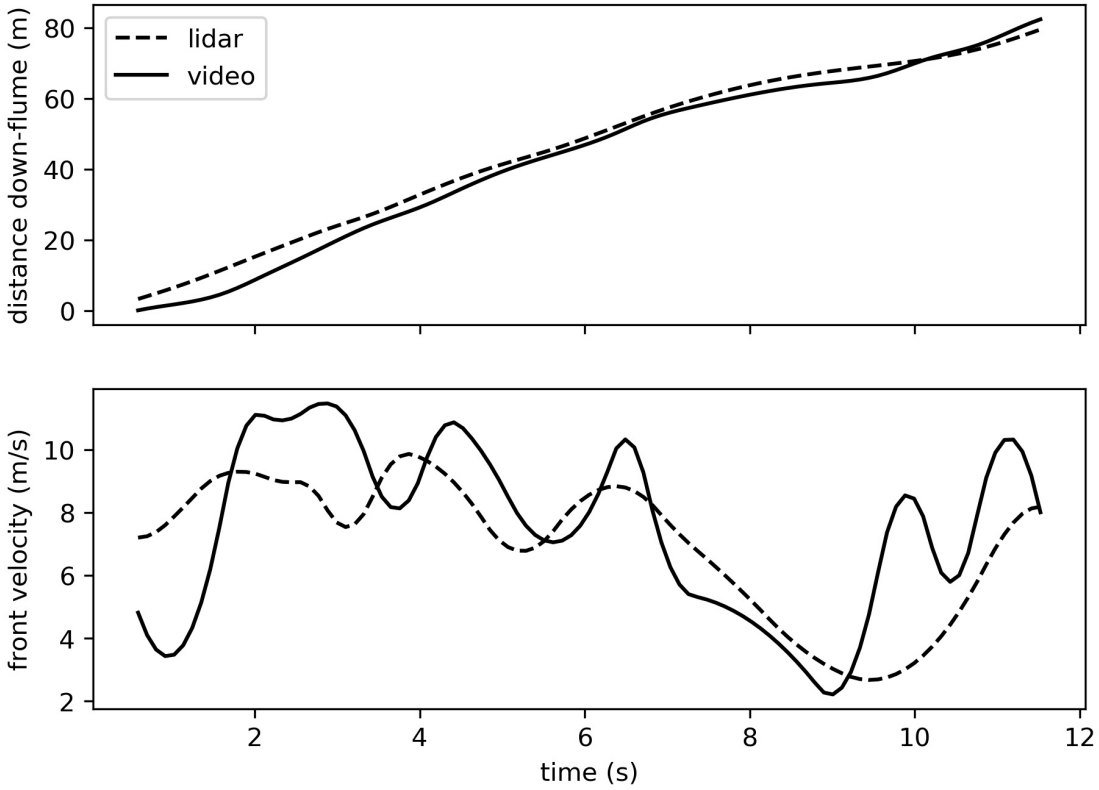

Figure 4.8: Flow front (a) position and (b) velocity for the May 25th debris-flow experiment according to video and lidar. The front position derived from video matches that derived from lidar with a mean front arrival time difference of -0.36 s. Front velocity from lidar and video appear as shifted versions of one another due to each sensor sampling slightly different positions along the flume axis.

4.4.3 Debris-flow surface velocity

The surface velocities derived from lidar and video data show general agreement (Figures 4.10b-c). As expected, during both experiments the surface velocity generally decreased as the debris-flow slowed down. The structure tensors used to compute velocities in a flow gather aligned with local structure (see Figure 4.9). We exclude results for structure tensors and velocities in areas with lower coherency since low coherency implies more ambiguous slope estimates, and therefore more ambiguous velocity estimates. Specifically, we exclude velocities derived from tensors whose coherency is below 0.2. The coherency maps show strong linear features for each of the experiments (Figure 4.10d-f) which can readily be interpreted. These events are highly resolved in the lidar flow gather coherency map (Figure 4.10f), and show oscillatory characteristics which may be interpreted as oscillations in dip caused by roll waves. Surface velocities computed from lidar appear to be more finely resolved than those derived using video, but the magnitude of the surface velocities are different yet comparable (Figures 4.10 and 4.11).

We use the empirical probability distribution function (PDF) of surface velocities and coherencies derived from lidar and video to describe and analyze notable differences between the two measurement systems (Figure 4.11). In general, more low surface velocities are recovered by both sensors, but lidar recovers more high surface velocity values and more high coherency values (Figure 4.11). These differences are likely due to several factors. Video measures changes in appearance and lidar measures geometric change. In addition, video and lidar do not sample the flume at the exact same locations, nor do they have the same temporal and spatial sampling resolution (lidar data have higher spatiotemporal resolution than video). The discrepancy in resolution is probably the cause for the higher coherency values in lidar than video; finer features resolved at finer resolution will appear more coherent when computing a structure tensor (Figure 4.11b). Additionally, noise in the high resolution lidar data will appear as fine features in the lidar flow gather and may be the cause for more high surface velocity values being recovered by lidar. Based on these

results, we are more certain in the flow front comparison agreement between lidar and video than the computed surface velocities. It is difficult to say, definitively, which system is more accurately measuring surface velocity. However, we are encouraged by finding that the range and general shapes of PDFs for derived surface velocities are similar when using lidar or video.

4.5 Conclusion

We present a method for measuring debris-flow front position, velocity, and surface velocity at the U.S Geological Survey debris-flow flume from a single video. Our video-based measurements agree with similar lidar-based measurements within reason considering the experimental setup and expected uncertainty in video-based results. The output from our method is an image we call a flow gather that can be directly interpreted or processed further to identify and quantify key flow characteristics such as roll waves. We promote using flow gathers to retroactively process videos of debris-flows at the flume to more completely understand debris-flow front and surface velocity evolution. Future work for improving the method we present could involve considering multiple slices along the flume axis for constructing a flow-gather as a volume, instead of an image, which would allow both down-flume and across-flume positions and velocities to be measured and analyzed.

4.6 Acknowledgements

This work was supported by the U.S. Geological Survey Landslide Hazards Program. The use of trade, product or firm names in this paper is for descriptive purposes only and does not constitute endorsement by the U.S. Geological Survey. Videos summarizing the experiments can be found at `https://pubs.usgs.gov/of/2007/1315/videos/2017` [57]. Laser-based flow-depth data is available at `https://doi.org/10.5066/P9QSZ4XO` [85]. The lidar data can be obtained at `https://doi:10.5066/P94GGE3G` [79].

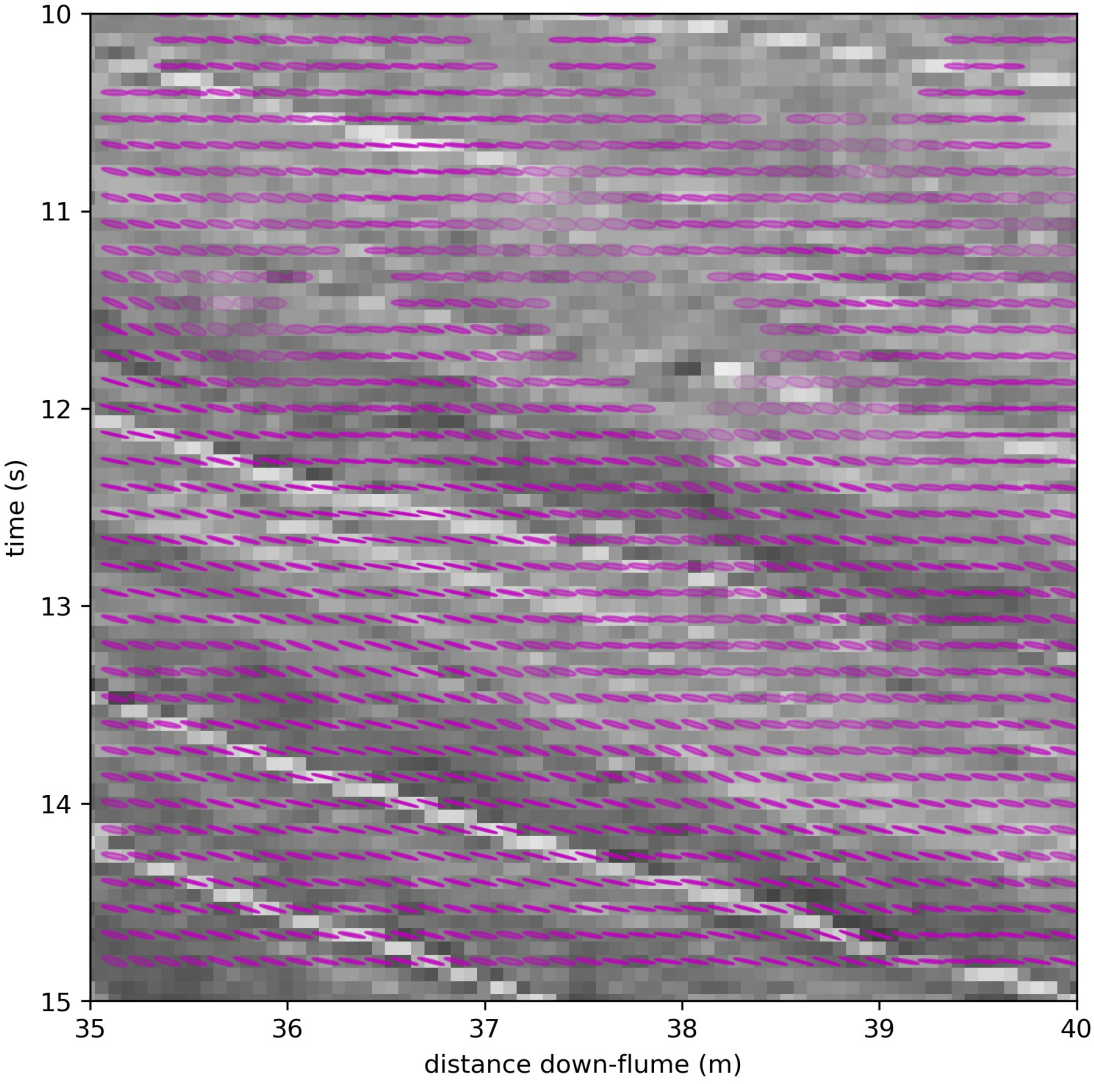

Figure 4.9: Zoomed in view of structure tensors computed on the May 23rd flow gather. Zoomed in region is outlined by the dashed line in Figure 4.4. Structure tensors are plotted as magenta ellipses with the minimum eigenvector direction aligning with the major axis of each ellipse. Structure tensors with higher coherency are plotted with more intense color; low coherency structure tensors are plotted with more opacity. We see that in areas where structure is ambiguous, the coherency is low. In areas with strongly dipping structure the coherency is high.

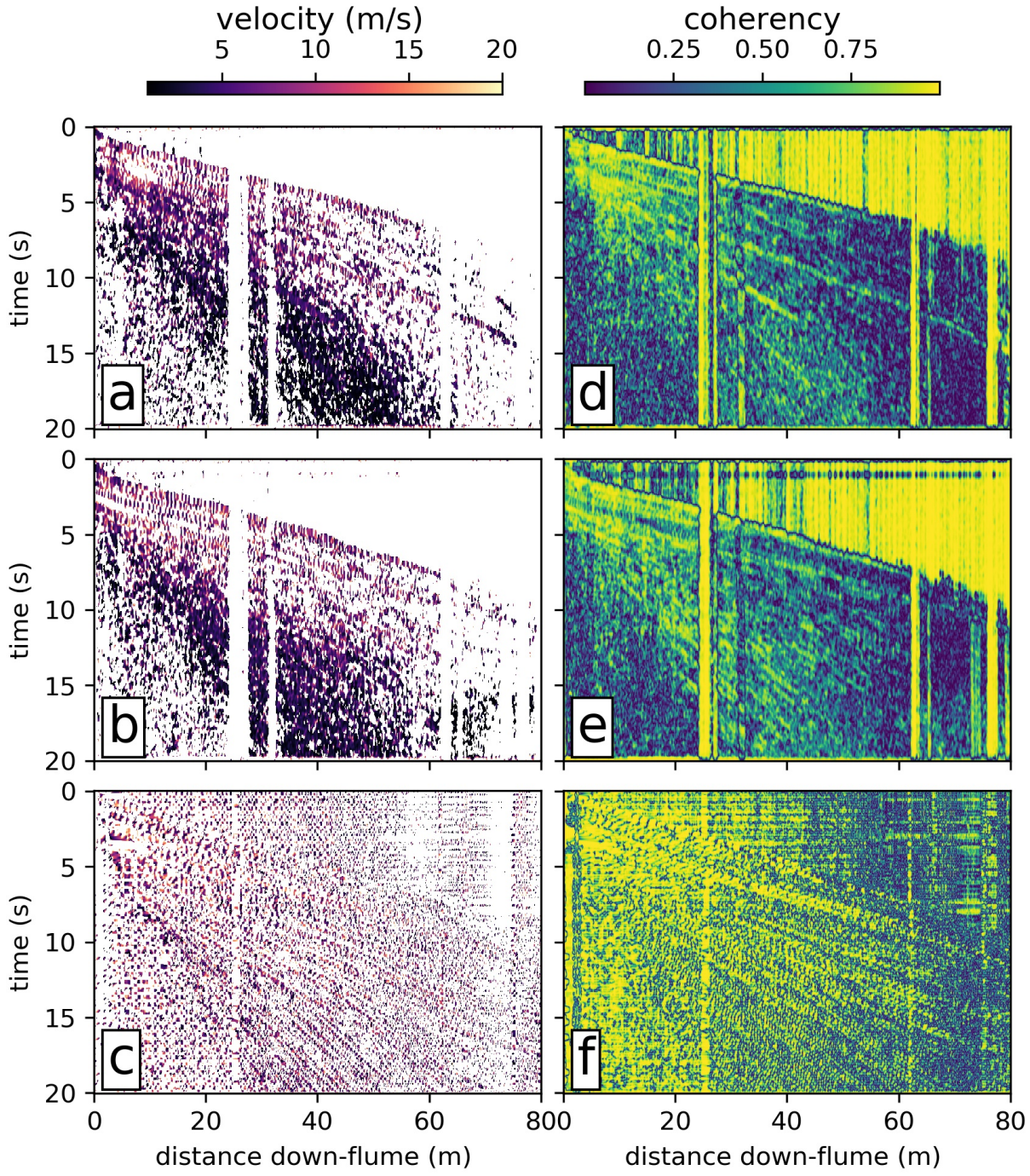

Figure 4.10: (a-c) Surface velocity estimates and (d-f) coherency values derived from flow gathers on (a & d) May 23rd and (b & e) May 25th experiments. (c & f) Surface velocity and coherency derived from lidar measurements on May 25th. Surface velocities derived from structure tensors with coherency below 0.2, below 1 m/s, or above 30 m/s are not displayed.

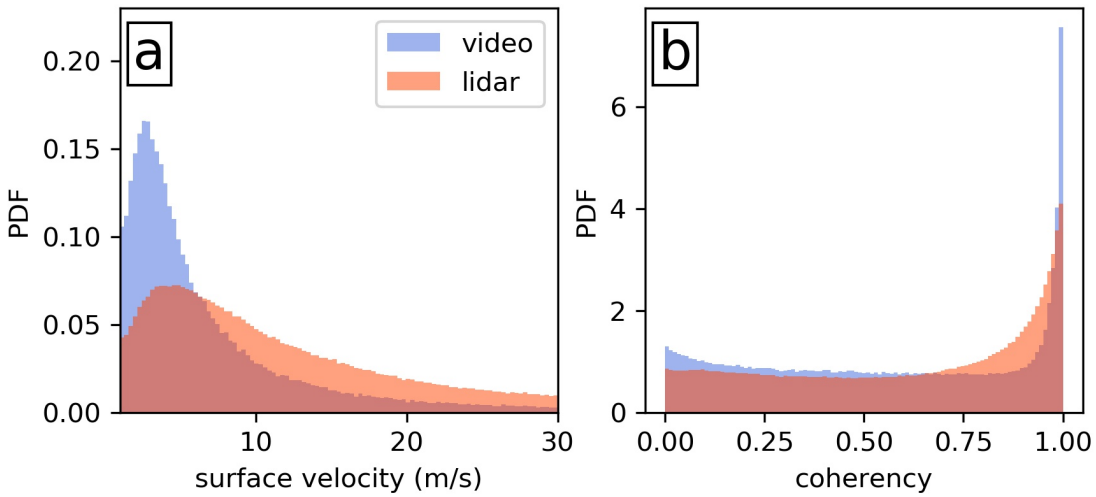

Figure 4.11: Empirical PDFs for (a) surface velocity and (b) coherency from lidar and video on May 25th experiment as shown in Figure 4.10. The distributions do not match exactly, but more low surface velocities are recovered by both sensors. Lidar tends to measure higher velocities, likely because it is a higher resolution instrument than video and measures geometric changes rather than appearance changes. Additionally, lidar-based structure tensors, in general, exhibit less low-coherency than video-based structure tensors as shown in (b).

CHAPTER 5

SEPARATING SENSOR MOTION FROM SEISMIC MOTION

Ready to submit

Thomas D. Rapstine[1,2], Paul Sava[2]

Airborne seismic data acquisition requires excellent knowledge of the sensor's position and orientation since distance measurements made from an airborne sensor represent a combination of platform and ground motion. The motion of a stabilized sensor on a hovering airborne platform, such as a camera or lidar system mounted on a drone, may not change much over the duration of a typical active seismic record (a few seconds). Evidence of this can be found even in modest consumer grade drones which produce stunningly smooth videos. Recent advancements in laser Doppler vibrometry and repeat lidar surveys show that the frequency and resolution of non-contact motion measurements is increasing to the point necessary for measuring seismic signals. We explore the conditions under which separation of drone motion from ground motion can be accomplished in practice. We assume (1) that the translation and rotation of the stabilized sensor follows an analytic form in time that is either known or can be estimated from the sensor's measurements, (2) that the seismic signal we observe has compact support contained within the measurement window, and (3) that the ground motion can be described by a rigid translation. We analyze the effectiveness of our signal separation problem as a function of peak signal, sensor noise level, sensor rotation angle, and sensor point sampling density by defining a boundary defining when $SNR = 0$ dB for various combinations of these parameters. We find that under the set of assumptions, lower rotation angles, lower sensor noise, and denser point samplings on the ground allow for better signal separation using our method.

[1]Primary researcher and author.
[2]Department of Geophysics, Colorado School of Mines, Golden, Colorado, United States of America.

5.1 Introduction

The ability to gather seismic data from an airborne platform would open new opportunities in seismology and exploration seismic. Airborne surveys could be faster, less environmentally impactful, and cheaper than current terrestrial alternatives. However, airborne seismic acquisition requires removing the negative effects of platform motion from the measurements [86, 87]. Previous virtual simulations have shown that modest airborne stereo video systems would be capable of measuring 1D displacements below a few millimeters from a height of a few meters, provided the aircraft position and orientation are precisely known [87, 88]. However, in reality the exact position of an airborne sensor is not known with arbitrary accuracy. In addition, measurement of 3D ground displacement would be a desirable for seismic measurement since motion due to seismic wave propagation is inherently 3D. Here, we avoid the requirement to know precisely the drone motion, and instead establish a method for removing sensor motion that remains after the sensor is stabilized in order to recover the 3D displacement of the ground. We test the method in a virtual simulation to identify the conditions under which airborne seismic measurements are achievable in practice. We are inspired by recent successful applications of remotely measuring seismic signals using laser Doppler vibrometer (LDV) systems and by the demonstrated sensitivity of high speed video to subtle vibrations, which we summarize next.

Much progress has been made recently in proving the feasibility of LDV-based seismic measurements from stationary, mobile, airborne, and even space-borne platforms. The feasibility of remotely detecting ground motion caused by seismic waves was proven successful from a stationary platform positioned 800 m away from a vibrating target of interest [23, 24]. More recently, work by Dräbenstedt et al. [86] shows that a closer, yet mobile, LDV system equipped with a vibration isolation system can enable remote seismic measurements from a terrestrial vehicle, even in a windy acquisition environment. We note that Dräbenstedt et al. [86] alludes to extending LDV-based seismic measurements to airborne platforms, but they cite a need for better clock synchronization, sensor vibration isolation, and methods

for removing residual motion measured by a reference sensor before doing so. The effect a moving platform has on LDV measurements including the so-called "speckle noise" may be addressed by multiple independent LDV sensors and signal processing algorithms such as Maximal Ratio Combining [89–92]. Maximal Ratio Combining leverages an assumption of independence between the LDV signals and the physics of speckle noise to enable measuring signals hidden by noise induced from a moving platform and the speckle pattern. This concept has been explored and analyzed even for satellite-borne LDVs in the context of conducting seismic surveys on asteriods or comets [92]. Whether on land, air, or in space an LDV still measures velocity at a single point whereas a distributed measurement of motion, in the form of displacement, may be available from video cameras.

High speed cameras have been shown to successfully measure minute vibrations that cause changes in color. A technique known as motion magnification enables measuring subtle vibration using high-speed video by isolating spatiotemporal changes at specified image scales and frequencies [9–13]. Motion magnification has successfully been used in a variety of applications including inferring structural composition from high speed video [93], deducing vibrational modes of a structure [94], measuring heart-beats [95], and recording audible speech by filming a vibrating object [96]. However, motion magnification does not quantify the amplitude of motion we seek when recording seismic data, and only measures variations in color. Another technique, repeat lidar, does allow for the amplitude of motion to be quantified, which is required when conducting a seismic survey.

Repeat lidar enables non-contact measurements of ground displacement which may improve in accuracy to a point that allows seismic signal measurement. Lidar technology has improved over recent years and is currently being used to measure large-scale geomorphic changes at the Earth's surface, for example due to a landslide or debris-flow. Geomorphic changes are being measured via repeat lidar at increasingly higher frequencies from years [4, 6] to months [3, 5, 76] to hours [7, 8] and even to sub-second intervals in controlled large-scale laboratory settings [41, 77]. Given recent advancements in LDV, high-speed video, and

lidar technologies, we anticipate that a non-contact airborne sensor will soon be developed with the ability to measure a dense array of points on the ground with accuracy necessary for seismic exploration. However, the problem of removing platform motion from airborne measurements would remain and provides motivation for the work we present here.

We establish a signal separation technique that removes the negative effects of residual platform motion after attempted hardware sensor stabilization. Our technique works under a set of assumptions relevant for an airborne sensor that has been largely stabilized, but still experiences residual platform motion. Along with ground displacement, our method provides an estimate of measurement uncertainty that is currently not available from conventional geophone measurements. In what follows, we outline a simulation framework to test our method, our signal separation strategy, and test its effectiveness for a range of scenarios. We establish guidelines for when our method would be effective by measuring the signal-to-noise (SNR) ratio for various realistic combinations of sensor rotation angle, maximum peak seismic signal, and the density of point measurements on the ground. We conclude by outlining technological advances needed to realize airborne seismic acquisition.

5.2 Methods

5.2.1 Airborne sensor motion model

Establishing an airborne sensor motion model is necessary in order to simulate how a sensor moves. In our work, we denote time as t_i for $i \in \{0, \ldots, T-1\}$ where samples are separated by a constant interval Δt and T denotes the number of times. We denote the position of the sensor as $\mathbf{r}_i = (r_x[i], r_y[i], r_z[i])^T$ and the orientation as $\boldsymbol{\theta}_i = (\theta_x[i], \theta_y[i], \theta_z[i])^T$ for $i \in \{0, ..., T-1\}$. $\boldsymbol{\theta}$ contains the Euler angles about the x-, y-, and z-axes which are necessary to describe 3D orientation. For example, a linear motion model may be written as

$$\mathbf{r}_i = \mathbf{r}_c t_i + \mathbf{r}_0 \tag{5.1}$$
$$\boldsymbol{\theta}_i = \boldsymbol{\theta}_c t_i + \boldsymbol{\theta}_0, \tag{5.2}$$

where $\mathbf{r}_0 \in \mathbb{R}^{3\times1}$ is the initial position of the sensor, $\boldsymbol{\theta}_0 \in \mathbb{R}^{3\times1}$ its initial orientation, and $\mathbf{r_c} \in \mathbb{R}^{3\times1}$, and $\boldsymbol{\theta_c} \in \mathbb{R}^{3\times1}$ denote the rate of change in its position and orientation. Other motion models could include higher order terms, such as t^2 or t^3, or even contain periodic terms involving trigonometric if sensor vibration is suspected. In reality, the appropriate sensor motion model depends on the sensor stabilization system. A high quality stabilization system may eliminate sensor vibrations, but a lower quality and more realistic system may result in residual sensor vibration that would be necessary to account for in the sensor motion model. We keep the concept of the sensor motion model general and only assume it is a function of time; that way our separation strategy can be used for a variety of motion model situations.

Given a sensor's position and orientation, we construct a matrix that performs a coordinate system transformation from a world coordinate system to the sensor's local coordinate system. We denote the rotation matrix for the sensor at t_i as $\mathbf{R}_i \in \mathbb{R}^{3\times3}$, which is formed using $\boldsymbol{\theta}_i$. We use $\mathbf{R}_i$ and the position of the sensor $\mathbf{r}_i$ to form a matrix $\mathbf{H}_i \in \mathbb{R}^{4\times4}$ that represents a coordinate transformation from a (global) world coordinate system to the (local) coordinate system of the airborne sensor at t_i

$$\mathbf{H}_i = \begin{bmatrix} \mathbf{R}_i & \mathbf{r}_i \\ \mathbf{0} & 1 \end{bmatrix}. \tag{5.3}$$

Conversely, we can transform a point from the sensor's coordinate system into world coordinates using the inverse transformation

$$\mathbf{H}_i^{-1} = \begin{pmatrix} \mathbf{R}_i^T & -\mathbf{R}_i^T\mathbf{r}_i \\ \mathbf{0} & 1 \end{pmatrix}. \tag{5.4}$$

In order to apply the coordinate transformation matrices $\mathbf{H}_i$ or $\mathbf{H}_i^{-1}$, to a 3D point, $\mathbf{x} = (x_1, x_2, x_3)^T$, we must represent the position $\mathbf{x}$ in homogenous coordinates as

$$\tilde{\mathbf{x}} = \begin{pmatrix} x_1 \\ x_2 \\ x_3 \\ 1 \end{pmatrix}. \tag{5.5}$$

Homogeneous coordinates are commonly used in computer vision applications of projective geometry since they allow a coordinate system transformation to be represented using a single matrix-vector product [2]. Hereafter we denote by a tilde ($\tilde{\cdot}$) the points or sets that are expressed in homogeneous coordinates. A point $\tilde{\mathbf{x}}$ in homogenous coordinates can be represented in 3D coordinates by dividing by the fourth element in $\tilde{\mathbf{x}}$:

$$\tilde{\mathbf{x}} = \begin{pmatrix} a \\ b \\ c \\ d \end{pmatrix} \rightarrow \mathbf{x} = \begin{pmatrix} \frac{a}{d} \\ \frac{b}{c} \\ \frac{c}{d} \end{pmatrix} = \begin{pmatrix} x_1 \\ x_2 \\ x_3 \end{pmatrix}. \tag{5.6}$$

$\mathbf{H}_i$ represents how points in the world coordinate system appear in the sensor's local coordinate system, which varies with time as does the seismic signal. A primary goal necessary to achieve for realizing airborne seismic acquisition is to remove the effects of $\mathbf{H}_i$ from sensor measurements of displacement in order to only recover ground displacement due to seismic wave propagation.

5.2.2 Defining a seismic signal model

We establish a seismic signal model with compact support in time which describes the translation of the ground surface observed by an airborne sensor. The concept of compact support physically represents a seismic signal that is non-zero for a finite amount of time and is a convenient property that allows us to establish a tractable signal separation strategy. A seismic signal observed by a rotating and translating sensor would appear to be non-zero even if the seismic signal is zero. However, if we assume that observation begins before the seismic signal is non-zero and ends after the support of the seismic signal, then we know that nonzero observations at the beginning and end of the measurement are only caused by the sensor motion. Thus, outside the support of the seismic signal, we can use displacement measurements to estimate the sensor motion model parameters (e.g. $\mathbf{r_c}$, $\mathbf{r}_0$, $\boldsymbol{\theta}_c$, or $\boldsymbol{\theta}_0$) without worrying about the effects of the seismic signal.

We choose to use discrete wavelets to reconstruct the seismic signal since, by design, discrete wavelets have compact support and can resemble seismic signals. We use Daubachies

wavelets with two vanishing moments since they appear wave-like and are efficient to compute [97]. We denote the 3D seismic signal as $\mathbf{s}_i = (s_x[i], s_y[i], s_z[i])$ for $i \in \{0, \ldots, T-1\}$. Each component of $\mathbf{s}$ is independently constructed using a linear combinations of N randomly shifted Daubachies wavelets at random scales; we only consider wavelets whose support is limited in $[a, b]$, where $a > 0$ and $b < T$. By only including wavelets with support in the interval $[a, b]$ we assume, physically, that the seismic signal is only non-zero in that particular interval. We label a random variable representing these wavelets as W, and note samples drawn from W as $w \in \mathbb{R}^{T \times 1}$. Using randomly generated w, we construct each component of $\mathbf{s}$ as

$$s_x = c \sum_{n=0}^{N-1} w \tag{5.7}$$

$$s_y = c \sum_{n=0}^{N-1} w \tag{5.8}$$

$$s_z = c \sum_{n=0}^{N-1} w, \tag{5.9}$$

where $n = \{0, 1, \ldots, N-1\}$ and the weight c is chosen such that the maximum peak amplitude of $\mathbf{s}$ is s_{max}. The resulting seismic signals look realistic and have the benefit of being randomly generated (Figure 5.1). We use these randomly generated signals to construct synthetic seismic data for testing our signal separation method.

5.2.3 Topography as a randomly generated smooth surface

The simulated seismic signals translate the ground surface topography, which we represent as a set of k points sampling a surface of varying smoothness. We refer to this set as a point cloud, which can be represented as a matrix

$$\mathbf{P} = \begin{pmatrix} \mathbf{p}_0 & \mathbf{p}_1 & \ldots & \mathbf{p}_{k-1} \end{pmatrix} \tag{5.10}$$

where each column of $\mathbf{P}$ contains the 3D coordinates of a point. Points in the columns of $\mathbf{P}$ lie on a $n_x \times n_y$ grid (where $k = n_x \times n_y$) where the spacing between points is Δx

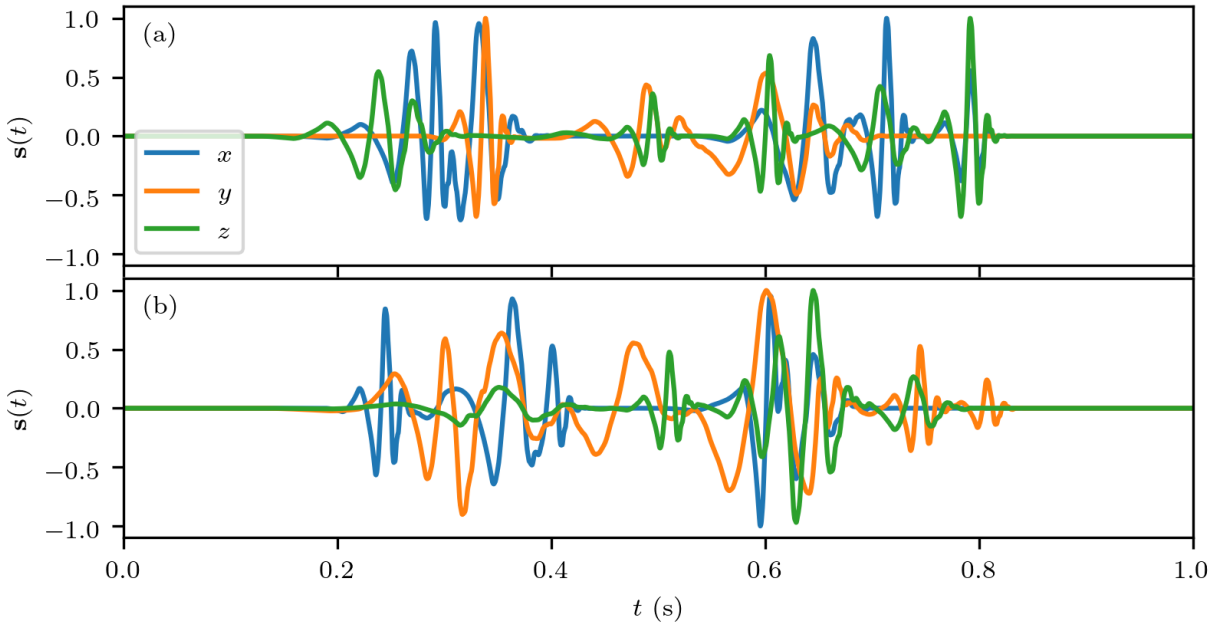

Figure 5.1: (a & b) Examples of randomly generated 3D seismic signals. The signals shown have compact support in the interval [0.2, 0.8] s. We estimate the sensors motion model using measurements taken outside the seismic signals support, then infer it inside the seismic signal support using an assumed sensor motion model.

in the x-direction and Δy in the y-direction. The z-coordinates (i.e. topography) at each point is populated with values drawn from a uniform distribution between z_{min} and z_{max}. This enables us to generate many random point clouds that lie on the same grid in x and y. Since the point cloud x and y coordinates lie on a grid, we can conceptualize it as a 2D function, or image, of topography (the z-coordinates in the point cloud). In order to induce a certain smoothness on topography, we apply a 2D isotropic Gaussian filter characterized by a standard deviation of σ_t to the gridded z-coordinates. Near the edges of the grid we assume a

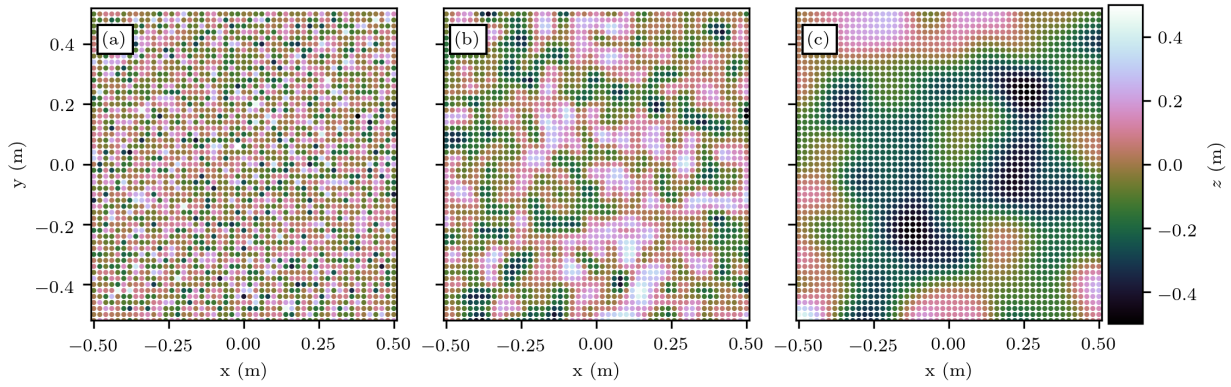

Figure 5.2: Map-view of simulated topography with varying smoothness; (a) no smoothing, (b) smoothing with σ_t=1, and (c) σ_t=2. Topography is translated by a seismic signal during our simulations and has the benefit of being randomly generated.

zero-slope condition when applying the filter, ensuring consistently smooth topography near the edges. Large values of σ_t lead to point clouds that sample smoother surfaces; smaller values of σ_t lead to less smooth point clouds (Figure 5.2).

5.2.4 Simulating a moving surface as viewed from a noisy airborne sensor

We seek to represent the ground surface moved by a seismic wave as viewed from a noisy airborne sensor that is also moving and rotating. To do this, we represent a dynamic point cloud by first translating all points in $\mathbf{P}$ by $\mathbf{s}_i$. Then we apply a rigid body transformation to all points using the coordinate transformation matrix $\mathbf{H}_i$ to represent them in the sensor's coordinate system at t_i. At each time t_i we observe a point cloud, represented as a matrix

$\tilde{\mathbf{Q}}_i \in \mathbb{R}^{4\times k}$, whose columns are

$$\tilde{\mathbf{q}}_j = \mathbf{H}_i(\tilde{\mathbf{p}}_j + \tilde{\mathbf{s}}_i), \tag{5.11}$$

for $j \in \{0, ..., k-1\}$. We note that the columns of $\tilde{\mathbf{Q}}_i$ are in homogenous coordinates, and can be represented in non-homogenous coordinates as the columns of an equivalent matrix, $\mathbf{Q}_i \in \mathbb{R}^{3\times k}$. $\mathbf{Q}_i$ represents the position of all points on the ground at time t_i as observed from a noiseless sensor's coordinate system. Our objective is to undo each rigid body transformation $\mathbf{H}_i$ in order to separate out the seismic signal $\mathbf{s}$. Moreove, we simulate noisy observations, $\hat{\mathbf{Q}}_i$, by adding noise drawn from a Gaussian distribution with zero mean and standard deviation σ to each observation in $\mathbf{Q}_i$. Uncorrelated noise is added independently to each point for each component (x, y, z) at each time t_i.

5.2.5 Separating platform motion from seismic signals

We leverage an airborne platform motion model (e.g. Equation 5.1) and the assumed compact support of the seismic signal $\mathbf{s}$ to develop a tractable signal separation strategy. Our strategy is to use observations to find the position and orientation of the airborne sensor outside the support of the seismic signal, then use knowledge of the sensor motion model (Equation 5.1) to infer the position and orientation of the airborne sensor during the support of the seismic signal. In order to describe this strategy, it is convenient to denote the indices $i_{in} = \{a, a+1, ..., b-1\}$ and $i_{out} = \{0, 1, ..., a-1, b, b+1, ..., T-1\}$ as those inside and outside the support of the seismic signal $\mathbf{s}$, respectively. The times corresponding to i_{in} and i_{out} are denoted as t_{in} and t_{out}, respectively.

Let us first consider how to find the motion of the airborne platform outside the support of the seismic signal during t_{out}. At $t_0 = 0$ the seismic signal does not influence the observations of the topography, therefore we define the world coordinate system origin and orientation as the initial position and orientation of the airborne sensor. This implies that at t_0 the point cloud representing topography in world coordinates is equal to the point cloud represented

in the airborne sensor's coordinates

$$\mathbf{Q}_0 = \mathbf{P}. \tag{5.12}$$

In addition, this implies that the initial position and orientation of the airborne sensor are

$$\mathbf{r}_c = (0,0,0)^T, \tag{5.13}$$

and

$$\boldsymbol{\theta}_c = (0,0,0)^T, \tag{5.14}$$

respectively. As the sensor translates and rotates during t_{out} each point at the ground surface is observed as

$$\tilde{\mathbf{q}}_j = \mathbf{H}_i \tilde{\mathbf{p}}_j, \tag{5.15}$$

or in physical coordinates as

$$\mathbf{q}_j = \mathbf{R}_i \mathbf{p}_j + \mathbf{r}_i. \tag{5.16}$$

Considering all $\mathbf{q}_j$ at a single time $t_i \in t_{out}$ we form a matrix of observations as

$$\mathbf{Q}_i = \begin{pmatrix} \mathbf{R}_i \mathbf{p}_0 + \mathbf{r}_i & \dots & \mathbf{R}_i \mathbf{p}_{k-1} + \mathbf{r}_i \end{pmatrix}, \tag{5.17}$$

or equivalently

$$\mathbf{Q}_i = \mathbf{R}_i \mathbf{P} + \mathbf{T}_i, \tag{5.18}$$

where $\mathbf{T}_i \in \mathbb{R}^{3\times k}$ has columns that are repeating representations of the airborne platform translation at t_i

$$\mathbf{T}_i = \begin{pmatrix} \mathbf{r}_i & \mathbf{r}_i & \dots & \mathbf{r}_i \end{pmatrix}. \tag{5.19}$$

Equation 5.18 shows that during t_{out} the observations $\mathbf{Q}_i$ are a rotated version of the point cloud $\mathbf{P}$ translated by the airborne platform. This also implies that $\mathbf{Q}_i$ is a rigid body transformed version of $\mathbf{P}$. We can solve for the rotation $\mathbf{R}_i$ and translation $\mathbf{T}_i$ in a least-squares sense using the strategy for finding rigid body transformations between point clouds developed by Arun et al. [98] (see Appendix A.1).

We utilize the platform rotations and translations found during t_{out} to infer those during t_{in} such that they adhere to our airborne sensor motion model (e.g. equation 5.1). More complicated motion models are also possible and do not reduce the generality of our method. For example, if the platform is not stabilized well and periodic sensor vibration is suspected, we may infer the dominant phase and frequency spectra of the platform motion using Fourier analysis. Non-linear non-periodic motion models may involve regressing the coefficients belonging to the first few polynomials that explain well the platforms motion during t_{out}. Linear platform translation would require us to infer translation during t_{in} by linear regression applied to all $(t_i, \mathbf{r}_i)$ for $t_i \in t_{out}$. If platform orientations are linearly varying, we could use spherical linear interpolation (SLERP) on rotation matrices found during t_{out} [99]. We stress that if the assumed motion model does not explain well the measurements during t_{out}, then the motion model must be modified (perhaps by adding higher order terms or periodic terms) until it explains well the measurements. For example, if a linear translation motion model is assumed, yet a clear quadratic residual remains after fitting a line to measurements during t_{out}, then a quadratic term must be added to the motion model. Perhaps, a motion model may even be learned using the measurements obtained during t_{out} via a machine learning technique. After all $\mathbf{T}_i$ and $\mathbf{R}_i$ are found, we infer the seismic signal $\mathbf{s}$ by undoing rotations and translations during t_{in}. During $t_i \in t_{in}$ the observations $\mathbf{Q}_i$ are rigid body transformations of the topography perturbed by $\mathbf{s}$. Specifically, during $t_i \in t_{in}$ each point in a point cloud observed by the moving platform is described by

$$\tilde{\mathbf{q}}_j = \mathbf{H}_i \left(\tilde{\mathbf{p}}_j + \tilde{\mathbf{s}}_i \right), \tag{5.20}$$

or

$$\mathbf{q}_j = \mathbf{R}_i \left(\mathbf{p}_j + \mathbf{s}_i \right) + \mathbf{r}_i. \tag{5.21}$$

Considering all $\mathbf{q}_j$ at a single time $t_i \in t_{in}$ we form a matrix of observations as

$$\mathbf{Q}_i = \mathbf{R}_i \left(\mathbf{P} + \mathbf{S}_i \right) + \mathbf{T}_i, \tag{5.22}$$

where $\mathbf{S}_i \in \mathbb{R}^{3\times k}$ has columns that are repeating representations of the seismic signal translation at t_i

$$\mathbf{S}_i = \begin{pmatrix} \mathbf{s}_i & \mathbf{s}_i & \dots & \mathbf{s}_i \end{pmatrix}. \tag{5.23}$$

The solution for the separated seismic signal at t_i is then

$$\mathbf{S}_i = \mathbf{R}_i^T \left(\mathbf{Q}_i - \mathbf{T}_i\right) - \mathbf{P}. \tag{5.24}$$

Here we use the transpose of the rotation matrix $\mathbf{R}_i^T$ as its inverse, since rotation matrices are orthogonal.

We can also obtain an estimate of uncertainty for the separated seismic signal by collectively considering the columns $\mathbf{S}_i$, noted as $\hat{\mathbf{S}}_i$, derived from noisy measurements at a particular time t_i. The columns of $\hat{\mathbf{Q}}_i$, and therefore $\hat{\mathbf{S}}_i$, correspond to points on the ground surface. Assuming that the noise in $\hat{\mathbf{Q}}_i$ is independent of the point being observed, and that all points undergo the same translation, we can collectively consider estimates of displacements for all points to obtain an estimate of uncertainty. Specifically, we can consider each column of $\mathbf{S}_i$ as an estimate of the seismic signal at t_i; the collection of all columns of $\hat{\mathbf{S}}_i$ can be considered as many noise observations of displacement. We take the estimate and uncertainty of the seismic signal at time t_i to be the mean and standard deviation, respectively, of the columns of $\hat{\mathbf{S}}_i$.

5.3 Results and Discussion

We divide our results into a series of experiments that illustrate the scenarios under which we can use our signal separation strategy to measure seismic signals from an airborne platform in practice. We identify parameters that exhibit successful seismic signal estimates by measuring the signal-to-noise ratio (SNR); we use the convention that $SNR > 0$ dB indicates success while a $SNR < 0$ dB indicates failure. We use the definition for SNR in dB that follows:

$$SNR = 10\log_{10}\left(\frac{\|s_i|^2}{\|s_i - \hat{s}_i\|^2}\right) \tag{5.25}$$

where s_i is one component of the true seismic signal and $\hat{s}_i$ is the corresponding estimate of s_i we estimate from our measurements (i.e. the mean of the ith row of the matrix $\hat{\mathbf{S}}$). In each experiment, we construct topography using a rugosity corresponding to $\sigma_t = 25$ cm, equal sample spacing $\Delta x = \Delta y = 1$ cm, and $N = 7$ wavelets. In all experiments, we simulate an airborne platform at a height of 2 m above the ground with linear platform rotation and translation equally applied about and along the $x-$, $y-$, and $z-$ axes. In each experiment, we recover a seismic signal that is one second long with compact support in $t \in [0.2, 0.8]$.

5.3.1 Seismic signal separation in noiseless observations

We first verify that our methodology recovers a seismic signal when no noise is present. In order to do so, we set the platform height at two meters above the ground, induce linear platform translation of 10 cm about all axes, induce linear platform rotation of 1° about all axes, and generate seismic signals with a maximum seismic signal peak of $s_{max} = 1$ mm to simulate observations $\mathbf{Q}_i$ for $i \in \{0, 1, ..., T-1\}$. The rotation we simulate is small, but a translation of 10 cm is a considerable distance for a stabilized sensor to move over the course of one second. We assume an airborne platform model that is linear in translation and rotation. The resulting observations are slightly curved due to the linear rotation over time and are orders of magnitude larger than the seismic signal (Figure 5.3a). The seismic signal recovered using our signal separation strategy shows excellent signal recovery for each of the three signal components and is nearly indistinguishable from the true signal (Figure 5.3b-c). This shows that our signal separation strategy works with zero observational noise for small s_{max}, small platform rotations of 1°, and modest platform translations of several centimeters. Next we explore the reality of recovering a seismic signal from noisy observations.

5.3.2 Seismic signal separation in noisy observations

We develop an understanding of how our methodology behaves as the observational noise (σ) increases by repeating the experiment described earlier with varying levels of noise and identifying when SNR drops less than 0. We consider noise between $\sigma = 0$ mm to

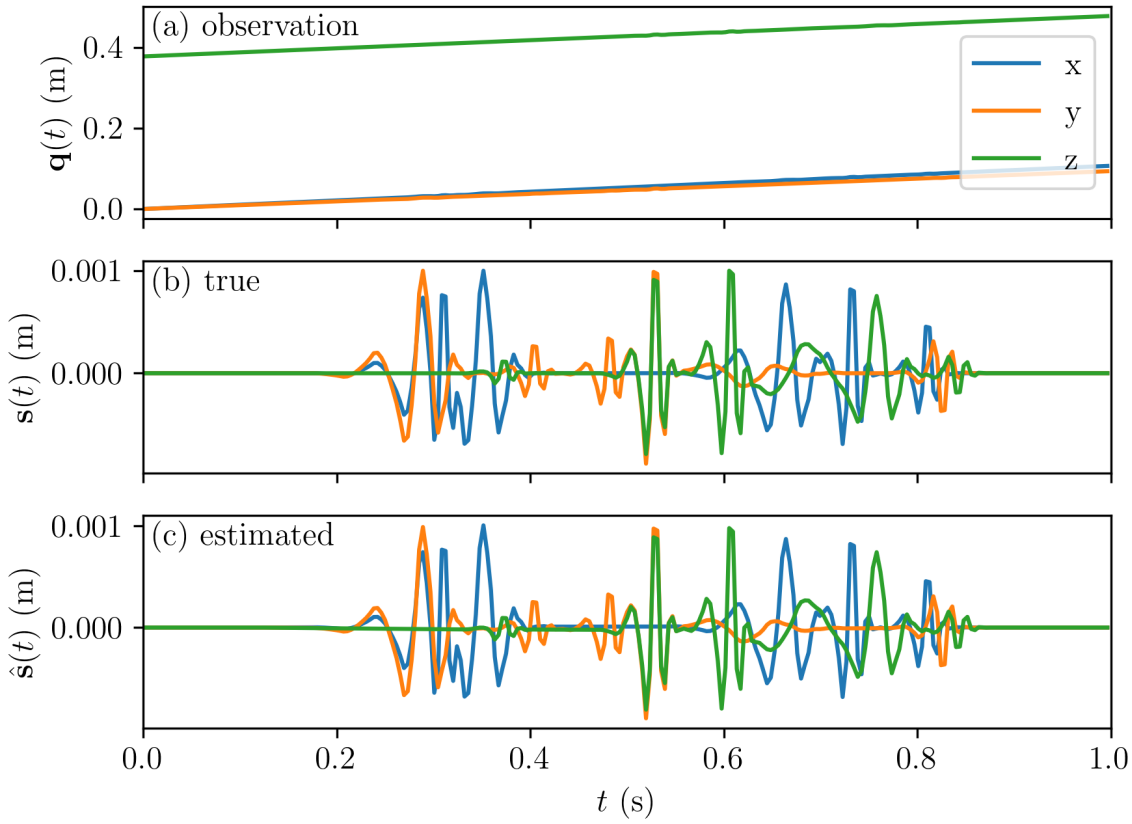

Figure 5.3: (a) Noiseless observation, (b) true seismic signal, and (c) estimated seismic signal.

$\sigma = 10$ cm; a generous range of noise values for modern laser- or camera-based sensors measuring distances roughly 2 meters away (the initial height of our platform above the ground). The recovered 3D seismic signal for two noise levels $\sigma = 0.5$ mm and $\sigma = 1.0$ mm shows that, unsurprisingly, our uncertainty increases as the noise in our measurements increase (Figure 5.4). We analyze how noise affects our separation more completely by conducting 31 simulations for each noise level between $\sigma = 1$ mm to $\sigma = 10$ cm and plotting the resulting SNR (Figure 5.5). As expected, for all components of $\mathbf{s}$, the SNR decreases as we add noise to our observations; SNR for the x-, y-, and z-component drops below 0 at $\sigma = 15$ mm (see Figure 5.5). However, the SNR for the z-component is consistently higher than x- or y-component SNR for lower noise levels ($\sigma < 1$ mm) (Figure 5.5). The lower SNR for the x- and y-component is expected since our topography is mostly planar (extending in the x- and y-directions); the x- and y- components of each point observed by the platform are the most affected by platform rotation, whereas the z-component is less affected. This encouraging result implies an airborne sensor can have a noise level that is roughly 15 times as high as the peak signal in $\mathbf{s}$ and still achieve an $SNR > 1$ from a platform height of 2 m.

5.3.3 Separation dependency on sensor rotation

We continue our analysis of how well signal separation performs by considering SNR as a function of sensor rotation angle. We repeat the noiseless experiment in Section 5.3.1 for a range of platform rotation angles between 0° and 10°, which is a reasonable range of angles relevant to stabilized sensors. Results show, again, that the $x-$ and $y-$ components have consistently lower SNR than the $z-$component (Figure 5.6). We observe that $SNR < 0$ below about $\theta = 2.75^\circ$ for the $x-$ and $y-$ components, but that $SNR > 0$ for angles up to, and beyond $\theta = 10.0^\circ$. The z-component SNR is greater than one for all angles below 10°. Thus, the recovery of the $z-$component is more robust to platform rotation angle changes than the $x-$ and $y-$ components.

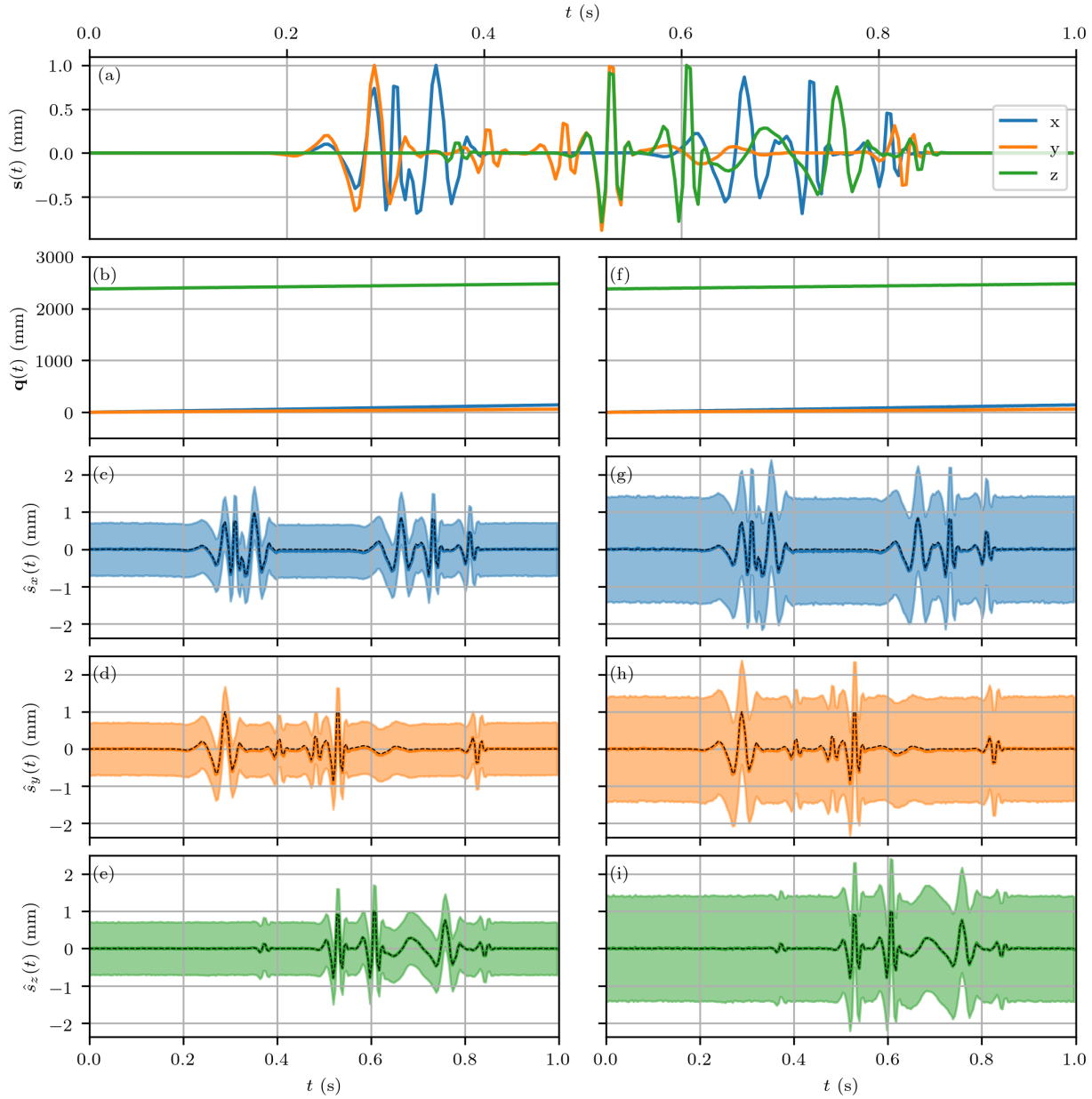

Figure 5.4: (a) True seismic signal and simulated noisy observations for (a) $\sigma = 0.5$ mm and (b) $\sigma = 1.0$ mm. Solid colors in (c-f) & (g-i) show each component of the mean recovered 3D seismic signal; shaded regions show the standard deviation of the estimated signal. (c-f) Recovery with a noise level $\sigma = 0.5$ mm shows lower uncertainty than that recovered using (g-i) a higher noise level $\sigma = 1.0$ mm.

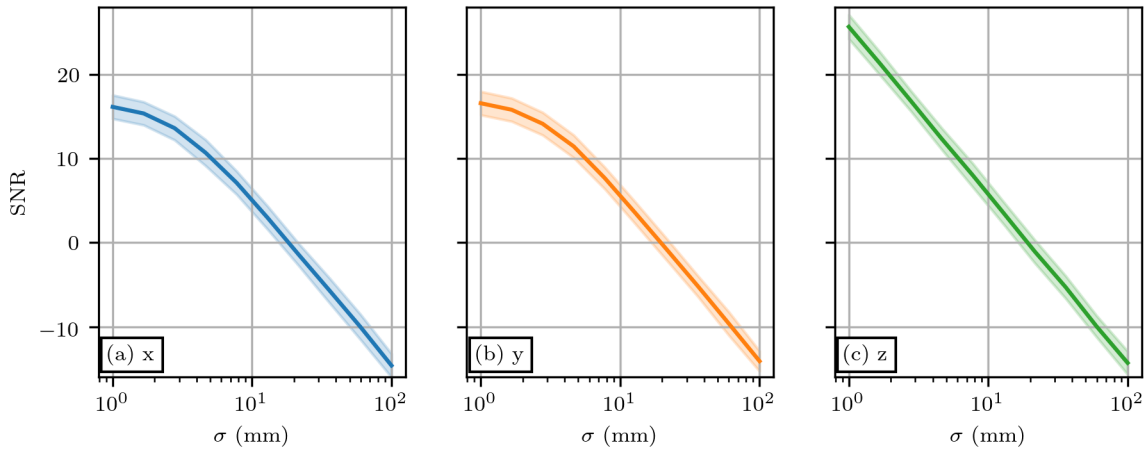

Figure 5.5: Derived SNR as a function of observational noise σ. We observe that SNR for $x-$ and $y-$ components are consistently lower than the $z-$ component SNR for noise levels below $\sigma = 1$ mm due to topography being mostly planar. We also observe that $SNR > 0$ for $\sigma < 15$ mm for all components.

5.3.4 Separation dependency on sensor noise level and max peak signal

Our signal separation strategy is affected by both the sensor noise level (σ) and maximum signal peak (s_{max}), thus, we jointly analyze how separation performs for many combinations of σ and s_{max}. We seek to identify a boundary in (σ, s_{max})-space that defines when our separation fails (i.e. when $SNR = 0$). We find this boundary by measuring SNR for recovered signals resulting from simulations with the platform height at 2 m, $\sigma \in [0.1 \text{ mm}, 1 \text{ cm}]$, and $s_{max} \in [0.1 \text{ mm}, 1 \text{ cm }]$. The resulting SNR maps for each component (Figure 5.7) show combinations of (σ, s_{max}) that result in $SNR > 0$. We define the $SNR = 0$ failure boundary (solid black line in Figure 5.7) in each SNR map to highlight combinations of (σ, s_{max}) that result in successfully separated seismic signals; areas in red in Figure 5.7 show viable (σ, θ) combinations, whereas blue areas highlight combinations that result in an unsuccessful signal separation.

In the $x-$ and $y-$component SNR maps (Figures 5.7a-b) we observe that SNR does not change as a function of σ when the s_{max} is below about 0.5 mm. We interpret this as a consequence of the sample spacing (in this particular case $\Delta x = \Delta y = 1$ cm) of our point

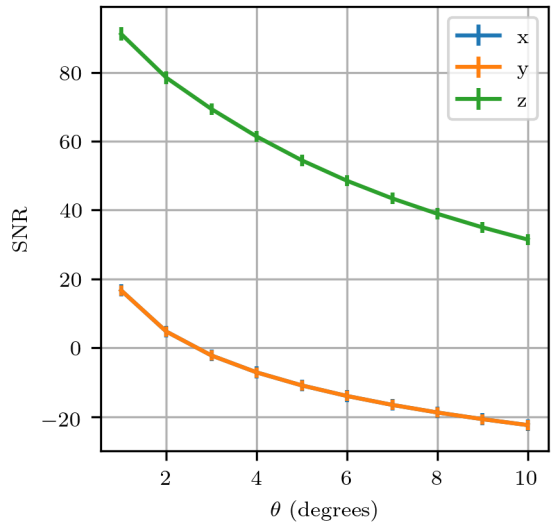

Figure 5.6: Derived SNR as a function of platform rotation θ. We observe smaller SNR for x- and $y-$ components compared to the z-component due to topography being mostly planar; rotation affects the x- and y- components of the points on the ground more than the z- components.

clouds being large compared to s_{max} and σ. We cannot recover the $x-$ and $y-$component of signals that are both far below the noise level and also far below our sampling in Δx and Δy. This feature is not observed in the $z-$component SNR map (Figure 5.7) since our topography is mostly planar; the $z-$coordinates are all very similar and represent a finer sample density along z compared to the sampling in x and y. Regardless, we find that that the failure boundary is approximately linear, and has a slope of approximately 20 for all components of displacement. Thus, from a 2 m platform height we can achieve $SNR > 0$ with an airborne sensor with σ 20$\times$ greater than s_{max} (provided σ is below the failure boundary in Figure 5.7). However, this conclusion relies on a sample spacing of $\Delta x = \Delta y = 1$ cm, which may vary based on the sensor of choice, thus we next explore variations in the failure boundary for various sample spacings.

5.3.5 Separation dependency on sample spacing

The SNR achieved using our signal separation method improves as the sample spacing (Δx and Δy) decreases. We reach this conclusion by repeating the experiment in Section

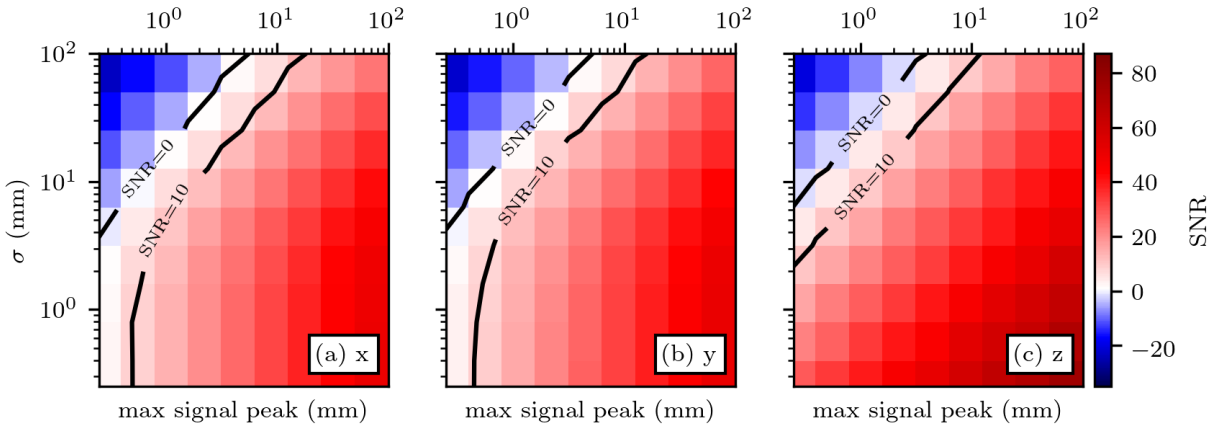

Figure 5.7: Signal-to-noise ratios for (a) x-, (b) y-, and (c) z-components of estimated seismic signal as a function of observation noise and peak signal amplitude. When the peak signal amplitude is close to the noise level we are able to recover the signal. Blue areas of each subplot denote $SNR < 0$ and indicate failure; red areas denote $SNR > 0$ and indicate success. We denote the failure boundary for each component using a solid black line in each subplot to indicate $SNR = 0$. Below the failure boundary our method succeeds to recover seismic signals.

5.3.4 where we measure SNR as a function of noise level (σ) and max peak signal (s_{max}) for various values of point sample spacings on the ground $\Delta x = \Delta y \in \{$20 cm, 10 cm, 5 cm, and 2.5 cm $\}$ within the same 1 m^2 area (see Figure 5.8). In each SNR map for the different values of $\Delta x = \Delta y$ (Figure 5.8) we find that the failure boundary, defined by $SNR = 0$, is approximately linear over most ranges of σ and θ for all options of $\Delta x = \Delta y$ (Figure 5.9). A steeper failure boundary slope implies that, for a given value of σ along the failure boundary, we can measure signals with smaller s_{max} if we increase the sample spacing of our measurements. We can more easily distinguish differences in the slope of each failure boundary by plotting them on a linear scale (Figure 5.9). The slopes for each failure boundary is summarized in Table 5.1, where we see that the slope roughly doubles as we halve the sample spacing. This behavior implies that measuring denser points on the ground from an airborne platform would substantially improve the SNR of recovered seismic signals.

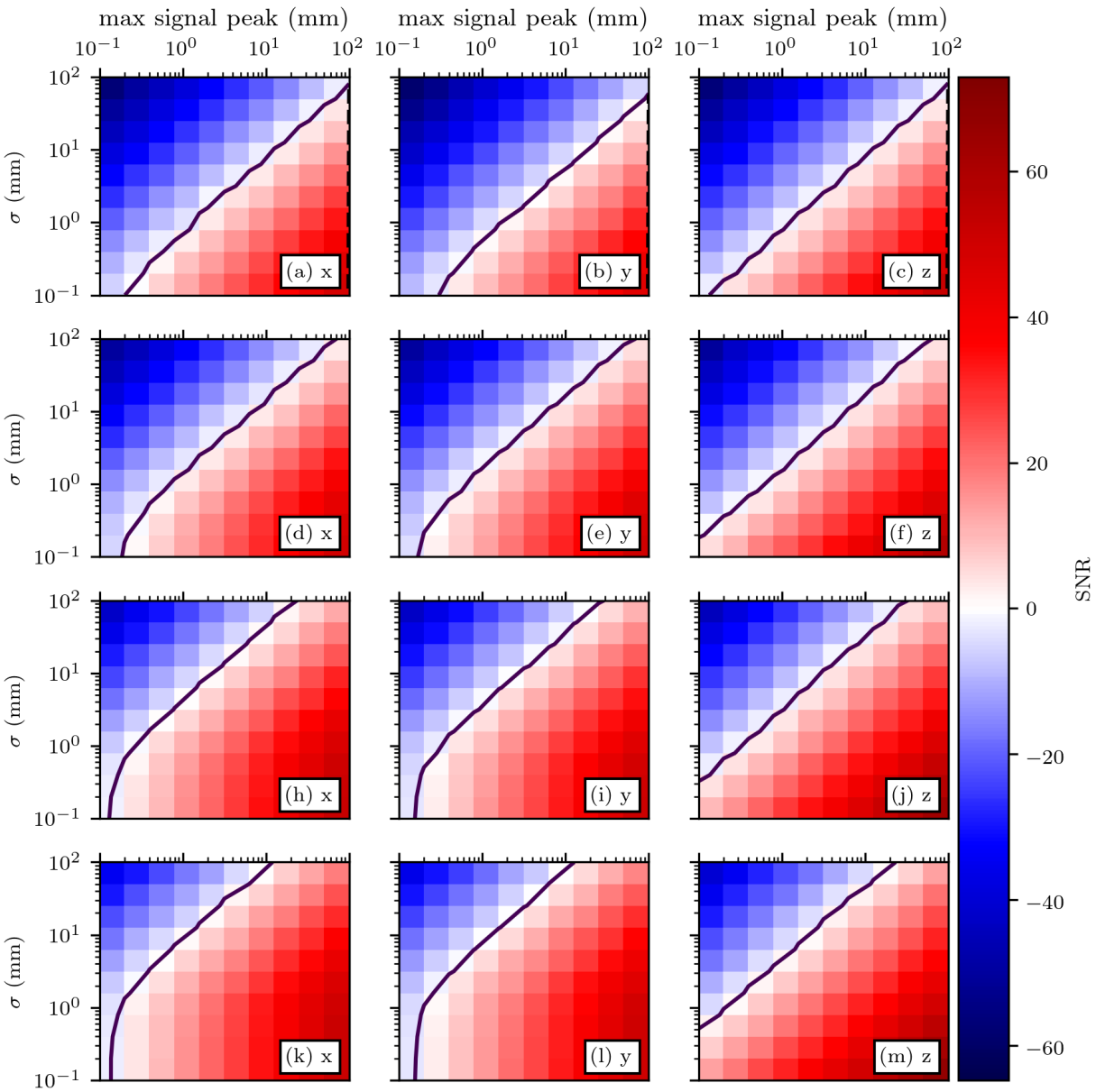

Figure 5.8: SNR maps for the x-, y-, and z- component of the estimated seismic signal as a function of σ and max signal peak for various $\Delta x = \Delta y =$ (a-c) 20 cm, (d-f) 10 cm, (h-j) 5 cm, and (k-m) 2.5 cm. We observe a general linear trend in the failure boundary at $SNR = 0$ marked as a black line on each subplot. These results imply that denser sample spacing results in higher SNR. We observe exception of for SNR values below $\sigma = 5.0$ cm where we see a nonlinear trend develop indicating no improvement in SNR with a decrease in σ.

Table 5.1: Failure boundary slope for each component of the estimated seismic signal for various sample spacings ($\Delta x = \Delta y$). The slope of the failure boundary quantifies the relationship between s_{max} and σ along the failure boundary. Higher slopes indicate that a higher sensor noise level σ can still achieve a given s_{max}.

	Slope of SNR failure boundary		
$\Delta x = \Delta y$	x	y	z
20 cm	0.808	0.594	0.823
10 cm	1.414	1.432	1.547
5 cm	4.225	3.436	3.033
2.5 cm	8.414	7.842	4.269

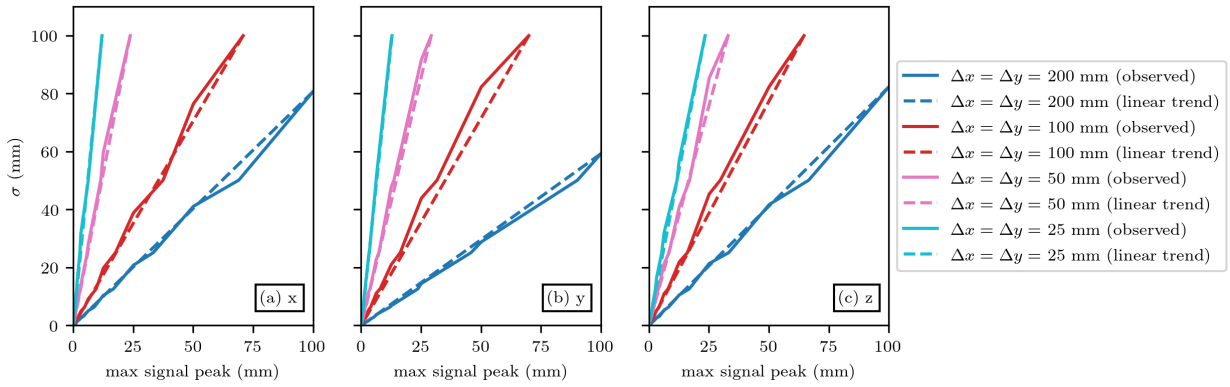

Figure 5.9: Failure boundaries defining $SNR = 0$ for (a) x-, (b) y-, and (c) z-components for varying sample spacings ($\Delta x = \Delta y$). Note that the failure boundaries here are plotted on a linear scale to highlight the differences in the slope of the failure boundary. The slope of each line is noted in Table 5.1. We find that smaller sample spacings give steeper failure boundaries. This indicates that for a given noise level on the failure boundary we can observe signals will smaller max signal peaks if we make measurements with denser sample spacings. The failure boundary slope roughly doubles if we half the sample spacing.

5.4 Conclusion

In response to advancements in drone and sensor technology, we develop a method for estimating and removing platform rotation and translation from consecutive measurements of point coordinates on the ground for measuring a 3D seismic signal. Our method assumes that the seismic signal has a finite duration and that a platform motion model is either known apriori or may be estimated from measurements made outside the support of the seismic signal. We achieve higher SNR when measurement noise level and platform rotation angles are small, when the seismic signal amplitude is large, and when the sampling point density of the sensor is high. We define a failure boundary that helps identify what combinations of noise level and max peak signal allow for seismic signal recovery. Using the boundary, we conclude that a sensor with $\sigma \approx 1$ mm mounted on a drone at 2 m height is capable of measuring seismic signals with max peak signals above $s_{max} \approx 0.1$ mm provided that ground sampling density is $\Delta x = \Delta y \leq 1$ cm, the sensor rotation $\theta \approx 1^{\circ}$, and sensor translation is less than 10 cm. We find that increasing sampling point density can make achieving $SNR < 0$ more feasible. Our method for defining the failure boundary can be used to explore other platform and sensor combinations, and facilitates exploring the effects of correlated observational noise as well as more complex platform motion models.

5.5 Acknowledgements

We thank the sponsor companies of the Center for Wave Phenomena, whose support made this research possible.

CHAPTER 6

CONCLUSION

This thesis develops key technology for acquiring remote measurements of ground displacement at spatial and temporal resolution necessary for novel geophysical and geomorphological applications. These advancements lead me to conclude the following: modern day camera technology is sufficient for measuring ground motion and its associated uncertainty due to a large earthquakes when the camera position is fixed or known (Chapter 2). Ground displacement and velocity during rapidly evolving landslide failure can be measured with two stationary video cameras; the accuracy of the video-based measurements is comparable to lidar-based measurements but are less expensive and far more broadly distributed (Chapter 3). In a controlled large-scale laboratory setting, the front position and velocity of a debris-flow is measurable via video with accuracy also comparable to lidar, with the added benefit of acquiring its surface velocity (Chapter 4). Using sensors mounted on an airborne platform, ground displacement can be measured provided a platform motion model is known or can be estimated, the ground translates as a rigid body, and the acquisition parameters are contained within the success-case areas (below the failure boundary) derived in Chapter 5. These conclusions rely on an array of assumptions which vary based on application and between each chapter of this thesis.

The results in this thesis are subject to a few caveats. (1) If the videos used to recover displacement are not taken from calibrated cameras, and if lens distortion is high, the techniques in Chapters 2-4 fail. (2) If the ground displacement signal of interest is below the diffraction limit, the appearance of the ground as measured by a camera does not change and the techniques in Chapters 2-4 fail. (3) If the debris-flow of interest traverses a surface with no markers and no known initial geometry, it is not possible to deduce debris-flow front position and velocity with one video camera. We emphasize that these caveats can be

addressed in practice (as they are in Chapters 2-5). In general, these caveats can be avoided by using multiple calibrated cameras to measure ground displacements above the diffraction limit within a scene of either (a) known initial geometry or (b) surveyed static markers.

Geophysical applications for measuring subtle, rapid, displacement signals extend beyond seismic data acquisition (Chapters 2 and 5) and landslide deformation studies (Chapters 3-4) presented here. Time-lapse variations in the bathymetry near critical subsea infrastructure could potentially be monitored using cameras. This would allow subsea risk assessment and the ability to avoid potentially dangerous subsea landslides. Drone-borne cameras could be used to measure time-varying sea surface topography, which can have dramatic negative effects on marine seismic data leading to inaccurate subsurface imaging [100]. Remote measurements of displacement could be made by satellite-borne instruments for applications in space exploration, similar to LDV-based measurements made from satellites but with wider spatial distribution [92].

Further advances in hardware and software technology increase the feasibility of airborne seismic in the future. It is safe to assume that the resolution and frame rate of cameras will continue to increase, leading to an increase in the spatial resolution of measurements advocated in this thesis; similarly an increase in frame rate would correspond to an increase in temporal resolution. This increase in spatial and temporal resolution would make geometric measurements from cameras increasingly more accurate and rapid. More subtle and rapidly varying physical phenomena could be routinely monitored using video cameras. Specifically, measurements that were only possible in controlled laboratory settings would become feasible in the field. This advancement would rely on sensor stabilization hardware becoming even more precise, rugged, and lighter weight. I envision a movement towards unique camera sensors paired with exotic fiducial markers placed on the ground for measuring seismic signals. Compressive sensing and sparse signal processing techniques would be necessary tools for realizing real-time ground displacement measurements. The future of airborne seismic relies on combining the expertise of engineers and geophysicists, yet the benefits of this

collaboration would allow us to more thoroughly explore the subsurface of the Earth in the years to come.

REFERENCES CITED

[1] Shimon Ullman. The interpretation of structure from motion. *Proceedings of the Royal Society of London. Series B. Biological Sciences*, 203(1153):405–426, 1979.

[2] R. Szeliski. *Computer vision: algorithms and applications*. Springer, 2011. tex.bibsource: http://www.visionbib.com/bibliography/book28.html#TT2007.

[3] Antoine Rabatel, Philip Deline, Stéphane Jaillet, and Ludovic Ravanel. Rock falls in high-alpine rock walls quantified by terrestrial lidar measurements: A case study in the Mont Blanc area. *Geophysical Research Letters*, 35(10), 2008.

[4] Michael A O'Neal and James E Pizzuto. The rates and spatial patterns of annual riverbank erosion revealed through terrestrial laser-scanner surveys of the South River, Virginia. *Earth Surface Processes and Landforms*, 36(5):695–701, 2011.

[5] Francis K Rengers and Greg E Tucker. The evolution of gully headcut morphology: a case study using terrestrial laser scanning and hydrological monitoring. *Earth Surface Processes and Landforms*, 40(10):1304–1317, 2015.

[6] Fabian Neugirg, Manuel Stark, Andreas Kaiser, Marketa Vlacilova, Marta Della Seta, Francesca Vergari, Jürgen Schmidt, Michael Becht, and Florian Haas. Erosion processes in Calanchi in the Upper Orcia Valley, Southern Tuscany, Italy based on multitemporal high-resolution terrestrial LiDAR and UAV surveys. *Geomorphology*, 269: 8–22, 2016.

[7] Jack G Williams, Nick J Rosser, Richard J Hardy, Matthew J Brain, and Ashraf A Afana. Optimising 4-D surface change detection: an approach for capturing rockfall magnitude–frequency. *Earth Surface Dynamics*, 6(1):101–119, 2018.

[8] Jack G Williams, Nick J Rosser, Richard J Hardy, and Matthew J Brain. The Importance of Monitoring Interval for Rockfall Magnitude-Frequency Estimation. *Journal of Geophysical Research: Earth Surface*, 2019.

[9] A Mazen Wahbeh, John P Caffrey, and Sami F Masri. A vision-based approach for the direct measurement of displacements in vibrating systems. *Smart Materials and Structures*, 12(5):785, 2003. tex.publisher: IOP Publishing.

[10] Michael Rubinstein and others. *Analysis and visualization of temporal variations in video*. PhD thesis, Massachusetts Institute of Technology, 2014.

[11] Neal Wadhwa, Michael Rubinstein, Frdo Durand, and William T. Freeman. Riesz pyramids for fast phase-based video magnification. 2014.

[12] Hao-Yu Wu, Michael Rubinstein, Eugene Inghaw Shih, John V Guttag, Frederic Durand, William T Freeman, and Neal Wadhwa. Linear-based eulerian motion modulation, February 26 2019. US Patent 10,217,218.

[13] Haider Ismael Shahadi, Hayder J Albattat, Zaid Jabbar Al-allaq, and Ahmed Toman Thahab. Eulerian video magnification: a review. *Indonesian Journal of Electrical Engineering and Computer Science*, 18(2):799–811, 2020.

[14] Daniele Faccio and Andreas Velten. A trillion frames per second: the techniques and applications of light-in-flight photography. *Reports on Progress in Physics*, 81(10): 105901, 2018. Whoa.

[15] David L. George and Richard M. Iverson. A depth-averaged debris-flow model that includes the effects of evolving dilatancy. II. Numerical predictions and experimental tests. *Proc. R. Soc. A*, 470(2170):20130820, 2014.

[16] Richard M. Iverson and David L. George. A depth-averaged debris-flow model that includes the effects of evolving dilatancy. I. Physical basis. *Proc. r. soc. a*, 470(2170): 20130819, 2014.

[17] FX Bostick III. Field experimental results of three-component fiber-optic seismic sensors. In *SEG technical program expanded abstracts 2000*, pages 21–24. Society of Exploration Geophysicists, 2000.

[18] J Mestayer, B Cox, P Wills, D Kiyashchenko, J Lopez, M Costello, S Bourne, G Ugueto, R Lupton, G Solano, and others. Field trials of distributed acoustic sensing for geophysical monitoring. In *SEG technical program expanded abstracts 2011*, pages 4253–4257. Society of Exploration Geophysicists, 2011.

[19] A Mateeva, J Mestayer, B Cox, D Kiyashchenko, P Wills, J Lopez, S Grandi, K Hornman, P Lumens, A Franzen, and others. Advances in distributed acoustic sensing (DAS) for VSP. In *SEG technical program expanded abstracts 2012*, pages 1–5. Society of Exploration Geophysicists, 2012.

[20] Thomas M Daley, Barry M Freifeld, Jonathan Ajo-Franklin, Shan Dou, Roman Pevzner, Valeriya Shulakova, Sudhendu Kashikar, Douglas E Miller, Julia Goetz, Jan Henninges, and others. Field testing of fiber-optic distributed acoustic sensing (DAS) for subsurface seismic monitoring. *The Leading Edge*, 32(6):699–706, 2013. Society of Exploration Geophysicists.

[21] Albena Mateeva, Jorge Lopez, Jeff Mestayer, Peter Wills, Barbara Cox, Denis Kiyashchenko, Zhaohui Yang, Wilfred Berlang, Rocky Detomo, and Samantha Grandi. Distributed acoustic sensing for reservoir monitoring with VSP. *The Leading Edge*, 32 (10):1278–1283, 2013. Society of Exploration Geophysicists.

[22] Albena Mateeva, Jorge Lopez, Hans Potters, Jeff Mestayer, Barbara Cox, Denis Kiyashchenko, Peter Wills, Samantha Grandi, Kees Hornman, Boris Kuvshinov, and others. Distributed acoustic sensing for reservoir monitoring with vertical seismic profiling. *Geophysical Prospecting*, 62(4):679–692, 2014. Wiley Online Library.

[23] Albert J Berni. Remote seismic sensing, December 1991. U.S. Patent No. 5,070,483.

[24] Albert J Berni. Remote sensing of seismic vibrations by laser Doppler interferometry. *Geophysics*, 59(12):1856–1867, 1994. Society of Exploration Geophysicists.

[25] AB Stanbridge, DJ Ewins, and AZ Khan. Modal testing using impact excitation and a scanning LDV. *Shock and Vibration*, 7(2):91–100, 2000. Hindawi Publishing Corporation.

[26] Lynn H Quam, Robert B Tucker, Sidney Liebes Jr, Marsha Jo Hannah, and Botond G Eross. Computer interactive picture processing. Technical Report 166, Stanford Artificial Intelligence Project Memo, 1972.

[27] Richard Szeliski. *Computer vision: Algorithms and applications*. Springer Science & Business Media, 2010.

[28] Daniel Scharstein and Richard Szeliski. A taxonomy and evaluation of dense two-frame stereo correspondence algorithms. *International journal of computer vision*, 47(1-3): 7–42, 2002. Springer.

[29] Elias Arias. Seismic slope estimation: analyses in 2d/3d. Master's thesis, Colorado School of Mines. Arthur Lakes Library, 2016.

[30] Dave Hale. Dynamic warping of seismic images. *Geophysics*, 78(2):S105–S115, 2013. Society of Exploration Geophysicists.

[31] Center for Engineering Strong Motion Data. USGS Station OK034. 2016. tex.howpublished: www.strongmotioncenter.org.

[32] Richard M. Iverson. Landslide triggering by rain infiltration. *Water resources research*, 36(7):1897–1910, 2000.

[33] Kritof Otir, Tatjana Veljanovski, Toma Podobnikar, and Zoran Stani. Application of satellite remote sensing in natural hazard management: the Mount Mangart landslide case study. *International Journal of Remote Sensing*, 24(20):3983–4002, 2003.

[34] Mario Parise. Observation of surface features on an active landslide, and implications for understanding its history of movement. *Natural Hazards and Earth System Science*, 3(6):569–580, 2003.

[35] Brent G. Delbridge, Roland Brgmann, Eric Fielding, Scott Hensley, and William H. Schulz. Three-dimensional surface deformation derived from airborne interferometric UAVSAR: Application to the Slumgullion Landslide. *Journal of Geophysical Research: Solid Earth*, 121(5):3951–3977, 2016.

[36] Dario Tarchi, Nicola Casagli, Riccardo Fanti, David D. Leva, Guido Luzi, Alessandro Pasuto, Massimiliano Pieraccini, and Sandro Silvano. Landslide monitoring by using ground-based SAR interferometry: An example of application to the Tessina landslide in Italy. *Engineering geology*, 68(1-2):15–30, 2003.

[37] Francesca Bozzano, Ivan Cipriani, Paolo Mazzanti, and Alberto Prestininzi. Displacement patterns of a landslide affected by human activities: Insights from ground-based InSAR monitoring. *Natural Hazards*, 59(3):1377–1396, 2011.

[38] W. H. Schulz, J. A. Coe, B. L. Shurtleff, J. Panosky, P. Farina, P. P. Ricci, and G. Barsacchi. Kinematics of the Slumgullion landslide revealed by ground-based InSAR surveys. In *Landslides and Engineered Slopes, Protecting Society through Improved Understanding*, volume 2, pages 1273–1279. Taylor & Francis, 2012.

[39] A Aryal, BA Brooks, JH Foster, and JM Becker. Velocity field estimation using terrestrial lidar 3D point cloud data. In *AGU Fall Meeting Abstracts*, 2008.

[40] Keith Williams, Michael Olsen, Gene Roe, and Craig Glennie. Synthesis of transportation applications of mobile LiDAR. *Remote Sensing*, 5(9):4652–4692, 2013.

[41] Francis Rengers, Thomas Rapstine, Kate Allstadt, Michael Olsen, Michael Bunn, Richard Iverson, Jason Kean, Ben Leshchinsky, Matthew Logan, Mahyar Sharifi-Mood, Maciej Obryk, and Joel Smith. Real-time monitoring of debris-flow velocity and mass deformation from field experiments with high sample rate lidar and video. 2019.

[42] Arko Lucieer, Steven M. de Jong, and Darren Turner. Mapping landslide displacements using Structure from Motion (SfM) and image correlation of multi-temporal UAV photography. *Progress in Physical Geography*, 38(1):97–116, 2014.

[43] L. L. C. AgiSoft. *Agisoft PhotoScan Professional Edition (version 1.4.4)*. 2018.

[44] Christian E. Willert and Morteza Gharib. Digital particle image velocimetry. *Experiments in fluids*, 10(4):181–193, 1991.

[45] Martin Detert and Volker Weitbrecht. A low-cost airborne velocimetry system: Proof of concept. *Journal of Hydraulic Research*, 53(4):532–539, 2015.

[46] Andr Stumpf, Emmanuel Augereau, Christophe Delacourt, and Julien Bonnier. Photogrammetric discharge monitoring of small tropical mountain rivers: A case study at Rivire des Pluies, Runion Island. *Water Resources Research*, 52(6):4550–4570, 2016.

[47] Catherine Berger, Brian W McArdell, Bruno Fritschi, and Fritz Schlunegger. A novel method for measuring the timing of bed erosion during debris flows and floods. *Water resources research*, 46(2), 2010. ISSN 0043-1397.

[48] C. Berger, B. W. McArdell, and Fritz Schlunegger. Direct measurement of channel erosion by debris flows, Illgraben, Switzerland. *Journal of Geophysical Research: Earth Surface*, 116(F1), 2011.

[49] G. Pulfer, M. Naaim, E. Thibert, and A. Soruco. Retrieving avalanche basal friction law from high rate positioning of avalanches. In *International Snow Science Workshop (ISSW)*, pages p. 1418–p. 1424. Irstea, ANENA, Meteo France, 2013.

[50] Qi-hua Ran, Wei Li, Qian Liao, Hong-lei Tang, and Meng-yao Wang. Application of an automated LSPIV system in a mountainous stream for continuous flood flow measurements. *Hydrological Processes*, 30(17):3014–3029, 2016.

[51] Guillaume Piton, Alain Recking, Jrme Le Coz, Herv Bellot, Alexandre Hauet, and Magali Jodeau. Reconstructing DepthAveraged OpenChannel Flows Using Image Velocimetry and Photogrammetry. *Water Resources Research*, 54(6):4164–4179, 2018.

[52] Richard M. Iverson, Mark E. Reid, and Richard G. LaHusen. Debris-flow mobilization from landslides. *Annual Review of Earth and Planetary Sciences*, 25(1):85–138, 1997.

[53] Richard M. Iverson, M. E. Reid, Neal R. Iverson, R. G. LaHusen, M. Logan, J. E. Mann, and D. L. Brien. Acute sensitivity of landslide rates to initial soil porosity. *science*, 290(5491):513–516, 2000.

[54] Richard M. Iverson, Matthew Logan, Richard G. LaHusen, and Matteo Berti. The perfect debris flow? Aggregated results from 28 largescale experiments. *Journal of Geophysical Research: Earth Surface*, 115(F3), 2010. doi: doi:10.1029/2009JF001514.

[55] Mark E. Reid, Richard G. LaHusen, and Richard M. Iverson. Debris-flow initiation experiments using diverse hydrologic triggers. *Debris-Flow Hazards Mitigation: Mechanics, Prediction and Assessment*, pages 1–11, 1997.

[56] Richard M. Iverson. Regulation of landslide motion by dilatancy and pore pressure feedback. *Journal of Geophysical Research: Earth Surface*, 110(F2), 2005.

[57] Matthew Logan, Richard M. Iverson, and Obryk, Maciej K. Video documentation of experiments at the USGS debris-flow flume 19922017 (ver 1.4, January 2018). Open-File Report, U.S. Geological Survey, 2018. URL `https://doi.org/10.3133/ofr20071315`.

[58] Robin Sibson. A vector identity for the Dirichlet tessellation. In *Mathematical Proceedings of the Cambridge Philosophical Society*, volume 87, pages 151–155. Cambridge University Press, 1980. ISBN 1469-8064.

[59] Abraham Savitzky and Marcel JE Golay. Smoothing and differentiation of data by simplified least squares procedures. *Analytical chemistry*, 36(8):1627–1639, 1964.

[60] Jean Steinier, Yves Termonia, and Jules Deltour. Smoothing and differentiation of data by simplified least square procedure. *Analytical chemistry*, 44(11):1906–1909, 1972.

[61] Gunnar Farnebck. Two-frame motion estimation based on polynomial expansion. In *Scandinavian conference on Image Analysis*, pages 363–370. Springer, 2003.

[62] Michael J. Olsen, Shawn Butcher, and Evon P. Silvia. Real-time change and damage detection of landslides and other earth movements threatening public infrastructure. Technical Report OTREC-RR-11-23, Transportation Research and Education Center (TREC), Portland, OR, 2012. URL `https://dx.doi.org/10.15760/trec.47`.

[63] Riegl Laser Measurement Systems. RiVLib, 2017. URL `http://www.riegl.com/index.php?id=224`.

[64] CG Johnson, BP Kokelaar, Richard M Iverson, M Logan, RG LaHusen, and JMNT Gray. Grain-size segregation and levee formation in geophysical mass flows. *Journal of Geophysical Research: Earth Surface*, 117(F1), 2012. doi: doi:10.1029/2011JF002185.

[65] Harry Nyquist. Certain topics in telegraph transmission theory. *Transactions of the American Institute of Electrical Engineers*, 47(2):617–644, 1928.

[66] Claude Elwood Shannon. A mathematical theory of communication. *Bell system technical journal*, 27(3):379–423, 1948.

[67] Claude Elwood Shannon. Communication in the presence of noise. *Proceedings of the IEEE*, 86(2):447–457, 1998.

[68] Henry Wilbraham. On a certain periodic function. *The Cambridge and Dublin Mathematical Journal*, 3:198–201, 1848.

[69] J. Willard Gibbs. Fourier's series. *Nature*, 59(1522):200, 1898.

[70] Thai Van Nguyen, Tuan Hong Do, and Dung Trung Vo. A novel joint blocking and ringing artifact reduction using advanced Beltrami based texture maps. *REV Journal on Electronics and Communications*, 7(1-2), 2017.

[71] Mike R. James and Stuart Robson. Mitigating systematic error in topographic models derived from UAV and groundbased image networks. *Earth Surface Processes and Landforms*, 39(10):1413–1420, 2014.

[72] D. Eckersley. Instrumented laboratory flowslides. *Geotechnique*, 40(3):489–502, 1990.

[73] G. Wang and K. Sassa. Factors affecting rainfall-induced flowslides in laboratory flume tests. *Geotechnique*, 51(7):587–599, 2001.

[74] Adam B Prochaska, Paul M Santi, and Jerry D Higgins. Debris basin and deflection berm design for fire-related debris-flow mitigation. *Environmental & Engineering Geoscience*, 14(4):297–313, 2008.

[75] Dieter Rickenmann. Empirical relationships for debris flows. *Natural hazards*, 19(1): 47–77, 1999.

[76] Laura Longoni, Monica Papini, Davide Brambilla, Luigi Barazzetti, Fabio Roncoroni, Marco Scaioni, and Vladislav Ivov Ivanov. Monitoring riverbank erosion in mountain catchments using terrestrial laser scanning. *Remote Sensing*, 8(3):241, 2016.

[77] Francis K Rengers, Thomas D Rapstine, Michael Olsen, Kate E Allstadt, Michael Bunn, Richard M Iverson, Jason W Kean, Ben Leshchinsky, Matthew Logan, Mahyar Sharifi-Mood, Maciej Obryk, and Joel B Smith. Using high sample rate lidar to capture debris-flow velocity and surface geometry. *in review*, 2020.

[78] Richard M. Iverson and David L. George. Basal Stress Equations for Granular Debris Masses on Smooth or Discretized Slopes. *Journal of Geophysical Research: Earth Surface*, 2019.

[79] Rengers, F. and Olsen, M. Lidar data for natural release experiment at the USGS Debris-Flow Flume. U.S. Geological Survey data release, 2020.

[80] Lucas J Van Vliet and Piet W Verbeek. Estimators for orientation and anisotropy in digitized images. In *ASCI Imaging Workshop, Venray, NL, October 25-27*. Citeseer, 1995.

[81] Gijs C Fehmers and Christian FW Höcker. Fast structural interpretation with structure-oriented filtering. *Geophysics*, 68(4):1286–1293, 2003.

[82] Dave Hale. Image-guided blended neighbor interpolation of scattered data. In *SEG Technical Program Expanded Abstracts 2009*, pages 1127–1131. Society of Exploration Geophysicists, 2009.

[83] I Sobel. An Isotropic 3×3 Gradient Operator, Machine Vision for Three-Dimensional Scenes. *Freeman, H., Academic Pres, NY*, page 376379, 1990.

[84] Bernd Jähne. *Spatio-temporal image processing: theory and scientific applications*, volume 751. Springer Science & Business Media, 1993.

[85] Obryk, Maciej K. and Iverson, Richard M. Sensor data from natural-release experiments conducted in May, 2017, at the USGS debris-flow flume, HJ Andrews Experimental Forest, Blue River, Oregon. U.S. Geological Survey data release, 2019.

[86] A Dräbenstedt, X Cao, U Polom, F Pätzold, T Zeller, P Hecker, V Seyfried, and C Rembe. Mobile seismic exploration. In *AIP Conference Proceedings*, volume 1740, page 030001. AIP Publishing LLC, 2016.

[87] Thomas Rapstine, Paul Sava, and Elias Arias. Airborne seismic data acquisition using stereo vision. *Journal of Unmanned Vehicle Systems*, 6(1):31–42, 2017.

[88] Thomas Rapstine and Paul Sava. Measuring seismic signals with airborne stereo cameras. In *SEG Technical Program Expanded Abstracts 2017*, pages 5943–5947. Society of Exploration Geophysicists, 2017. ISBN 1949-4645.

[89] Alexander Dräbenstedt. Diversity combining in laser Doppler vibrometry for improved signal reliability. In *AIP Conference Proceedings*, volume 1600, pages 263–273. American Institute of Physics, 2014.

[90] C Rembe and A Dräbenstedt. Speckle-insensitive laser-doppler vibrometry with adaptive optics and signal diversity. *Proceedings SENSOR 2015*, pages 505–510, 2015.

[91] Samuel Courville and Paul Sava. Speckle noise in orbital laser doppler vibrometry. In *Lunar and Planetary Science Conference*, volume 50, 2019.

[92] Samuel W. Courville. *Toward Orbital Seismology: Theory for Speckle Noise Reduction in Laser Doppler Vibrometer Measurements on Distant Rough Surfaces*. PhD thesis, Colorado School of Mines, 2019. URL `http://mines.idm.oclc.org/login?url=https://search.proquest.com/docview/2352101098?accountid=25386`.

[93] Justin G Chen, Neal Wadhwa, Young-Jin Cha, Frdo Durand, William T Freeman, and Oral Buyukozturk. Structural modal identification through high speed camera video: Motion magnification. In *Topics in modal analysis I*, volume 7, pages 191–197. Springer, 2014.

[94] Ali Shariati, Thomas Schumacher, and Nakul Ramanna. Eulerian-based virtual visual sensors to detect natural frequencies of structures. *Journal of Civil Structural Health Monitoring*, pages 1–12, 2015. tex.publisher: Springer.

[95] Hao-Yu Wu, Michael Rubinstein, Eugene Shih, John V Guttag, Frdo Durand, and William T Freeman. Eulerian video magnification for revealing subtle changes in the world. *ACM Trans. Graph.*, 31(4):65, 2012.

[96] Abe Davis, Michael Rubinstein, Neal Wadhwa, Gautham J. Mysore, Fredo Durand, and William T. Freeman. The visual microphone: passive recovery of sound from video. *ACM Transaction on Graphics*, 33 (4):79:1–79:10, 2014.

[97] Ingrid Daubechies. Orthonormal bases of compactly supported wavelets. *Communications on Pure and Applied Mathematics*, 41(7):909–996, 1988.

[98] K. Somani Arun, Thomas S. Huang, and Steven D. Blostein. Least-squares fitting of two 3-D point sets. *IEEE Transactions on pattern analysis and machine intelligence*, (5):698–700, 1987.

[99] Ken Shoemake. Animating rotation with quaternion curves. In *Proceedings of the 12th Annual Conference on Computer Graphics and Interactive Techniques*, pages 245–254, 1985.

[100] Tugrul Konuk and Jeffrey Shragge. Modeling full-wavefield time-varying sea-surface effects on seismic data: A mimetic finite-difference approach. *Geophysics*, 85(2):T45–T55, 2020.

APPENDIX

A.1 Estimating a rigid body transformation between point clouds

A least-squares solution to the rigid body transformation between two point clouds has previously been established by Arun et al. [98]. We briefly review this solution here. Consider matrices $\mathbf{A}, \mathbf{B} \in \mathbb{R}^{3\times k}$ whose corresponding columns represent k points in two point clouds. If $\mathbf{B}$ is $\mathbf{A}$ after rigid body transformation then we may express $\mathbf{B}$ as

$$\mathbf{B} = \mathbf{R}\mathbf{A} + \mathbf{T} \tag{A.1}$$

where $\mathbf{R} \in \mathbb{R}^{3\times 3}$ is a rotation matrix from $\mathbf{A}$ to $\mathbf{B}$, and $\mathbf{T} \in \mathbb{R}^{3\times k}$ contains the translation component of the rigid body transformation in matrix form

$$\mathbf{T} = \begin{pmatrix} \mathbf{t} & \dots & \mathbf{t} \end{pmatrix}, \tag{A.2}$$

where $\mathbf{t}$ is the translation from $\mathbf{A}$ to $\mathbf{B}$. Given observations of points in $\mathbf{A}$ and $\mathbf{B}$ we can find the least squares solution for $\mathbf{R}$ and $\mathbf{T}$ by minimizing

$$err = \sum_{i=0}^{k-1} ||\mathbf{R}\mathbf{a}_i + \mathbf{t} - \mathbf{b}_i||^2, \tag{A.3}$$

where $\mathbf{a}_i, \mathbf{b}_i \in \mathbb{R}^{3\times 1}$ denote corresponding points in each point set in corresponding columns of $\mathbf{A}$ and $\mathbf{B}$, respectively. The solution requires us to center each point cloud then deduce an optimal rotation between them by singular value decomposition. To center, we first compute the centroid of each x, y, and z component of both $\mathbf{A}$ and $\mathbf{B}$ by

$$\boldsymbol{\mu}_A = \frac{1}{k}\sum_{i}^{k} \mathbf{a}_i \tag{A.4}$$

and

$$\boldsymbol{\mu}_B = \frac{1}{k}\sum_{i}^{k} \mathbf{b}_i. \tag{A.5}$$

We then form the matrices for centering $\mathbf{A}$ and $\mathbf{B}$ as

$$\mathbf{M}_A = \begin{pmatrix} \boldsymbol{\mu}_A & \boldsymbol{\mu}_A & \dots & \boldsymbol{\mu}_A \end{pmatrix}, \tag{A.6}$$

and

$$\mathbf{M}_B = \begin{pmatrix} \boldsymbol{\mu}_B & \boldsymbol{\mu}_B & \dots & \boldsymbol{\mu}_B \end{pmatrix}. \tag{A.7}$$

Then, we compute the singular value decomposition

$$\mathbf{UEV}^T = (\mathbf{A} - \mathbf{M}_A)(\mathbf{B} - \mathbf{M}_B)^T. \tag{A.8}$$

The least-squares solution for the rotation matrix $\mathbf{R}$ is given by

$$\widehat{\mathbf{R}} = \mathbf{VU}^T. \tag{A.9}$$

Once we compute the least squares solution for $\mathbf{R}$ we can estimate the translation component of the rigid body transformation by inserting $\mathbf{M}_A$ and $\mathbf{M}_B$ into equation A.1 and solving for $\mathbf{T}$

$$\widehat{\mathbf{T}} = \mathbf{M}_B - \widehat{\mathbf{R}}\mathbf{M}_A. \tag{A.10}$$

A.2 Permissions from journal

Permission to include work from the Journal of Unmanned Aerial Vehicles and from the Journal of Geophysical Research - Earth Surfaces are shown in Figure A.1 and Figure A.2, respectively. The URL for permissions in the Journal of Unmanned Aerial Vehicles is `https://www.nrcresearchpress.com/page/authors/information/rights`. The URL for permissions in the Journal of Geophysical Research - Earth Surfaces is `https://agupubs.onlinelibrary.wiley.com/hub/journal/21699011/permissions`.

A.3 Permissions from coauthors

The permissions from each coauthor are shown by the email screenshots in Figure A.3, A.4, A.5, A.6, A.7, A.8, A.9, A.10, and A.11,

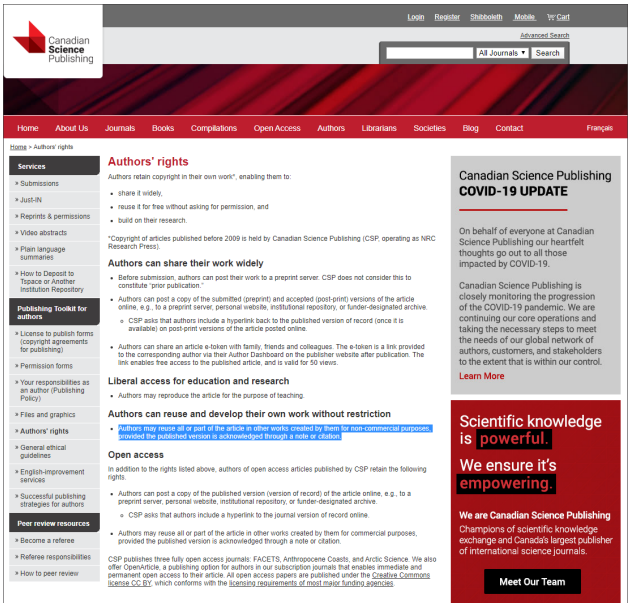

Figure A.1: Permission statement for the Journal of Unmanned Aerial Vehicles paper published under Canadian Science Publishing hightlighted in blue.

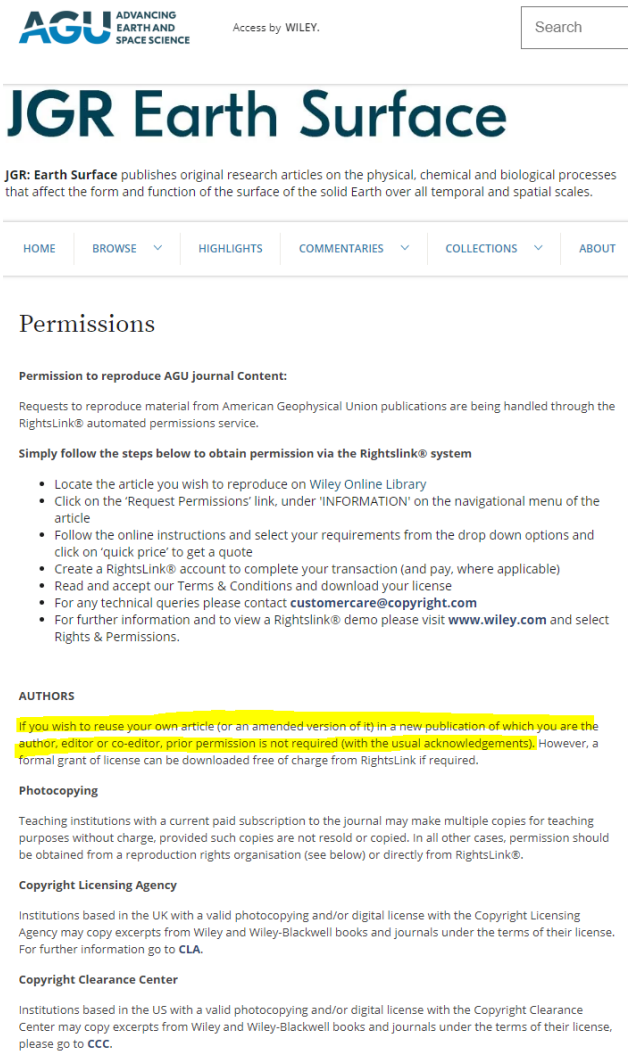

AGU ADVANCING EARTH AND SPACE SCIENCE

Access by WILEY.

Search

JGR Earth Surface

JGR: Earth Surface publishes original research articles on the physical, chemical and biological processes that affect the form and function of the surface of the solid Earth over all temporal and spatial scales.

HOME | BROWSE | HIGHLIGHTS | COMMENTARIES | COLLECTIONS | ABOUT

Permissions

Permission to reproduce AGU journal Content:

Requests to reproduce material from American Geophysical Union publications are being handled through the RightsLink® automated permissions service.

Simply follow the steps below to obtain permission via the Rightslink® system

- Locate the article you wish to reproduce on Wiley Online Library
- Click on the 'Request Permissions' link, under 'INFORMATION' on the navigational menu of the article
- Follow the online instructions and select your requirements from the drop down options and click on 'quick price' to get a quote
- Create a RightsLink® account to complete your transaction (and pay, where applicable)
- Read and accept our Terms & Conditions and download your license
- For any technical queries please contact **customercare@copyright.com**
- For further information and to view a Rightslink® demo please visit **www.wiley.com** and select Rights & Permissions.

AUTHORS

If you wish to reuse your own article (or an amended version of it) in a new publication of which you are the author, editor or co-editor, prior permission is not required (with the usual acknowledgements). However, a formal grant of license can be downloaded free of charge from RightsLink if required.

Photocopying

Teaching institutions with a current paid subscription to the journal may make multiple copies for teaching purposes without charge, provided such copies are not resold or copied. In all other cases, permission should be obtained from a reproduction rights organisation (see below) or directly from RightsLink®.

Copyright Licensing Agency

Institutions based in the UK with a valid photocopying and/or digital license with the Copyright Licensing Agency may copy excerpts from Wiley and Wiley-Blackwell books and journals under the terms of their license. For further information go to **CLA**.

Copyright Clearance Center

Institutions based in the US with a valid photocopying and/or digital license with the Copyright Clearance Center may copy excerpts from Wiley and Wiley-Blackwell books and journals under the terms of their license, please go to **CCC**.

Figure A.2: Permission statement for Journal of Geophysical Research - Earth Surfaces hightlighted in yellow.

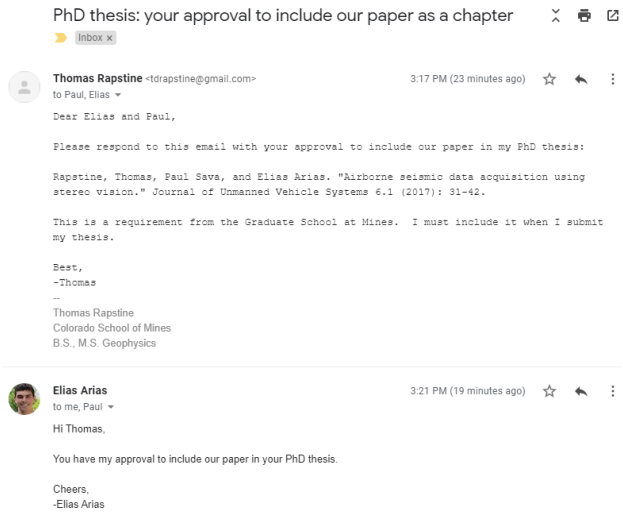

Figure A.3: Permission statement from coauthor Elias Arias.

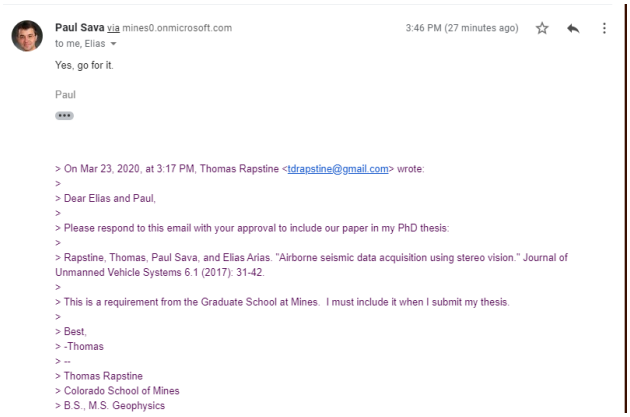

Figure A.4: Permission statement from coauthor Dr. Paul Sava.

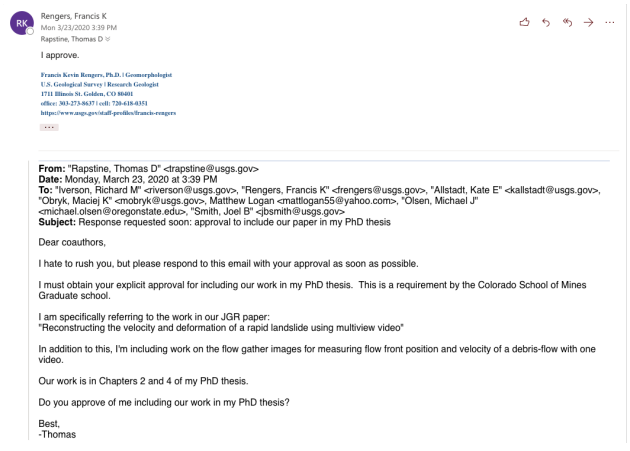

Figure A.5: Permission statement from coauthor Dr. Francis Rengers.

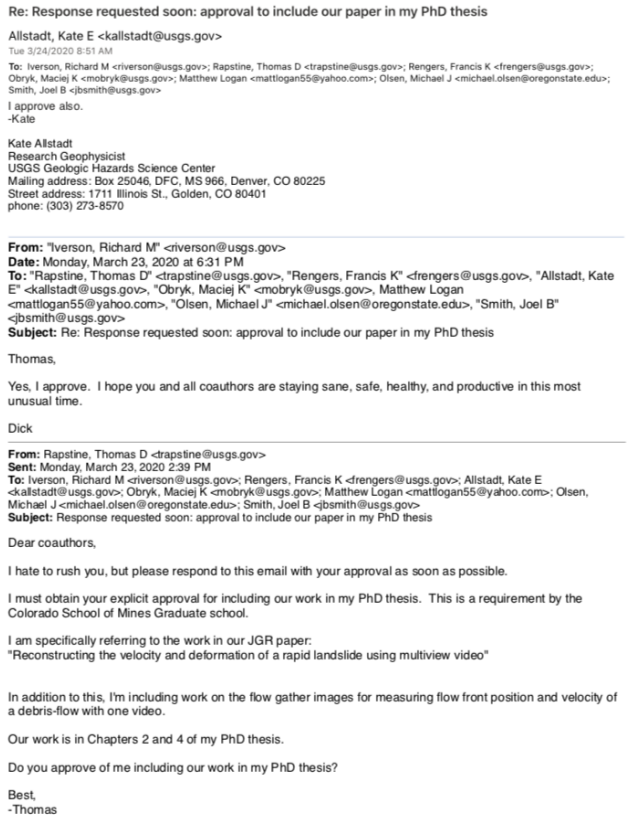

Re: Response requested soon: approval to include our paper in my PhD thesis

Allstadt, Kate E <kallstadt@usgs.gov>
Tue 3/24/2020 8:51 AM

To: Iverson, Richard M <riverson@usgs.gov>; Rapstine, Thomas D <trapstine@usgs.gov>; Rengers, Francis K <frengers@usgs.gov>; Obryk, Maciej K <mobryk@usgs.gov>; Matthew Logan <mattlogan55@yahoo.com>; Olsen, Michael J <michael.olsen@oregonstate.edu>; Smith, Joel B <jbsmith@usgs.gov>

I approve also.
-Kate

Kate Allstadt
Research Geophysicist
USGS Geologic Hazards Science Center
Mailing address: Box 25046, DFC, MS 966, Denver, CO 80225
Street address: 1711 Illinois St., Golden, CO 80401
phone: (303) 273-8570

From: "Iverson, Richard M" <riverson@usgs.gov>
Date: Monday, March 23, 2020 at 6:31 PM
To: "Rapstine, Thomas D" <trapstine@usgs.gov>, "Rengers, Francis K" <frengers@usgs.gov>, "Allstadt, Kate E" <kallstadt@usgs.gov>, "Obryk, Maciej K" <mobryk@usgs.gov>, Matthew Logan <mattlogan55@yahoo.com>, "Olsen, Michael J" <michael.olsen@oregonstate.edu>, "Smith, Joel B" <jbsmith@usgs.gov>
Subject: Re: Response requested soon: approval to include our paper in my PhD thesis

Thomas,

Yes, I approve. I hope you and all coauthors are staying sane, safe, healthy, and productive in this most unusual time.

Dick

From: Rapstine, Thomas D <trapstine@usgs.gov>
Sent: Monday, March 23, 2020 2:39 PM
To: Iverson, Richard M <riverson@usgs.gov>; Rengers, Francis K <frengers@usgs.gov>; Allstadt, Kate E <kallstadt@usgs.gov>; Obryk, Maciej K <mobryk@usgs.gov>; Matthew Logan <mattlogan55@yahoo.com>; Olsen, Michael J <michael.olsen@oregonstate.edu>; Smith, Joel B <jbsmith@usgs.gov>
Subject: Response requested soon: approval to include our paper in my PhD thesis

Dear coauthors,

I hate to rush you, but please respond to this email with your approval as soon as possible.

I must obtain your explicit approval for including our work in my PhD thesis. This is a requirement by the Colorado School of Mines Graduate school.

I am specifically referring to the work in our JGR paper:
"Reconstructing the velocity and deformation of a rapid landslide using multiview video"

In addition to this, I'm including work on the flow gather images for measuring flow front position and velocity of a debris-flow with one video.

Our work is in Chapters 2 and 4 of my PhD thesis.

Do you approve of me including our work in my PhD thesis?

Best,
-Thomas

Figure A.6: Permission statement from coauthor Dr. Kate Allstadt.

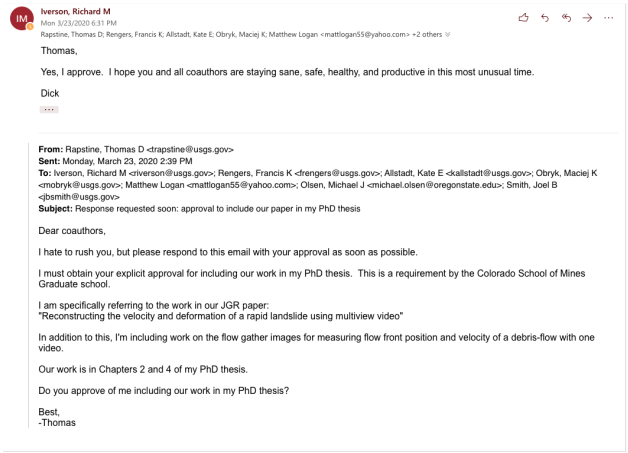

Iverson, Richard M
Mon 3/23/2020 6:31 PM
Rapstine, Thomas D; Rengers, Francis K; Allstadt, Kate E; Obryk, Maciej K; Matthew Logan <mattlogan55@yahoo.com> +2 others

Thomas,

Yes, I approve. I hope you and all coauthors are staying sane, safe, healthy, and productive in this most unusual time.

Dick

From: Rapstine, Thomas D <trapstine@usgs.gov>
Sent: Monday, March 23, 2020 2:39 PM
To: Iverson, Richard M <riverson@usgs.gov>; Rengers, Francis K <frengers@usgs.gov>; Allstadt, Kate E <kallstadt@usgs.gov>; Obryk, Maciej K <mobryk@usgs.gov>; Matthew Logan <mattlogan55@yahoo.com>; Olsen, Michael J <michael.olsen@oregonstate.edu>; Smith, Joel B <jbsmith@usgs.gov>
Subject: Response requested soon: approval to include our paper in my PhD thesis

Dear coauthors,

I hate to rush you, but please respond to this email with your approval as soon as possible.

I must obtain your explicit approval for including our work in my PhD thesis. This is a requirement by the Colorado School of Mines Graduate school.

I am specifically referring to the work in our JGR paper:
"Reconstructing the velocity and deformation of a rapid landslide using multiview video"

In addition to this, I'm including work on the flow gather images for measuring flow front position and velocity of a debris-flow with one video.

Our work is in Chapters 2 and 4 of my PhD thesis.

Do you approve of me including our work in my PhD thesis?

Best,
-Thomas

Figure A.7: Permission statement from coauthor Dr. Richard Iverson.

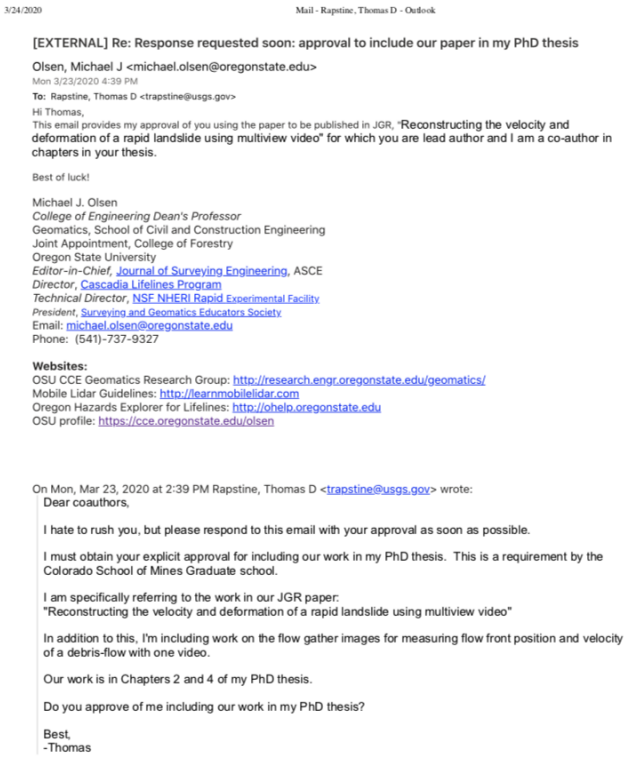

3/24/2020 Mail - Rapstine, Thomas D - Outlook

[EXTERNAL] Re: Response requested soon: approval to include our paper in my PhD thesis

Olsen, Michael J <michael.olsen@oregonstate.edu>
Mon 3/23/2020 4:39 PM
To: Rapstine, Thomas D <trapstine@usgs.gov>

Hi Thomas,
This email provides my approval of you using the paper to be published in JGR, "Reconstructing the velocity and deformation of a rapid landslide using multiview video" for which you are lead author and I am a co-author in chapters in your thesis.

Best of luck!

Michael J. Olsen
College of Engineering Dean's Professor
Geomatics, School of Civil and Construction Engineering
Joint Appointment, College of Forestry
Oregon State University
Editor-in-Chief, Journal of Surveying Engineering, ASCE
Director, Cascadia Lifelines Program
Technical Director, NSF NHERI Rapid Experimental Facility
President, Surveying and Geomatics Educators Society
Email: michael.olsen@oregonstate.edu
Phone: (541)-737-9327

Websites:
OSU CCE Geomatics Research Group: http://research.engr.oregonstate.edu/geomatics/
Mobile Lidar Guidelines: http://learnmobilelidar.com
Oregon Hazards Explorer for Lifelines: http://ohelp.oregonstate.edu
OSU profile: https://cce.oregonstate.edu/olsen

On Mon, Mar 23, 2020 at 2:39 PM Rapstine, Thomas D <trapstine@usgs.gov> wrote:

Dear coauthors,

I hate to rush you, but please respond to this email with your approval as soon as possible.

I must obtain your explicit approval for including our work in my PhD thesis. This is a requirement by the Colorado School of Mines Graduate school.

I am specifically referring to the work in our JGR paper:
"Reconstructing the velocity and deformation of a rapid landslide using multiview video"

In addition to this, I'm including work on the flow gather images for measuring flow front position and velocity of a debris-flow with one video.

Our work is in Chapters 2 and 4 of my PhD thesis.

Do you approve of me including our work in my PhD thesis?

Best,
-Thomas

Figure A.8: Permission statement from coauthor Dr. Michael Olsen.

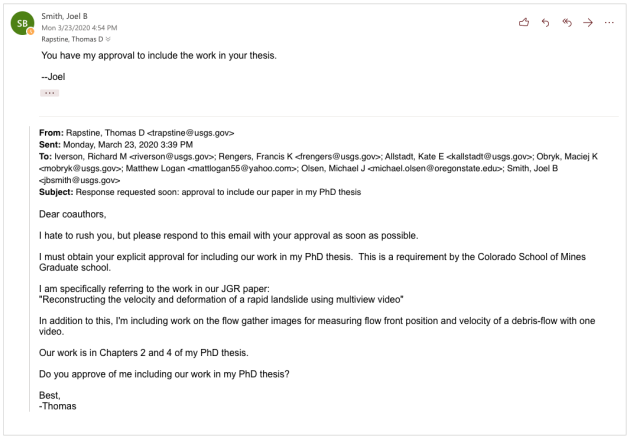

Smith, Joel B
Mon 3/23/2020 4:54 PM
Rapstine, Thomas D

You have my approval to include the work in your thesis.

--Joel

From: Rapstine, Thomas D <trapstine@usgs.gov>
Sent: Monday, March 23, 2020 3:39 PM
To: Iverson, Richard M <riverson@usgs.gov>; Rengers, Francis K <frengers@usgs.gov>; Allstadt, Kate E <kallstadt@usgs.gov>; Obryk, Maciej K <mobryk@usgs.gov>; Matthew Logan <mattlogan55@yahoo.com>; Olsen, Michael J <michael.olsen@oregonstate.edu>; Smith, Joel B <jbsmith@usgs.gov>
Subject: Response requested soon: approval to include our paper in my PhD thesis

Dear coauthors,

I hate to rush you, but please respond to this email with your approval as soon as possible.

I must obtain your explicit approval for including our work in my PhD thesis. This is a requirement by the Colorado School of Mines Graduate school.

I am specifically referring to the work in our JGR paper:
"Reconstructing the velocity and deformation of a rapid landslide using multiview video"

In addition to this, I'm including work on the flow gather images for measuring flow front position and velocity of a debris-flow with one video.

Our work is in Chapters 2 and 4 of my PhD thesis.

Do you approve of me including our work in my PhD thesis?

Best,
-Thomas

Figure A.9: Permission statement from coauthor Joel Smith.

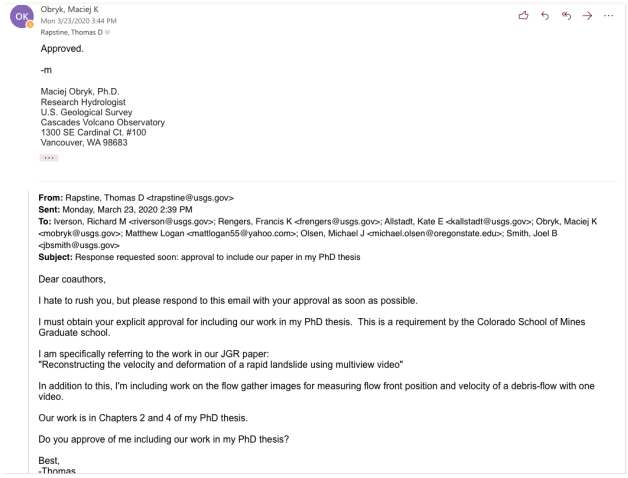

Obryk, Maciej K
Mon 3/23/2020 3:44 PM
Rapstine, Thomas D

Approved.

-m

Maciej Obryk, Ph.D.
Research Hydrologist
U.S. Geological Survey
Cascades Volcano Observatory
1300 SE Cardinal Ct. #100
Vancouver, WA 98683

From: Rapstine, Thomas D <trapstine@usgs.gov>
Sent: Monday, March 23, 2020 2:39 PM
To: Iverson, Richard M <riverson@usgs.gov>; Rengers, Francis K <frengers@usgs.gov>; Allstadt, Kate E <kallstadt@usgs.gov>; Obryk, Maciej K <mobryk@usgs.gov>; Matthew Logan <mattlogan55@yahoo.com>; Olsen, Michael J <michael.olsen@oregonstate.edu>; Smith, Joel B <jbsmith@usgs.gov>
Subject: Response requested soon: approval to include our paper in my PhD thesis

Dear coauthors,

I hate to rush you, but please respond to this email with your approval as soon as possible.

I must obtain your explicit approval for including our work in my PhD thesis. This is a requirement by the Colorado School of Mines Graduate school.

I am specifically referring to the work in our JGR paper:
"Reconstructing the velocity and deformation of a rapid landslide using multiview video"

In addition to this, I'm including work on the flow gather images for measuring flow front position and velocity of a debris-flow with one video.

Our work is in Chapters 2 and 4 of my PhD thesis.

Do you approve of me including our work in my PhD thesis?

Best,
-Thomas

Figure A.10: Permission statement from coauthor Maciej Obryk.

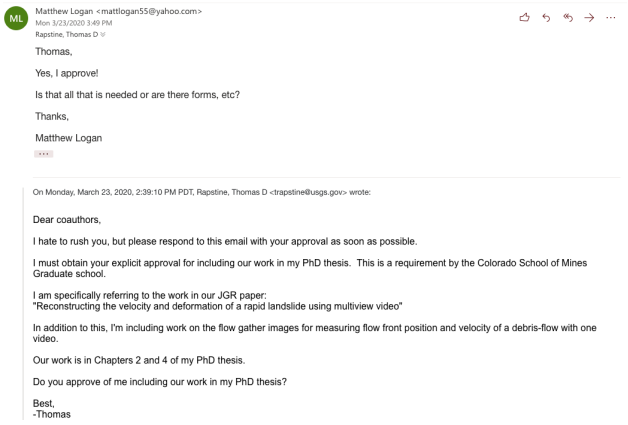

Matthew Logan <mattlogan55@yahoo.com>
Mon 3/23/2020 3:49 PM
Rapstine, Thomas D

Thomas,

Yes, I approve!

Is that all that is needed or are there forms, etc?

Thanks,

Matthew Logan

On Monday, March 23, 2020, 2:39:10 PM PDT, Rapstine, Thomas D <trapstine@usgs.gov> wrote:

Dear coauthors,

I hate to rush you, but please respond to this email with your approval as soon as possible.

I must obtain your explicit approval for including our work in my PhD thesis. This is a requirement by the Colorado School of Mines Graduate school.

I am specifically referring to the work in our JGR paper:
"Reconstructing the velocity and deformation of a rapid landslide using multiview video"

In addition to this, I'm including work on the flow gather images for measuring flow front position and velocity of a debris-flow with one video.

Our work is in Chapters 2 and 4 of my PhD thesis.

Do you approve of me including our work in my PhD thesis?

Best,
-Thomas

Figure A.11: Permission statement from coauthor Dr. Matthew Logan.